

Ultrafast dynamics driven by attosecond and structured photons

Dissertation

zur Erlangung des Doktorgrades der Naturwissenschaften
(Dr. rer. nat.)

der

Naturwissenschaftlichen Fakultät II
Chemie, Physik und Mathematik

der Martin-Luther-Universität
Halle-Wittenberg

vorgelegt von

Herrn Wätzel, Jonas
geb. am 27.09.1988 in Halle (Saale)

Betreuer:

1. Dr. Yaroslav Pavlyukh, Martin-Luther-Universität Halle-Wittenberg
2. Prof. Dr. Jamal Berakdar, Martin-Luther-Universität Halle-Wittenberg

Gutachter:

1. Prof. Dr. Jamal Berakdar, Martin-Luther-Universität Halle-Wittenberg
2. Prof. Dr. Jörg Schilling, Martin-Luther-Universität Halle-Wittenberg
3. Prof. Dr. Dieter Bauer, Universität Rostock

Datum der Abgabe: 8. August 2016

Datum der öffentlichen Verteidigung: 19. Dezember 2016

Vorsitzender der Promotionskommission: Prof. Dr. Thurn-Albrecht

Table of contents

Overview	1
1 Angular resolved time delay in photoionization	3
1.1 Introduction	3
1.2 The time delay for Coulomb potentials	7
1.3 Calculation of the atomic time delay	11
1.4 Numerical extraction of the time delay	15
1.5 Influence of multielectron effects on the time delay	16
1.6 Angular dependence of the atomic time delay	21
1.6.1 Neon	21
1.6.2 Argon	25
1.7 Conclusion	29
2 Ultrafast processes with light carrying orbital angular momentum	31
2.1 Introduction	31
2.2 Mathematical description of OAM beams	34
2.3 Time delay in atomic photoionization with optical vortex beams	36
2.3.1 Photoionization amplitude	36
2.3.2 Evaluation of the time delay	40
2.3.3 Dependence on the distance to the optical axis	44
2.3.4 Conclusion	45
2.4 Driving current loops in C ₆₀ by optical vortex beams	45
2.4.1 Theoretical model	45
2.4.2 Photo-induced magnetic moment	49
2.4.3 Magnetic field	53
2.4.4 Conclusion	55
2.5 Centrifugal photovoltaic effect induced by optical vortex beams	56
2.5.1 Details of the investigation	56
2.5.2 Photo-induced charge drift	59
2.5.3 Photovoltaic current generation	62

2.5.4 Conclusion	65
Summary	67
References	69
List of figures	80
List of Publications	84
Acknowledgements	85

Overview

The present thesis deals with the investigation of ultrafast quantum mechanical processes accessed by structured optical probes with a focus on two main aspects:

At first, we will study the *time delay in photoionization* which describes the delayed photoemission following the absorption of an exciting photon. It was predicted theoretically more than half a century ago [1, 2] and confirmed thanks to recent experimental advances in measurements of the electron dynamics on the attosecond time scale [3]. The reported existence of the time delay in photoionization triggered large activities in the field of attosecond physics. In addition to measurements in atoms [3–5] as well as in condensed matter [6], several theoretical results and interpretations within the frameworks of both the time-dependent [7–11] and time-independent [12–17] picture complemented the experiments. However, the theoretical attempts to reproduce the experimental results with a broad range of models and techniques have not yet converged to the experimental findings. A more detailed introduction of the time delay will be presented in the first chapter of this thesis. Here, we will discuss the dependence of the time delay on the emission angle for different atomic systems. Most of the theoretical results deliver the time delay in the forward direction, i.e. the photoelectron is detected along the laser polarization axis. Therefore, we will address the question to which extent the angular dependence influences the measured time delay with reference to its value in the forward direction and demonstrate that the angular characteristics are strongly influenced by the choice of the theoretical model and the accurate description of the electronic structure.

A second big topic is dedicated to the inspection of the possibility of structuring the light beam. In particular, we will employ *light carrying orbital angular momentum*, also called an optical vortex. This class of light waves was predicted in the 1990s [18–23] and revealed interesting applications [24–36]. For our purpose, the outstanding feature is the capability of transferring orbital angular momentum to charge carriers allowing for a new class of photo-induced non-dipolar transitions. This opens the door to interesting effects and a vast number of possible utilizations in different fields of physics.

We will discuss how an optical vortex pulse interplays with the time delay. Therefore, we will demonstrate that applying such a light beam allows discerning the atomic time delay from magnetic sub-levels even for completely spherically symmetric targets.

Another investigation is focused on the generation of a magnetic pulse inside a C_{60} molecule by irradiating it with an optical vortex pulse. The subsequent interaction initiates non-dipolar transitions from the occupied radial bands to virtual bound states. As a consequence, a current loop on the sphere of the molecule will be generated which produces a measurable magnetic field in the regime of mT.

An impressive application of the optical vortex light is the possibility to generate a directed photo-current by irradiating a semiconductor-based quantum ring which is attached to a straight conducting channel. The light-matter interaction leads to an effective enhancement of the repulsive centrifugal potential which causes a charge imbalance between the ring boundaries. We will demonstrate that the accompanied photocurrent can be tuned effectively by the parameters of the optical vortex laser pulse.

A summary and outlook conclude this thesis.

Chapter 1

Angular resolved time delay in photoionization

1.1 Introduction

The development of attosecond light sources [37–39] opened the door to exciting new opportunities for studying ultrafast phenomena and proving well-established theoretical models developed 30 - 40 years ago [40]. A broad class of different atomic, molecular and condensed matter systems can be explored with these techniques, and the theoretical results are confirmed by experiments on the electron dynamics [6, 14, 41–46].

For instance, a generated photoelectron can be deflected by an intense laser pulse which can be recorded by the attosecond streaking technique. A typical streaking metrology for measurements to trace photoelectron dynamics is in principle a pump-probe setup consisting of an extreme ultraviolet (XUV) pulse of a few hundred attoseconds serving as the pump, while a phase-coherent few-cycle infrared (IR) pulse plays the role of the probe pulse. The physics behind this streaking setup is the following: photoelectrons, which are liberated from the atomic core while interacting with the pump XUV pulse, are (de-)accelerated in the presence of the probe IR field to different final momenta. The corresponding kinetic energy depends on the value of the vector potential at the moment of the release. Classically the final momenta can be described by

$$p_f = p_0 - A_{\text{IR}}(t_0), \quad (1.1)$$

where t_0 is the moment of ionization and $p_0(t_0) = \sqrt{2(\omega_{\text{XUV}} - \varepsilon_i)}$ is the free-field asymptotic momentum of the photoelectron originating from a valence shell i with the energy level ε_i while interacting with an XUV-pulse with the photon energy $\hbar\omega_{\text{XUV}}$. The temporal characteristic of the vector potential of the probing field is given by $A_{\text{IR}}(t)$. Thus, varying the delay time between the maximum of the XUV pulse and IR pulse leads to different final

momenta and the time information of the electron dynamics can be accessed by momentum measurements [3, 6]. First applications and proofs were the measurement of the Kr($3d^{-1}$) hole lifetime due to the Auger decay [47] and the detecting of the time-dependent electric field of an IR light wave [48].

The XUV field in the streaking setup is generally in the weak-field high-frequency regime, which allows us to treat the photoionization process with the perturbation theory. Thus, the ratio between the intensity and the frequency $I_{\text{XUV}}/\omega_{\text{XUV}} \ll 1$. As a consequence, for photon energies in the XUV regime, an intensity $I_{\text{XUV}} \leq 10^{14}$ W/cm² is sufficiently weak. In contrast, the typical intensity of the IR-field is high enough ($I_{\text{IR}} \approx 10^{10} - 10^{12}$ W/cm², $\omega_{\text{IR}} = 0.057$ a.u.) that the continuum state of the liberated photoelectron is heavily perturbed with the consequence that a perturbative description is not possible. Nevertheless, the field strength is not in the regime that tunnel ionization processes are dominant. A well-established method is the so-called "soft photon approximation" for the ionization of atoms with the help of a weak XUV pulse in the presence of an IR laser field [49–52]. The condition of this approximation is that the frequency of the IR-photon is small in comparison to the energy of the photoelectron.

However, this method implies that the interaction between the liberated photoelectron and the residual ion is neglected. Consequently, the influence of the Coulomb potential and correlation effects have no impact on the calculation. In the literature, the motion of the photoelectron in the combined Coulomb and IR laser field is often called Coulomb-laser coupling and can be studied analytically within the Coulomb-Volkov approximation (CVA) [53, 54], which can be applied to the soft photon approximation [52].

Usually, it is assumed that emission of a photoelectron from an atom which absorbs an energetic photon leads to a wave packet which follows the temporal variation of the incident laser field instantly. In the 1950s it was suggested that the response of the wave packet to the light field is delayed [1, 55]. The temporal shift between the arrival of the XUV laser field and the departure of the wave packet is called the *time delay* in photoionization τ .

The time delay was measured and therefore confirmed 2010 by the pioneer experiment of Schultze *et al.* [3] who found a relative time delay in photoemission τ^{2p-2s} between photoelectrons originating from $2s$ and $2p$ valence shells in neon. The experimentally obtained time delay with the help of the attosecond streaking metrology is 21 ± 5 as. We call this experimentally obtained time delay in the following the *streaking delay* τ_S because the IR field has a substantial influence on the time delay. The experimental result triggered a tremendous interest of the scientific community in this topic and was the beginning of a series of theoretical and experimental works and publications. Schultze *et al.* tried to reproduce the time delay theoretically with various models. A multi-configurational Hartree-Fock (MCHF) calculation neglecting the influence of the IR field resulted in a relative time delay of 4.0 as. Correlation effects like interchannel coupling were included with the help of the state-specific expansion approach (SSEA), leading to a delay of 6.4 as. The influence of

the IR field was modeled with the aid of the CVA whereas correlation effects were neglected. An analysis of the photoelectron wave packets yielded a time delay of 4.5 as. Consequently, the computed time delay is around 15 as smaller than the measured value [3].

Other theoretical groups tried to resolve this controversy between experimental and theoretical results. Time-independent and time-dependent approaches were utilized to calculate the time delay. The time-independent one concentrates on the accurate calculation of the dipole matrix element of the photoionization process, which is directly connected with the time delay as the group delay of the photoelectron wave packet. In this direction Kheifets and Ivanov calculated a relative time of 8.4 as by using the Hartree-Fock (HF) and random phase approximation (RPAE) method for the absorption of a single XUV photon [12, 16]. The two-color case, i.e. the combined XUV and IR field, was discussed by Dahlström *et al.* within a diagrammatic approach [17, 56], while another method uses an MCHF close-coupling ansatz [57]. Time-dependent approaches aimed at the accurate simulation of the streaking spectra, i.e. by incorporating the IR field. The disadvantage is the incomplete description of electron-electron correlation effects within the photoionization process. The group of Nagele *et al.* calculated the time delay including the effect of the IR-field in simulations for one or two active electrons in model systems [7, 8]. Moore *et al.* used the time-dependent R-Matrix method for neon with a limited basis size and obtained a relative time delay of 10.3 ± 1.5 as [13]. Generally, all theoretical efforts led to computed delays more than a factor of 2 shorter than the experimentally obtained value. The up to date most complete quantum mechanical simulation of the streaking setup by Feist *et al.* [11] using a B-Spline R-Matrix method led to a relative time delay of 10.0 as. Furthermore, the calculation reveals the trend that the time delay decreases with increasing photon energies of the corresponding XUV-field, which is not precisely reproducible in the experiment. In general, the dividing of the streaking time delay τ_S into a sum of two terms is accepted:

$$\tau_S = \tau_{\text{at}} + \tau_{\text{CLC}}. \quad (1.2)$$

The first contribution is the *atomic time delay* τ_{at} originating from the pure photoionization process initiated by the XUV pulse. The second term τ_{CLC} arises from the interaction between the IR field and the photoelectron which moves in the Coulomb field of the residual ion. The combination of both is called Coulomb-laser coupling (CLC) [4, 7, 8, 15, 56].

For all Coulombic systems, we will show that the atomic time delay as a system-dependent quantity can be identified with the Eisenbud-Wigner-Smith time delay τ_W [1, 58], i.e. $\tau_{\text{at}} \equiv \tau_W$, whose characteristics play an integral role in this thesis. The validity of the Eq. (1.2) is proofed for photoelectrons in the continuum originating from noble gas atoms [56]. However, it is expected that Eq. (1.2) is not correct in the case of autoionizing resonances that lead to slow delay structures in the Coulomb field of the residing ion [57]. The τ_{CLC} shows some remarkable characteristics as the phase corresponding to the

delay is universal, i.e. it depends only on the final momentum of the photoelectron, the probe frequency ω_{IR} of the dressing IR-field and the charge of the residual ionic core. Consequently, it is independent of the considered atomic system. Some compact equations in various approximation for calculating the CLC delay are available [9, 10, 15]. In contrast, the atomic time delay contribution τ_{W} is not universal and reflects the scattering properties of the atomic system directly .

Lately, the studies of the time delay moved to another noble gas system. Argon was predestined because interesting phenomena occur at energies around the Cooper minimum [4, 5]. The Cooper minimum characterizes a minimum of the ionization rate for different photon energies when at least two final ionization channels exist, and the interference between those channels induces a change of the sign of the phase of the excited state wave function. In this case, the ionization probability can be zero or reach a minimum at a certain energy [59]. Klünder *et al.* [4] measured a relative time delay between photoemissions from the $3p$ and $3s$ valence shells in argon for photon energies of the XUV pulse in the range of 34-40 eV. Guénot *et al.* [5] revisited this experiment, and their results confirmed the earlier measurements, except for the highest photon energy at 40 eV, where a significant discrepancy occurs. The time delay was computed theoretically with the help of the RPAE model and diagrammatic approaches [4, 5, 16, 17, 57]. Recently, it was recalculated with the time-dependent density functional (TDDFT) theory as a conceptionally different approach to the many-body problem [60, 61].

Rarely discussed is the angular dependence of the time delay in photoionization, especially for the both experimental target systems neon and argon. In the case of hydrogen, a strong variation of the atomic time delay was calculated for angles around $\pm 90^\circ$ relative to the laser polarization axis [62]. The angular properties of the time delay corresponding to the photoionization of the H_2 molecule were also discussed theoretically [63, 64] and measured in a two-color experiment [65]. Very recently, the angular dependence of the time delay of a photoelectron liberated from the $3p$ subshell in argon was confirmed indirectly due to angle-integrated measurements [66].

In the experimental setup, the time-of-flight (TOF) detector collects all contributions from photoelectrons within a certain solid angle Ω_{max} . Here we introduce the angle $\vartheta_{\mathbf{k}}$ between the asymptotic direction of the momentum of the photoelectron and the laser polarization axis, which is parallel to the z -axis. We will discuss to which extent the resulting time delay is influenced by the effect of the angular dependence since most available calculations only concentrated on the computation in the forward direction, i.e. $\vartheta_{\mathbf{k}} = 0^\circ$. To address this point we consider all possible propagation directions of the photoelectrons.

Unless otherwise stated, atomic units (a.u.) will be used throughout this chapter.

1.2 The time delay for Coulomb potentials

In the following section the equivalence between the atomic time delay τ_{at} and the Wigner time delay τ_{W} will be derivated. Therefore, to depict the individual scattering properties of the considered atomic system only the calculation of the Wigner time delay is needed. This statement is correct for short-range potentials as well as for the long-range Coulomb potential. Further, this emphasizes the validity Eq. 1.2 in the case of the attosecond streaking of an atomic target. An analytic result for the universal and system-independent CLC contribution to the streaking time delay is derived.

Following Ref. [9] let us introduce formally the differential operator (which we will refer to as the time operator)

$$\hat{t} = -i \frac{\partial}{\partial t}. \quad (1.3)$$

Conceptually we are facing some problems with this definition, since the spectrum of the Hamilton operator, \hat{H} , is bounded [67]. By restricting the domain to the continuum, i.e. to scattering states, an expectation value of the time operator can be found [1, 2, 58]:

$$\langle t \rangle = -i S^\dagger(\epsilon_k) \frac{\partial}{\partial \epsilon_k} S(\epsilon_k), \quad (1.4)$$

where $S(\epsilon_k)$ is the well-known scattering matrix which depends on the kinetic energy $\epsilon_k = k^2/2$ of the particle. Consequently, we can identify the expectation value $\langle t \rangle$ as the time delay of the particle due to the scattering process. The quantity describes the delayed departure of the outgoing wave packet relative to the incoming particle after passing the scattering region. For a short-range potential and in case of spherical symmetry the S-Matrix is diagonal in the angular momentum representation and we find a simple expression [68]:

$$S_\ell = e^{i2\delta_\ell(\epsilon_k)}. \quad (1.5)$$

Here $\delta_\ell(\epsilon_k)$ describes the energy dependent scattering phase shift of the scattering potential. Now we can introduce the formal expression of the expectation value

$$\langle t \rangle = 2 \frac{\partial}{\partial \epsilon_k} \delta_\ell(\epsilon_k), \quad (1.6)$$

which is simply the energy-derivative of the scattering phase shift depending on the angular momentum characterized by ℓ .

In the case of photoionization we consider a half-scattering process, because the incident channel is a bound state and only the outgoing final channel resides in the continuum.

Consequently, we introduce the Wigner time delay τ_W in such a scenario [1, 9]:

$$\tau_W = \frac{\partial}{\partial \epsilon_k} \delta_\ell(\epsilon_k). \quad (1.7)$$

In general, the final state f is a superposition of several exit channels with different final angular momenta ℓ . In such a case the atomic time delay is defined with the help of the dipole matrix element $D_i(\mathbf{k})$ which characterizes the transition from the initial state $|\Psi_i\rangle$ to the final state $|\Psi_f\rangle$:

$$\tau_W(\epsilon_k, \theta_k) = \frac{\partial}{\partial \epsilon_k} \arg [D_i(\mathbf{k})] = \frac{\partial}{\partial \epsilon_k} \arg [\langle \Psi_f | \hat{z} | \Psi_i \rangle], \quad (1.8)$$

where \hat{z} is the dipole operator. In principle, this formal introduction of the Wigner time delay represents only the one-color photoionization process, i.e. only the XUV pulse is considered, in a short range potential. In this case, we can immediately state that $\tau_{\text{at}} \equiv \tau_W$ is valid [9, 10].

We consider now a photoelectron in a Coulomb field and the presence of the IR field. Revisiting the streaking metrology and keeping in mind the nature within the streaking time delay τ_S , which characterizes the delayed (positive value) or advanced (negative value) emission relative to the center of the XUV pulse, the final momentum distribution of the streaked photoelectron is given by

$$p_f(\Delta t_{\text{XUV-IR}}) = p_0 - \alpha A_{\text{IR}}(\Delta t_{\text{XUV-IR}} + \tau_S). \quad (1.9)$$

Here, $\Delta t_{\text{XUV-IR}}$ is the delay time between the XUV and IR pulses. The α is a correction factor for the amplitude, which is shifted due to the action of the IR streaking field $A_{\text{IR}}(t)$. In the case, the transition from the bound state to the asymptotic continuum state happens instantaneously, the streaking delay $\tau_S = 0$ and Eq. 1.9 reduces to the standard equation Eq. (1.1).

In the case of a long-range potential, we are facing significant problems in finding a good definition of a finite atomic time delay τ_{at} . The reason is that for the spherically symmetric Coulomb potential $V(r) = -Z/r$ the scattering matrix $S(\epsilon_k)$ can be introduced as a sum of two terms [69]:

$$S(\epsilon_k) = S^C(\epsilon_k) + S^{\text{cor}}(\epsilon_k). \quad (1.10)$$

The first contribution is the pure Coulomb scattering operator $S^C(\epsilon_k) = e^{i2\sigma_\ell(\epsilon_k)}$ (in angular momentum representation) where $\sigma_\ell(\epsilon_k)$ represent the scattering phases of the Coulomb potential. The second term is the remaining part $S^{\text{cor}}(\epsilon_k)$ due to the long-range characteristics. The resulting atomic time delay in the case of our photoionization process by following the

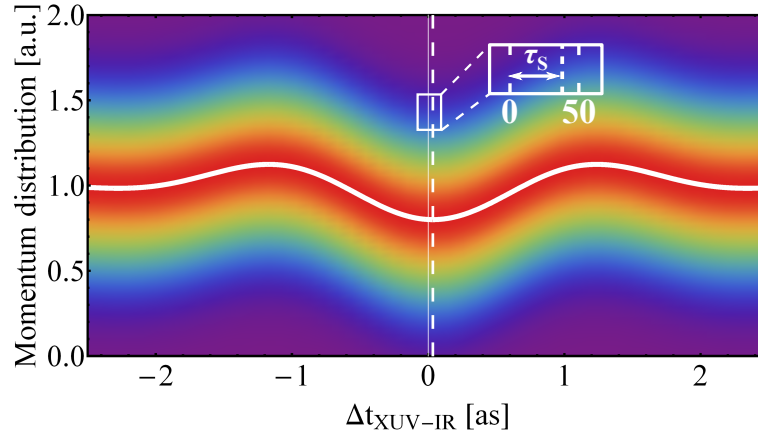


Fig. 1.1 Streaking spectrogram corresponding to the photoionization of the hydrogen $1s$ ground state by an XUV pulse with a photon energy $\hbar\omega_{\text{XUV}} = 27.211$ eV. The photoelectron is probed by an 800 nm IR laser field with a duration of 6 fs and an intensity of 10^{12} W/cm 2 . The red color means here the largest ionization probability while violet corresponds to no photoionization. The electron momentum distribution is depicted for various values of the delay time $\Delta t_{\text{XUV-IR}}$ between the maxima of the XUV and IR field. The solid white line shows the center of energy (COE) and therefore the peak position of the final electron momentum distribution. The small inset reveals the streaking delay τ_S .

Eq. (1.4) would then be given by [69, 70]:

$$\tau_{\text{at}}(\epsilon_k) = -iS^{C^\dagger}(\epsilon_k) \frac{\partial}{\partial \epsilon_k} S^C(\epsilon_k) + \frac{Z}{(2\epsilon_k)^{3/2}} \left[1 - \ln(2\sqrt{2\epsilon_k r}) \right], \quad (1.11)$$

where we can identify the first term as the conventional Wigner time delay of the Coulomb phase shift, i.e. $\tau_{\text{W}}^{\text{Coul}}(\epsilon_k) = \frac{\partial}{\partial \epsilon_k} \sigma_\ell(k)$ (cf. Eq. (1.7)). The second term in Eq. (1.11) incorporates the logarithmic distortion of the wavefront and is characteristic for all Coulomb type potentials. Interesting is the aspect that the time delay as a form of a time expectation in the asymptotic limit value depends on the propagation time t_{prop} ($r \approx kt_{\text{prop}}$):

$$t_{\text{cor}}^{\text{Coul}}(\epsilon_k, r) = \frac{Z}{(2\epsilon_k)^{3/2}} \left[1 - \ln(2\sqrt{2\epsilon_k r}) \right] \approx \frac{Z}{(2\epsilon_k)^{3/2}} \left[1 - \ln(4\epsilon_k t_{\text{prop}}) \right]. \quad (1.12)$$

Thus, according to the correction $t_{\text{cor}}^{\text{Coul}}$ a finite atomic time delay value τ_{at} is not defined for the Coulomb potential and further we would come to the conclusion that $\tau_{\text{at}} \neq \tau_{\text{W}}$. However, one should keep in mind that the correction is a universal contribution and depends neither on the initial state i nor the final state characterized by the angular momentum ℓ .

In Fig. 1.1 we show a typical streaking spectrogram corresponding to the photoionization of the hydrogen $1s$ state initiated by an XUV pulse with a photon energy $\hbar\omega_{\text{XUV}} = 27.211$ and a probing 800 nm IR field. It reveals a finite streaking time delay $\tau_S = -34.5$ as. The relation $\tau_S = \tau_{\text{at}} + \tau_{\text{CLC}}$ with the two finite contributions τ_{at} and τ_{CLC} is not in line with the Coulomb correction $t_{\text{cor}}^{\text{Coul}}$ that would depend on the propagation time according to Eq. (1.12).

Therefore, we checked carefully that the streaking time delay did not change for different propagation times $t_{\text{prop}} > d_{\text{IR}}$ where d_{IR} is the duration of IR pulse. Consequently, due to the action of the IR field, the dependence on the propagation time t_{prop} according to Eq. (1.12) somehow disappears. Looking at the structure of the Coulomb correction delay and taking into account the independence on the initial and final states it is natural to associate $t_{\text{cor}}^{\text{Coul}}$ with the CLC contribution τ_{CLC} to the streaking delay.

We consider now a streaking process with a particular delay time $\Delta_{\text{XUV-IR}}$ between the maxima of the XUV and IR fields and assume photoionization at $t_0 = 0$, i.e. the photoelectron in the continuum is immediately driven by the IR field with a value of the vector potential $A_{\text{IR}}(\Delta_{\text{XUV-IR}})$.

Let now introduce a time interval $t \in [\Delta_{\text{XUV-IR}}, \Delta_{\text{XUV-IR}} + t_{\text{str}}]$ where the action of the IR field can be seen adiabatically, i.e. $A_{\text{IR}}(t) \approx A_{\text{IR}}(\Delta_{\text{XUV-IR}})$. Consequently, $t_{\text{str}} \ll T_{\text{IR}}$ where $T_{\text{IR}} = 2\pi/\omega_{\text{IR}}$ is the period of the IR laser field. For different XUV photon energies between 20 eV and 140 eV, an IR photon energy $\hbar\omega_{\text{IR}} = 1.54$ eV, and a typical intensity $I_{\text{IR}} = 5 \times 10^{11}$ W/cm² we find in a numerical way that the CLC correction $\tau_{\text{CLC}} = \tau_{\text{S}}(t_{\text{prop}} > d_{\text{IR}}) - \tau_{\text{W}}^{\text{Coul}}$ is independent on the propagation time t_{prop} . It is given by the compact equation

$$\tau_{\text{CLC}}(\varepsilon_k) \approx t_{\text{cor}}^{\text{Coul}}(\varepsilon_k, r = kt_{\text{str}}) = \frac{Z}{(2\varepsilon_k)^{3/2}} [1 - \ln(0.36T_{\text{IR}})]. \quad (1.13)$$

By fitting, we conclude $t_{\text{str}} \approx 0.089T_{\text{IR}}$. How can we interpret this result?

The delay correction $t_{\text{cor}}^{\text{Coul}}$, which according to Eq. (1.12) depends on the propagation time, is mapped into the CLC delay contribution τ_{CLC} which is independent of the propagation time. However, only the interval $\Delta t = t_{\text{str}}$ which covers only a small portion of T_{IR} is captured and therefore a limited contribution to the time delay is accumulated. This statement was confirmed (in a numerical way) by Pazourek *et al.* [9, 10]. The direct consequence is that the attosecond streaking method is probing only a limited part of the ionic potential, i.e. the coupling between the Coulomb potential and the IR laser field (therefore CLC) is only effective close to the core, while there is no contribution to the delay at the asymptotic region. For a conventional streaking setup the effective distance in the ionic force field, which can be addressed, is typical below 30 a.u..

This circumstance underlines the correctness of Eq. (1.2) also for the Coulomb potential since due to the interaction with the streaking field, the propagation time dependent correction $t_{\text{cor}}^{\text{Coul}}$ is mapped onto the CLC contribution τ_{CLC} which is independent of the propagation time. All characteristics of the atomic system, i.e. the information about the initial state $|\Psi_i\rangle$ or the final state $|\Psi_f\rangle$, as well as the angular dependence, are fully incorporated in the Wigner time delay τ_{W} which is finite. Therefore, this legitimates our above definition of the atomic time delay also for long-ranged Coulomb potentials. As a consequence, the strict definition of τ_{at} according to Eq. (1.11) has to be corrected and we can conclude that $\tau_{\text{at}} \equiv \tau_{\text{W}}$.

1.3 Calculation of the atomic time delay

In this section, we focus on a proper introduction and calculation of the atomic time delay which is equivalent to the Wigner delay τ_W and represents the unique scattering properties of the considered atomic system. Therefore, the photoionization amplitude as an integral part of the time delay definition and its angular characteristics will be derived from a perturbative treatment. The CLC contribution provides no further information since it is essentially the same for every target [15] and will be not taken into account.

The wave function representing a photoelectron can be expressed as a superposition of several final partial waves:

$$\Phi(\mathbf{r}, t) = \int d\mathbf{k} a(\mathbf{k}, t) \varphi_{\mathbf{k}}^f(\mathbf{r}) e^{-i\varepsilon_{\mathbf{k}} t}, \quad (1.14)$$

where $\varphi_{\mathbf{k}}^f(\mathbf{r})$ is a set of appropriate continuum wave functions of the considered atomic system, and $a(\mathbf{k}, t)$ are the corresponding projection coefficients, which can be evaluated as [71]

$$a_i(\mathbf{k}, t) = -i \int_{-\infty}^t dt' \langle \varphi_{\mathbf{k}}^f | \hat{H}_{\text{int}}(t') | \Psi_i \rangle e^{i(\varepsilon_{\mathbf{k}} - \varepsilon_i) t'}. \quad (1.15)$$

The label i signals the photoionization process from the bound state $|\Psi_i\rangle$ with the energy eigenvalue ε_i . The kinetic energy is given by $\varepsilon_{\mathbf{k}} = k^2/2$. The time-dependent interaction Hamiltonian $\hat{H}_{\text{int}}(t)$ in the dipole approximation describes the interaction with the XUV field, which is linearly polarized in the z -direction and is characterized by the temporal envelope $E(t)$. It can be given either in the length or the velocity gauges:

$$\hat{H}_{\text{int}}(t) = \begin{cases} \hat{z}E(t) \\ \hat{p}_z A(t), \quad \text{where } A(t) = -\int_{-\infty}^t E(t') dt'. \end{cases} \quad (1.16)$$

Inserting the length gauge form of Eq. (1.16) in Eq. (1.15) and considering a field which vanishes for $|t| \rightarrow \infty$ we find a simple expression for the projection coefficients:

$$a_i(\mathbf{k}) = -i D_i(\mathbf{k}) \tilde{E}(\varepsilon_{\mathbf{k}} - \varepsilon_i), \quad (1.17)$$

which is the product of the dipole matrix element $D_i(\mathbf{k}) = \langle \varphi_{\mathbf{k}}^f | \hat{z} | \Psi_i \rangle$ and the Fourier transform $\tilde{E}(\omega)$ of the XUV field. $D_i(\mathbf{k})$ describes the transition from the initial state $|\Psi_i\rangle$ to the final continuum state $|\varphi_{\mathbf{k}}^f\rangle$ and has all information about the atomic time delay τ_W . Considering spherical symmetry the wave function of the initial state $|\Psi_i\rangle$ has a well-defined angular momentum and can be expressed as $\Psi_i(\mathbf{r}) = R_{n_i, \ell_i}(r) Y_{\ell_i m_i}(\Omega_{\mathbf{r}})$. Here $R_{n_i, \ell_i}(r)$ describes the radial part of the wave function, characterized by the principal quantum number n_i , the angular quantum number ℓ_i , and the number of nodes $n_i - \ell_i - 1$. The angular part is given by the spherical harmonic $Y_{\ell_i m_i}(\Omega_{\mathbf{r}})$ and has the well-defined orbital angular

momentum and magnetic quantum numbers ℓ_i and m_i . The corresponding bound state energy is characterized by $\varepsilon_i \equiv \varepsilon_{n_i \ell_i}$. Therefore, the magnetic substates within a subshell are degenerated concerning the energy. The partial wave expansion of the final continuum states is [15, 68]:

$$\varphi_{\mathbf{k}}^f(\mathbf{r}) = (8\pi)^{3/2} \sum_{\ell} \sum_{m=-\ell}^{\ell} i^{\ell} e^{-i\delta_{\ell}(k)} R_{k\ell}(r) Y_{\ell m}^*(\Omega_{\mathbf{k}}) Y_{\ell m}(\Omega_{\mathbf{r}}). \quad (1.18)$$

The scattering phases are given by $\delta_{\ell}(k) = \eta_{\ell}(k) + \sigma_{\ell}(k)$ and represent a sum of two contributions. The influence of the long-range Coulomb field of the residing ion on the outgoing photoelectron is characterized by the analytically known Coulomb phase shift $\sigma_{\ell}(k) = \arg[\Gamma(\ell + 1 - i/k)]$ [68], where $\Gamma(x) = \int_0^{\infty} dt t^{x-1} e^{-t}$ is the complex Gamma function. The contribution $\eta_{\ell}(k)$ is a correction due to the short range deviation of the ionic potential from the pure Coulomb potential. It characterizes the unique scattering properties of the atomic system. Obviously in the case of hydrogen $\eta_{\ell}(k) = 0$.

Furthermore, the scattering phases have to fulfill the Levinson-Seaton theorem, i.e. $\eta_{\ell}(k \rightarrow 0) = \nu_{\ell}(\infty)\pi$ [72, 73]. Here $\nu_{\ell}(\infty)$ is the quantum defect due to the presence of occupied bound states with a given orbital angular momentum ℓ which perturb the energy level sequence. For a pure short-range potential the scattering phase at the zero energy is related to the number of occupied subshells with a particular ℓ and is given by $\eta_{\ell}(k \rightarrow 0) = N_{\ell}\pi$ (regular Levinson-theorem [74]). For example, in the absence of the Coulomb potential tail, the phase contribution $\eta_{\ell=1}(k)$ (belonging to the transition ns to kp) would tend to π for the zero energy in the case of neon because there is one np subshell occupied ($n = 2$). In the same vein for argon $\eta_{\ell=1}(k)$ would tend to 2π for $k \rightarrow 0$ because two p subshells ($2p$ and $3p$) are occupied. When the Coulomb potential is taken into account the sequence of energy levels with a specific orbital angular momentum ℓ can be fitted to $\varepsilon_{n\ell} = -(n - \nu_{\ell}(n))^{-2}$ to find the quantum defect $\nu_{\ell}(\infty)$.

The $R_{k\ell}(r)$ are the radial wave functions corresponding to the set of the final continuum states $|\varphi_{\mathbf{k}}^f\rangle$. They are normalized to the energy by the condition $\langle R_{k,\ell} | R_{k',\ell} \rangle = \delta(\varepsilon_k - \varepsilon_{k'})$. Although no exact analytical solution for $R_{k\ell}(r)$ can be derived, the behavior in the asymptotic limit is characterized by

$$\lim_{r \rightarrow \infty} R_{k,\ell}(r) = \frac{N_k}{r} \sin[kr + \Phi_{\ell}(r, k)], \quad (1.19)$$

where the phase of the wave function is given by

$$\Phi_{\ell}(r, k) = \log(2kr)/k - \ell\pi/2 + \delta_{\ell}(k). \quad (1.20)$$

This phase also includes the logarithmic divergence, which is characteristic for the Coulomb potential of the ionic core in the asymptotic region. $N_k = \sqrt{2/\pi k}$ stands here for the normalization constant.

In the next step, we find an expression for the transition matrix element $D_i(\mathbf{k})$ in the case of the linearly polarized laser pulse. The corresponding dipole operator is given by $\hat{z} = \sqrt{4\pi/3}rY_{10}(\Omega_{\mathbf{r}})$. Using the partial wave expansion in Eq. (1.18) and performing the angular integration in the r -space we obtain:

$$D_i(\mathbf{k}) = (8\pi)^{3/2} \sum_{\ell=\ell_i\pm 1} i^{-\ell} e^{i\delta_i(k)} Y_{\ell m_i}(\Omega_{\mathbf{k}}) \begin{pmatrix} \ell & 1 & \ell_i \\ -m_i & 0 & m_i \end{pmatrix} d_{\ell, n_i \ell_i}(k). \quad (1.21)$$

Here we introduce the reduced radial matrix elements in length form [40, 75]:

$$d_{\ell, n_i \ell_i}(k) = \langle k\ell || d^{(r)} || n_i \ell_i \rangle = \sqrt{(2\ell+1)(2\ell_i+1)} \begin{pmatrix} \ell & 1 & \ell_i \\ 0 & 0 & 0 \end{pmatrix} \int_0^\infty dr r^3 R_{k\ell}(r) R_{n_i, \ell_i}(r). \quad (1.22)$$

This formula results from the angular integration [76]:

$$\int d\Omega_{\mathbf{r}} Y_{\ell_1 m_1}^*(\Omega_{\mathbf{r}}) Y_{\ell_2 m_2}(\Omega_{\mathbf{r}}) Y_{\ell_3 m_3}(\Omega_{\mathbf{r}}) = \sqrt{\frac{(2\ell_1+1)(2\ell_2+1)(2\ell_3+1)}{4\pi}} \begin{pmatrix} \ell_1 & \ell_2 & \ell_3 \\ 0 & 0 & 0 \end{pmatrix} \\ \times \begin{pmatrix} \ell_1 & \ell_2 & \ell_3 \\ -m_1 & m_2 & m_3 \end{pmatrix}, \quad (1.23)$$

where the Wigner $3j$ symbols are zero unless $-m_1 + m_2 + m_3 = 0$ and $|\ell_1 - \ell_2| \leq \ell_3 \leq \ell_1 + \ell_2$ [76]. In our particular case, this leads to the well-known dipole selection rules for linearly polarized light and the final state f , i.e. $\ell_f = \ell_i \pm 1$ and $m = m_i$. That means the photoionization process does not change the magnetic state.

Let $\mu_i(\varepsilon_k, \Omega_{\mathbf{k}})$ be the phase of the transition matrix element $D_i(\mathbf{k})$ corresponding to the respective subshell i , i.e. $\mu_i(\varepsilon_k, \Omega_{\mathbf{k}}) = \arg[D_i(\mathbf{k})] \equiv \arg[a_i(\mathbf{k})]$. According to Eq. (1.8) the Wigner time delay τ_W (and therefore the atomic time delay) derives from the energy derivative of the phase $\mu_i(\varepsilon_k, \Omega_{\mathbf{k}})$. It is immediately obvious that the delay is dependent on the momentum \mathbf{k} of the photoelectron and therefore is an angular dependent quantity. In the case, the final state f is characterized by only one partial wave Eq. (1.8) reduces to Eq. (1.7). Note that the definition of the time delay in Eq. (1.8) is also valid for the velocity form of the matrix element, i.e. $\tau_W^{(\nabla)}(\mathbf{k}) = \frac{\partial}{\partial \varepsilon_k} \arg \left[\langle \Phi_{\mathbf{k}}^f | \hat{p}_z | \Psi_i \rangle \right]$.

We can write the spherical harmonics $Y_{\ell m}(\Omega_{\mathbf{k}})$ as $N_\ell^m P_\ell^m(\cos \vartheta_{\mathbf{k}}) e^{im\varphi_{\mathbf{k}}}$, where $\Omega_{\mathbf{k}} \equiv (\vartheta_{\mathbf{k}}, \varphi_{\mathbf{k}})$ and $P_\ell^m(x)$ are the associated Legendre polynomials. Introducing the real amplitudes

$$S_{\ell_i \pm 1}(\varepsilon_k, \vartheta_{\mathbf{k}}) = \begin{pmatrix} \ell_i \pm 1 & 1 & \ell_i \\ -m_i & 0 & m_i \end{pmatrix} d_{\ell_i \pm 1, n_i \ell_i} N_{\ell_i \pm 1}^{m_i} P_{\ell_i \pm 1}^{m_i}(\cos(\vartheta_{\mathbf{k}})) \quad (1.24)$$

and the phase factors

$$\phi_{\ell_i \pm 1}(\varepsilon_k, \varphi_{\mathbf{k}}) = \delta_{\ell_i \pm 1}(k) - (\ell_i \pm 1)\pi/2 + m_i \varphi_{\mathbf{k}} \quad (1.25)$$

we find an equation for the phase of the transition matrix element:

$$\mu_i(\varepsilon_k, \Omega_{\mathbf{k}}) = \text{atan} \left[\frac{\sum_{\ell=\ell_i \pm 1} S_{\ell}(\varepsilon_k, \vartheta_{\mathbf{k}}) \sin(\phi_{\ell}(\varepsilon_k, \varphi_{\mathbf{k}}))}{\sum_{\ell=\ell_i \pm 1} S_{\ell}(\varepsilon_k, \vartheta_{\mathbf{k}}) \cos(\phi_{\ell}(\varepsilon_k, \varphi_{\mathbf{k}}))} \right]. \quad (1.26)$$

Equation (1.26) reveals that the phase of the transition matrix elements strongly depends on the scattering phases $\delta_{\ell_i \pm 1}$ of the exit channels with the quantum numbers $\ell = \ell_i \pm 1$ and the ratio of the amplitudes $S_{\ell_i+1}(\varepsilon_k, \vartheta_{\mathbf{k}})/S_{\ell_i-1}(\varepsilon_k, \vartheta_{\mathbf{k}})$. A closer inspection of the energy derivative of $\mu_i(\varepsilon_k, \Omega_{\mathbf{k}})$ at a particular energy shows that the time delay only depends on the angle $\vartheta_{\mathbf{k}}$ between the asymptotic momentum of the photoelectron and the laser polarization axis, but not on the polar angle $\varphi_{\mathbf{k}}$ which reflects the cylindrical symmetry of the photoionization process.

In the special case for photoionization from the initial state with $\ell_i = m_i = 0$ we find only one final exit channel characterized by $\ell = 1$ and $m = 0$. Thus, the phase of the transition matrix element is given by $\mu_{\ell_i=0, m_i=0}(\varepsilon_k, \Omega_{\mathbf{k}}) = \phi_{\ell=1}(\varepsilon_k, \varphi_{\mathbf{k}}) = \delta_1(k) - \pi/2$ and is independent of the whole solid angle. The corresponding time delay can be computed by $\tau_{\mathbf{W}}^{\ell_i=0, m_i=0} = \frac{\partial}{\partial k} \delta_1(k)$, which reflects the primary definition of the time delay in Eq. (1.7) and shows that it strongly depends on the properties of the scattering phases. The same arguments work for the case of the initial states with $\ell_i = 1$ and $m_i = \pm 1$ where we also find only one final partial wave channel and therefore no angular modulation.

An effective dependence of the time delay on the angle $\vartheta_{\mathbf{k}}$ occurs only in the case when we find an interference between two different final states, i.e. $\ell_i > 0$. Within this perturbative treatment, the phase factor $m_i \varphi_{\mathbf{k}}$ has no impact on the resulting time delay of the photoionization process. Therefore, we can state $\tau_{\mathbf{W}}^{\ell_i, m_i}(\varepsilon_k, \Omega_{\mathbf{k}}) \equiv \tau_{\mathbf{W}}^{\ell_i, m_i}(\varepsilon_k, \vartheta_{\mathbf{k}})$.

The time delay is, in general, a function of the energy. The characteristic (and measured) time

ionization probability $w_i(\varepsilon_k, \vartheta_{\mathbf{k}}) = |a_i(\mathbf{k})|^2$. The ionization probability shows an intrinsic angular dependence due to the directional dependence of the projection coefficients $a_i(\mathbf{k})$. These probabilities are peaked around the so-called center of energy (COE) $\varepsilon_{\text{COE}} = \hbar\omega_{\text{XUV}} + \varepsilon_i$, which is a consequence of the energy conversion. The peaks are not sharp because they represent the spectral width of the short pulse (cf. (1.17)). Furthermore, it is reasonable to sum over all possible initial states due to the degeneracy with respect to the magnetic quantum number m_i :

$$\tau_{\mathbf{W}}^i(\vartheta_{\mathbf{k}}) = \frac{\int d\varepsilon_k \sum_{m_i}^{\text{occ.}} w_{\ell_i, m_i}(\varepsilon_k, \vartheta_{\mathbf{k}}) \tau_{\ell_i, m_i}(\varepsilon_k, \vartheta_{\mathbf{k}})}{\int d\varepsilon_k \sum_{m_i}^{\text{occ.}} w_{\ell_i, m_i}(\varepsilon_k, \vartheta_{\mathbf{k}})}. \quad (1.27)$$

1.4 Numerical extraction of the time delay

In addition to the approximate analytical solution of the Schrödinger equation via the perturbation theory, we want to employ a numerical method to extract the time delay information. The following equation has to be solved:

$$\begin{aligned} i\frac{\partial}{\partial t}\Psi(\mathbf{r},t) &= \hat{H}(t)\Psi(\mathbf{r},t) \\ &= [\hat{H}_0 + \hat{H}_{\text{int}}(t)]\Psi(\mathbf{r},t), \end{aligned} \quad (1.28)$$

where the possible interaction Hamiltonians are given in Eq. (1.16). The field-free Hamiltonian \hat{H}_0 incorporates the atomic potential $V(r)$. The TDSE is discretized on a spatial grid with a step size $h = 0.02$ a.u. and a maximal box size $R_{\text{max}} = 1000$ a.u., while the temporal grid is also equidistant. For every time step t_n the full wave function corresponding to an initial state i can be represented as

$$\Psi(\mathbf{r},t_n) = \sum_{\ell=0}^{L_{\text{max}}} \sum_{m=-\ell}^{\ell} f_{\ell}(r,t_n) Y_{\ell,m}(\Omega_{\mathbf{r}}). \quad (1.29)$$

Here the functions $f_{\ell}(r,t_n)$ represent the radial part defined on the points of the radial grid. For $t \rightarrow -\infty$ we define that $\Psi(\mathbf{r},t) = \Psi_i(\mathbf{r})$.

The choice of the gauge within interaction Hamiltonian \hat{H}_{int} has a significant impact on the convergence properties which are characterized by maximal number L_{max} of needed partial waves. Although both gauges deliver the same results, a much smaller number of partial waves is needed when using the velocity gauge [77, 78]. For the moderate intensities used below $L_{\text{max}} = 8$ in the case of the velocity gauge is sufficient while we need 13 partial waves for the length gauge.

To propagate the wave function in Eq. (1.29) numerically the so-called Matrix iteration method (MIM) was employed [78]. The method was already successfully used for the effective solution of the TDSE in strong fields [79] as well as for time delay calculations [62, 80].

The key point for developing the MIM procedure is the expression of the wave function at the time step t_{n+1} with the help of the Crank-Nicolson (CN) propagator [81]:

$$\Psi(\mathbf{r},t_{n+1}) = \frac{1 - i\hat{H}(t_n + \Delta t/2)\Delta t/2}{1 + i\hat{H}(t_n + \Delta t/2)\Delta t/2}\Psi(\mathbf{r},t_n), \quad (1.30)$$

where Δt is the step size of the temporal grid. Now, the denominator in Eq. (1.30) can be separated:

$$1 + i\hat{H}(t_n + \Delta t/2)\Delta t/2 = \hat{A} + \hat{B}, \quad (1.31)$$

where $\hat{A} = 1 + \hat{H}_0 \Delta t / 2$ is the time-independent part and $\hat{B} = i\hat{H}_{\text{int}}(t_n + \Delta t / 2) \Delta t / 2$ incorporates the time-dependent interaction. Using the Neumann expansion

$$(\hat{A} + \hat{B})^{-1} = \hat{A}^{-1} - \hat{A}^{-1} \hat{B} \hat{A}^{-1} + \hat{A}^{-1} \hat{B} \hat{A}^{-1} \hat{B} \hat{A}^{-1} \dots, \quad (1.32)$$

we avoid the problem of computing the matrix inverse of the operator $1 + i\hat{H}(t_n + \Delta t / 2) \Delta t / 2$ in the expression of the Crank-Nicolson propagator. In fact, the computing of the matrix inverse at every time step t_n is substituted by the repeated multiplication of the static matrix inverse \hat{A}^{-1} by the time-dependent operator \hat{B} . For the radial wave functions $f_\ell(r, t_n)$ this matrix inversion of \hat{A} is very simple since the free-field Hamiltonian \hat{H}_0 is discretized on the radial grid by using the three-point finite difference formula for the first and second spatial derivatives [82]. Therefore, the operator \hat{A} is diagonal in ℓ and tridiagonal in space. Consequently, we find the inverse of \hat{A} by computing the inverse of a tridiagonal matrix which has to be performed only one time and can be stored.

We consider now an XUV pulse which is switched on for times $t \in [-T_{\text{XUV}}, T_{\text{XUV}}]$. To obtain the time delay information, every initial state i with $\Psi(\mathbf{r}, t \rightarrow -\infty) = \Psi_i(\mathbf{r})$ corresponding to the considered subshell is propagated from $t = -T_{\text{XUV}}$ to $t = T_{\text{XUV}}$ in the presence of the ionizing XUV field which enters the interaction Hamiltonian \hat{H}_{int} . After the photoelectron wave packet is fully formed, the solution $\Psi(\mathbf{r}, t > T_{\text{XUV}})$ is projected on a set of appropriate continuum wave functions $\varphi_{\mathbf{k}}^f(\mathbf{r})$. Consequently, we obtain the projection coefficients $a_i(\mathbf{k}, t)$ corresponding to the photoionization of an electron originating from an initial state i of a subshell [cf. Eq. (1.15)]. By computing now the phase $\mu_i(\mathbf{k}) = \arg[a_i(\mathbf{k})]$ we can extract the time delay information with the aid of the energy derivative. This propagation procedure has to be repeated for every possible initial state within the considered subshell. The evaluation of Eq. (1.27) delivers then the full time delay corresponding to the photoionization of a particular subshell.

The atomic potential used for the description of the neon atom below is a parametrized optimized effective potential [83]. The coefficients of the parametrization are determined in a way to match the experimental energy eigenvalues of corresponding atoms. The influence of the electronic restructuring of the remaining ion due the electron emission cannot be addressed within this scheme. This effective single-particle potential was already used in the theoretical description of the Wigner time delay [12] and yielded to reasonable results.

1.5 Influence of multielectron effects on the time delay

After introducing the time delay as a quantity consisting of two contributions we can include correlation effects on the time-independent level for the atomic (Wigner) time delay τ_{W} . Especially in the case of the argon atom, it becomes apparent that multielectron effects play

a crucial role in the accurate description of the photoionization and the corresponding time delay [4, 5, 16, 17].

For an atom of the charge Z and the number of N electrons interacting via the Coulomb interaction we have to solve the stationary Schrödinger equation with the Hamiltonian

$$\hat{H} = -\sum_j^N \left(\frac{\nabla_j^2}{2} + \frac{Z}{r_j} \right) + \frac{1}{2} \sum_{j=1}^N \sum_{j \neq k}^N \frac{1}{|\mathbf{r}_j - \mathbf{r}_k|} \quad (1.33)$$

and the N -body wave function Ψ . Here \mathbf{r}_j denotes the position of the j -th individual electron.

Within the Hartree-Fock (HF) approximation, it is assumed that all N electrons move in a self-consistent field according to [40, 75]

$$\begin{aligned} \hat{H}^{\text{HF}}\Psi(x_1, \dots, x_N) &\equiv \sum_{j=1}^N \left[-\frac{\nabla_j^2}{2} - \frac{Z}{r_j} + U_{\text{HF}}(x_j) \right] \Psi(x_1, \dots, x_N) \\ &= E^{\text{HF}}\Psi(x_1, \dots, x_N) \end{aligned} \quad (1.34)$$

where the wave function $\Psi(x_1, \dots, x_N)$ is the Slater determinant formed out of one-particle wave functions $\varphi_j(x_j)$:

$$\Psi(x_1, \dots, x_N) = \begin{vmatrix} \varphi_1(x_1) & \varphi_1(x_2) & \dots & \varphi_1(x_N) \\ \varphi_2(x_1) & \varphi_2(x_2) & \dots & \varphi_2(x_N) \\ \vdots & \vdots & \dots & \vdots \\ \varphi_N(x_1) & \varphi_N(x_2) & \dots & \varphi_N(x_N) \end{vmatrix}. \quad (1.35)$$

The variable $x_j \equiv (\mathbf{r}_j, \sigma_j)$ incorporates the coordinates of space and spin of the electron state j . Due to the requirements of the Pauli principle, the wave function is asymmetric with respect to an interchange between two electron state positions, i.e.

$$\Psi(x_1, x_2, \dots, x_i, \dots, x_j, \dots, x_N) = -\Psi(x_1, x_2, \dots, x_j, \dots, x_i, \dots, x_N). \quad (1.36)$$

The self-consistent potential $U_{\text{HF}}(x_j)$ as a non-local operator is characterized by the single-particle wave functions φ_j of all atomic states and can be found through the minimization of the atom energy. The total energy of the ground state is given by

$$E_0^{\text{HF}} = \frac{\langle \Psi_0^{\text{HF}} | \hat{H}^{\text{HF}} | \Psi_0^{\text{HF}} \rangle}{\langle \Psi_0^{\text{HF}} | \Psi_0^{\text{HF}} \rangle}. \quad (1.37)$$

Small variations with respect to the wave function φ_j under the condition of the minimal energy lead to a set of equations for the electronic wave functions $\varphi_j(\mathbf{r})$ with the corresponding

spin projections σ_j , called the Hartree-Fock equations:

$$\left(-\frac{\nabla^2}{2} - \frac{Z}{r}\right) \varphi_j(\mathbf{r}) + \sum_{k=1}^N \int d\mathbf{r}' \frac{\varphi_k^*(\mathbf{r}')}{|\mathbf{r}' - \mathbf{r}|} \times [\varphi_k(\mathbf{r}') \varphi_j(\mathbf{r}) - \varphi_j(\mathbf{r}') \varphi_k(\mathbf{r})] = E_j \varphi_j(\mathbf{r}). \quad (1.38)$$

The left side consists of four terms. The first and the second characterize the kinetic energy contribution and the electron-ion potential. The third contribution is called Hartree term and describes the electrostatic potential due to the charge cloud of the N electrons. However, it includes also the unphysical self-interaction of electrons in the case of $k = j$ which is canceled by the exchange term, i.e. the last term of the left-hand side. The E_j on the right-hand side is the HF-energy of the electron state.

This approximate mean-field description of the atom by the HF-hamiltonian together with the wave function $\Psi(x_1, \dots, x_N)$ does not contain the whole interaction between the electrons because

$$\sum_j U_{\text{HF}}(x_j) \neq \frac{1}{2} \sum_j^N \sum_{k \neq j}^N \frac{1}{|\mathbf{r}_j - \mathbf{r}_k|}. \quad (1.39)$$

and therefore $\hat{H}^{\text{HF}} \neq \hat{H}$. Consequently, the Hartree-Fock approximation does not account fully for correlation between the electron states by assuming a single-determinant form for the many-body wave function. This is reflected in some shortcomings in describing the electronic structure [40, 75].

By introducing the Fermi level E_f as the filled level with the highest energy, we introduce the class of *bound states* for all electronic states $\varphi_j(\mathbf{r})$ with energies $E_j \leq E_f$. For atoms, the electron energy E_j is characterized by the principal quantum number n_j and the orbital angular quantum number ℓ_j . The number of nodes of the radial part of the wave function is determined by $n - \ell - 1$. The one-particle wave functions are orthogonal and normalized according to

$$\int d\mathbf{r} \varphi_j^*(\mathbf{r}) \varphi_k(\mathbf{r}) = \delta_{jk}. \quad (1.40)$$

The solutions of Eq. (1.38) for $E_j > E_f$ characterize the *excited states*, i.e. in that case φ_j describes the wave function of the surplus electron state in the field of $N - 1$ residual electrons of the atom. We call it *frozen-core* approximation when the remaining electrons are unaffected by the excitation (a hole-electron pair is created) and form a fixed field. Furthermore, we can distinguish between the discrete ($E_j < 0$) and continuous ($E_j > 0$) spectrum. The discrete solutions are normalized in accordance with Eq. (1.40) and have a well-defined energy. In contrast, in the case of $E_j > 0$ solutions exist for any value. For large distances from the atom, the corresponding wave functions oscillate and are normalized according to

$$\int d\mathbf{r} \varphi_E^*(\mathbf{r}) \varphi_{E'}(\mathbf{r}) = \delta(E - E'). \quad (1.41)$$

The wave functions of both the ground and the excited states for a given spin projection σ_j and $E_j < 0$ can be represented as a product of a radial part and an angular part, i.e. $\varphi_j(\mathbf{r}) = R_{n_j\ell_j}(r)Y_{\ell_j m_j}(\Omega_{\mathbf{r}})$. In the case of the continuum states the representation of the spectrum is given by the partial wave expansion (cf. Eq. (1.18)).

Interactions with an electromagnetic field can now be described by matrix elements as introduced in Eq. (1.15) by just replacing the single particle wave functions with HF wave functions. In this thesis the HF wave functions of the bound and excited spectra were computed with the methods of Chernysheva *et al.* [84, 85].

The first step to introduce correlation effects in the HF scheme is the Random Phase Approximation with Exchange (RPAE). In principle, it is a generalization of the Hartree-Fock approximation in a weak non-stationary field with the assumption that the many-body wave function in the presence and absence of the field is always a Slater determinant built by one-particle wave functions φ_j . The second assumption is that the temporal variation due the action of the electromagnetic field is small, i.e. $|\varphi_j(t) - \varphi_j| \ll \varphi_j$. Under these conditions, the RPAE equations are derived from the HF equations [40].

To describe the photoionization process more accurate, the reduced matrix element $d_{\ell, n_i \ell_i}(k)$ (cf. Eq. (1.22)), which describes the transition from a bound state $|\Psi_i\rangle$ to a final state in the continuum $|\varphi_k^f\rangle$ due to the action of the XUV pulse, has to be replaced by the screened matrix element $D_{\ell, n_i \ell_i}(k)$. This reduced RPAE matrix element accounts for the correlation process between the various valence subshells to the first order. It is defined by the following self-consistent equation:

$$D_{\ell, n_i \ell_i}(k) = d_{\ell, n_i \ell_i}(k) + \lim_{\varepsilon \rightarrow 0^+} \sum_{n_j \ell_j}^{\text{occ.}} \sum_{\ell'} \int d\mathbf{k}' k' \times \left[\frac{D_{\ell', n_j \ell_j}(k') \langle n_j \ell_j, k\ell || V || k' \ell', n_i \ell_i \rangle}{\omega_{\text{XUV}} - \varepsilon_{k'} + \varepsilon_j + i\varepsilon} + \frac{D_{n_j \ell_j, \ell'}(k') \langle k' \ell', k\ell || V || n_j \ell_j, n_i \ell_i \rangle}{\omega_{\text{XUV}} + \varepsilon_{k'} - \varepsilon_j} \right]. \quad (1.42)$$

The indices i and j denote for valence orbitals and the sum/integral sign stands for the summation over all discrete excited states with energies $\varepsilon_k = \varepsilon_{n' \ell'}$ as well as integration over the continuum states with the energy $\varepsilon_k = k^2/2$. All used single particle wave functions are in the HF approximation. The whole process is depicted graphically in Fig. 1.2.

The first term of Eq. (1.42) is the reduced dipole matrix $d_{\ell, n_i \ell_i}(k)$, which describes the transition from the bound state i to the continuum in the HF approximation. The second term of Eq. (1.42) describes the time-forward process and is characterized by the reduced Coulomb matrix elements $\langle n_j \ell_j, k\ell || V || k' \ell', n_i \ell_i \rangle$ which is the difference between the direct and exchange Coulomb matrix elements. The direct Coulomb interaction matrix is given by

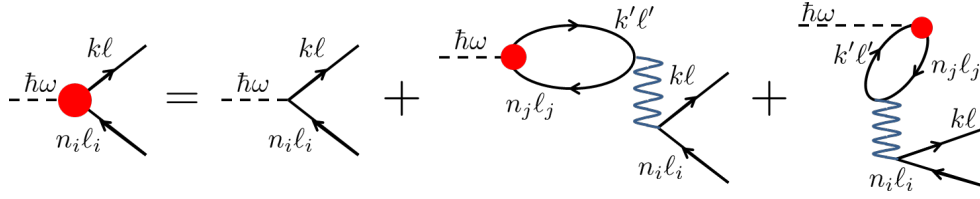


Fig. 1.2 Illustration of RPAE equations. The straight lines with an arrow to the right represent a continuum state, while an arrow to the left stands for a bound (hole) state. The curly line displays the Coulomb interaction while a dashed line exhibits a photon with the energy $\hbar\omega$. The filled circle represents the correlated matrix element while the bare reduced matrix element is displayed by the bifurcation. The time axis goes from left to right.

[40]:

$$\begin{aligned} \langle n_j \ell_j k \ell || U || k' \ell' n_i \ell_i \rangle &= \sqrt{(2\ell + 1)(2\ell' + 1)(2\ell_i + 1)(2\ell_j + 1)} \begin{pmatrix} \ell & 1 & \ell_i \\ 0 & 0 & 0 \end{pmatrix} \\ &\times \begin{pmatrix} \ell' & 1 & \ell_j \\ 0 & 0 & 0 \end{pmatrix} R_{\ell, \ell', \ell_i, \ell_j}(\boldsymbol{\varepsilon}_k, \boldsymbol{\varepsilon}_{k'}, n_i, n_j), \end{aligned} \quad (1.43)$$

where $R_{\ell, \ell', \ell_i, \ell_j}(\boldsymbol{\varepsilon}_k, \boldsymbol{\varepsilon}_{k'}, n_i, n_j)$ is the radial Slater integral:

$$R_{\ell, \ell', \ell_i, \ell_j}(\boldsymbol{\varepsilon}_k, \boldsymbol{\varepsilon}_{k'}, n_i, n_j) = \int_0^\infty dr R_{k\ell}(r) R_{k'\ell'} \int_0^r dr' \frac{r <}{r >} R_{n_i \ell_i}(r) R_{n_j \ell_j}(r). \quad (1.44)$$

In the exchange Coulomb matrix element simply the states $|k\ell\rangle$ and $|n_j\ell_j\rangle$ have to be swapped. In principle in the time forward process after absorption of a photon, the following interelectron interaction leads to a creation of a virtual hole-electron pair in the neighboring subshell. The process is shown in the second graph of Fig. 1.2.

The third term of the RPAE equation (1.42) represents the time-reversed process [the third graph of Fig. 1.2] where the virtual hole-electron pair creation due interelectron interaction takes place before the photon is absorbed. It is characterized by the reduced Coulomb matrix element $\langle k'\ell', k\ell || V || n_j\ell_j, n_i\ell_i \rangle$ and $D_{n_j\ell_j, \ell'}(k') = \langle n_j\ell_j || D || k'\ell' \rangle$. The time-forward process is the dominant contribution to the photoionization process since it conserves the energy of the system while the time-reversed process is virtual [16, 40]. The system of integral equations in Eq. (1.42) was solved with the methods of Ref. [75].

The energy integration in the time-forward term contains a pole with the consequence that the whole reduced RPAE matrix element is complex. Thus, $D_{\ell, n_i \ell_i}(k)$ can be expressed as $|D_{\ell, n_i \ell_i}(k)| e^{i\delta_\ell^{\text{RPAE}}(k)}$ and we find an additional spectral phase. The whole RPAE dipole

matrix element has the form (cf. Eq. (1.21))

$$D_i^{\text{RPAE}}(\mathbf{k}) = \sqrt{\frac{(2\pi)^3}{k}} \sum_{\ell=\ell_i \pm 1} i^{-\ell} e^{i(\delta_\ell^{\text{HF}}(k) + \delta_\ell^{\text{RPAE}}(k))} \times \begin{pmatrix} \ell & 1 & \ell_i \\ -m_i & 0 & m_i \end{pmatrix} Y_{\ell m_i}(\Omega_{\mathbf{k}}) |D_{\ell, m_i \ell_i}(k)|. \quad (1.45)$$

All the steps from Eq. (1.24) to Eq. (1.27) can be repeated and we obtain the angular characteristics of the Wigner time delay $\tau_{\text{W}}^i(\vartheta_{\mathbf{k}})$ corresponding to the photoionization from a subshell i in the RPAE.

1.6 Angular dependence of the atomic time delay

1.6.1 Neon

Neon was chosen as a first system to investigate the angular dependence of the time delay. It is a natural choice since the corresponding relative time delay between the photoionization of the $2s$ and $2p$ subshell was measured by Schultze *et al.* [3] and triggered a large research interest because up to date it can not be reproduced by theoretical methods.

Most theoretical results were computed in the forward direction, i.e. $\vartheta = 0^\circ$. Kheifets *et al.* [12, 16] obtained 8.4 as with the help of the RPAE method and therefore a similar treatment as used in this thesis. The aim is to analyze whether the angular dependence has some influence on the resulting time delay since in the measurement the incoming signal is an average over all contributions of photoelectrons within the detection (acceptance) angle ϑ_{max} . The linearly polarized XUV field which ionizes the target atom is modeled as

$$E_{\text{XUV}}(t) = E_0 \cos^2\left(\frac{\pi t}{2T_{\text{XUV}}}\right) \cos(\omega_{\text{XUV}} t) \quad (1.46)$$

for all times within the interval $[-T_{\text{XUV}}, T_{\text{XUV}}]$ and zero otherwise. To mimic the experiment [3] suitable parameters were chosen such that the pulse has a full width at half maximum (FWHM) of 182 as. The amplitude of the electric field is 0.12 a.u. which gives us a peak intensity of $5 \times 10^{14} \text{ W/cm}^2$ and justifies the perturbative treatment.

In Fig. 1.3 the explicit angular dependence of the time delays corresponding to the $2s$ and the three possible $2p$ initial states of neon is shown. The used photon energy of 106 eV is in agreement with the experiment [3]. We compare here the results within the RPAE with the time delays obtained by numerical simulations of the 3D Schrödinger equation with the aid of the MIM technique introduced in the fourth section of this chapter. Although the RPAE has a more advanced theoretical background because it treats correlation effects to a first order, this comparison is justified. Previous studies showed that in neon

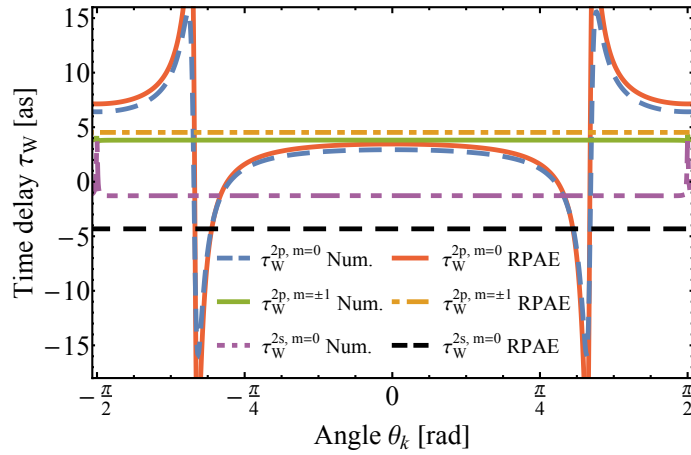


Fig. 1.3 Angular dependence of the time delays corresponding to photoelectrons liberated from the different initial states of the $2s$ and $2p$ subshells in neon. The photon energy $\hbar\omega_{\text{XUV}} = 106 \text{ eV}$. Results within the RPAE and numerical calculations are shown.

the correction due to the intershell correlation effects has only a minor impact on the description of the photoionization process of the $2p$ subshell but a significant contribution to the $2s$ photoionization [12, 16]. Nevertheless, from Eq. (1.26) we know that any angular dependence of the relative time delay $\tau_{\text{W}}^{2p-2s} \equiv \tau_{\text{W}}^{2p} - \tau_{\text{W}}^{2s}$ originates from the photoionization of the $2p$ subshell since only in that case two photoionization channels can be found. Therefore, it is reasonable to compare both methods qualitatively.

The RPAE results indicate a pronounced angular modulation with $\vartheta_{\mathbf{k}}$ of the time delay corresponding to a photoelectron liberated from the initial state of the $2p$ subshell with $m_i = 0$. However, the time delays corresponding to $m_i = \pm 1$ show no dependence on the angle because they are missing the second ionization channel (only $2p \rightarrow Ed$ is possible for $m_i = \pm 1$). Due to the same circumstance the time delay of the $2s$ subshell is constant. These results are confirmed by the full numerical simulation of the photoionization process. Small differences occur around $\vartheta = \pm 90^\circ$ where the time delays corresponding to $\{\ell_i = 0, m_i = 0\}$ ($2s$) and $\{\ell_i = 1, m_i = \pm 1\}$ ($2p$) show small variations on the angle. The reason is that the associated dominating final ionization channels $\{\ell = 1, m = 0\}$ ($2s \rightarrow kp$) and $\{\ell = 2, m = \pm 1\}$ ($2p \rightarrow kd$) vanish because $Y_{10}(90^\circ, \varphi_{\mathbf{k}}) = Y_{2\pm 1}(90^\circ, \varphi_{\mathbf{k}}) = 0$. Consequently, ionization channels with higher orbital angular momentum become decisive which cannot be captured by the RPAE but by the full numerical treatment.

The time delay of the photoionization process which liberates an electron from the $2p$ initial state with $\{\ell_i = 1, m_i = 0\}$ shows substantial variations. Typically, the time delay is characterized by the dominating photoionization channel with $\ell = 2$ which is underpinned by Fano's propensity rule [86], that means the total phase of the scattering amplitude $\mu_i(\mathbf{k}) \approx \delta_{\ell=2}(k) = \delta_{\ell=2}^{\text{HF}}(k) + \delta_{\ell=2}^{\text{RPAE}}(k)$. The phases are depicted in Fig. 1.4(a) and in the case of $\ell = 2$ they both have a positive slope and lead therefore to a positive time delay

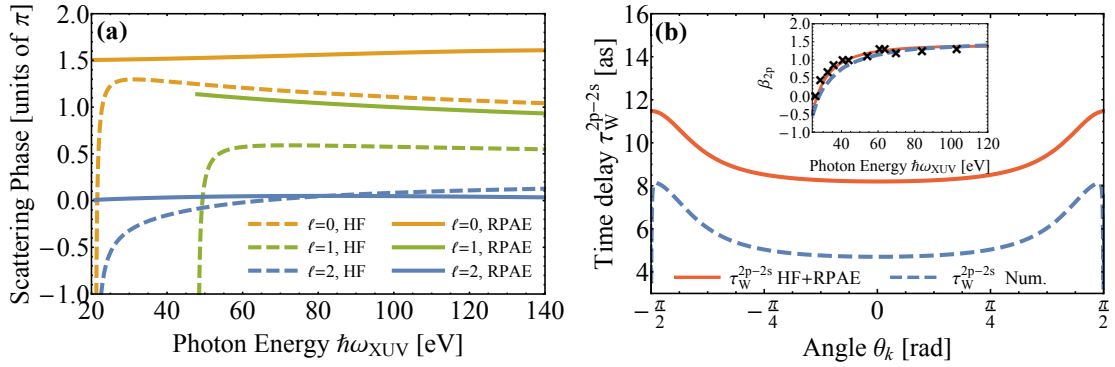


Fig. 1.4 (a) Scattering phases of the different ionization channels within HF approximation and RPAE. Both enter the evaluation of the time delay according to Eq. (1.45). (b) Angular dependence of the relative delay τ_{W}^{2p-2s} at a photon energy $\hbar\omega_{\text{XUV}} = 106$ eV as an average of the contributions of all possible initial states. The inset shows the β -parameter β_{2p} of the $2p$ subshell calculated on the basis of the pseudopotential and the RPAE model. The crosses represent the experimental data given in Ref. [87].

which is the energy derivative of $\mu_i(\mathbf{k})$. Furthermore, as an additional feature $\delta_{\ell=2}^{\text{HF}}$ fulfills the Levinson-Seaton theorem [73] since $\delta_{\ell=2}^{\text{HF}}(k \rightarrow 0) - \sigma_{\ell=2}(k \rightarrow 0) = 0$ which can be explained because in neon no d -orbital is occupied.

The very pronounced sharp delay structures around an angle $\vartheta_{\mathbf{k}} = \pm 57^\circ$ can be explained by the vanishing contribution of the typically dominating ionization channel with $\ell_f = 2$ [86]. The consequence for the sign of the time delay is evident. According to Eq. (1.26) the full phase $\mu_i(\mathbf{k})$ in this regime is now completely characterized by $\delta_{\ell=0}(k) = \delta_{\ell=0}^{\text{HF}}(k) + \delta_{\ell=0}^{\text{RPAE}}(k)$ which reveals a negative slope in Fig. 1.4(a) collectively. The direct consequence is a locally negative time delay $\tau_{\text{W}}^{\ell_i=1, m_i=0}$. In that case, we encounter the Levinson-Seaton theorem again. The difference $\delta_{\ell=0}^{\text{HF}}(k \rightarrow 0) - \sigma_{\ell=0}(k \rightarrow 0) = 1.28\pi$, i.e. the quantum defect $\mu_{\ell=0}(\infty) = 1.28$ which resonates well with the HF energy eigenvalue of the $2s$ -orbital $\epsilon_{2s}^{\text{HF}} = -1.93$ a.u..

The explicit plot of the scattering phases reveals that for the dominating ionization channel with $\ell = 2$ the additional RPAE phase $\delta_{\ell=2}^{\text{RPAE}}(k)$ is hardly distinguishable from zero (and very flat). Therefore, the correction induced by the RPAE for τ_{W}^{2p} is subtle, and a qualitative comparison of the resulting angular dependence with the single particle description (via HF or numerical solution) is permissible.

While the effect of the RPAE on the specific time delays related to the photoionization of the $2p$ subshell is subsidiary [16], we find that the energy derivative of the additional phase $\delta_{\ell=1}^{\text{RPAE}}$ has a significant influence on the resulting delay corresponding to the photoionization process of the $2s$ subshell. In this case, the total scattering phase $\mu_i(\mathbf{k})$ is according to Eq. (1.26) fully characterized by $\delta_{\ell=1}(k) = \delta_{\ell=1}^{\text{HF}}(k) + \delta_{\ell=1}^{\text{RPAE}}(k)$. Both the HF phase and the RPAE phase for $\ell = 1$, depicted in Fig. 1.4(a), have a negative slope leading therefore to a

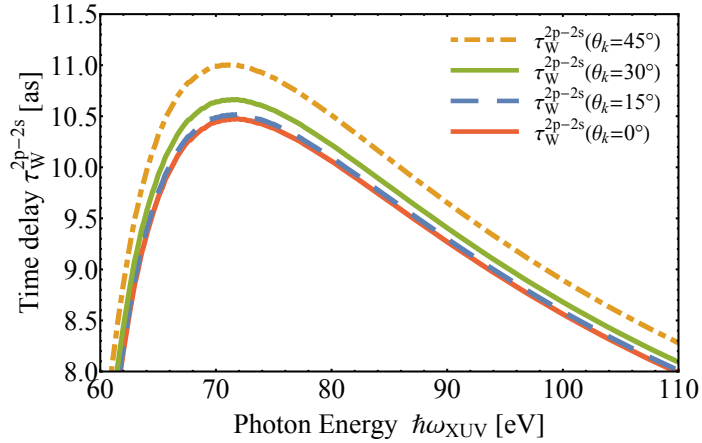


Fig. 1.5 The relative time delay τ_{W}^{2p-2s} within the RPAE in dependence on the photon energy $\hbar\omega_{\text{XUV}}$ for different angles $\vartheta_{\mathbf{k}}$.

negative time delay. The resulting quantum defect gathered from $\delta_{\ell=1}^{\text{HF}}(k \rightarrow 0) - \sigma_{\ell=1}(k \rightarrow 0) = 0.91\pi$ is $\mu_{\ell=1}(\infty) = 0.91$ which is in line with the literature [16]. By comparing the RPAE results with the full numerical simulation, we observe a visible discrepancy which is explained by the additional RPAE phase for $\ell = 1$ which is not as flat as $\delta_{\ell=2}^{\text{RPAE}}$.

In Fig. 1.4(b) the angular dependence of the full averaged (over all possible initial states) relative time delay τ_{W}^{2p-2s} is shown. It is remarkable that the formerly strong angular variation of $\tau_{\text{W}}^{m_i=1, \ell_i=0}$ is nearly compensated by the constant time delays belonging to $\{m_i = 1, \ell_i = \pm 1\}$ leading so to a relatively smooth angular dependence of the relative time delay. The discrepancy between RPAE results and full numerical simulation is explained by τ_{W}^{2s} which is significantly influenced by intershell electron correlation captured by the RPAE.

By looking at Eq. (1.27) in case of the photoionization of the $2p$ subshell, we can express the sum in the denominator as $\sum_{m_i=-1}^1 w_{\ell_i=1, m_i}(\epsilon_k, \vartheta_{\mathbf{k}}) \propto 1 + \beta_{2p}(\epsilon_k) P_2(\cos \vartheta_{\mathbf{k}})$. Here β_{2p} is the angular asymmetry parameter [40, 88] and $P_2(x) = (3x^2 - 1)/2$ the Legendre polynomial of the second order. In principle, it describes the angular dependence of the photoionization process. The calculation of the β_{2p} -parameter provides another good test for the accurateness of the description of the $2p$ photoionization process by the RPAE and the full numerical simulation. Together with a comparison with the experimental measurement [87], it is shown in the inset of Fig. 1.4(b). We see practically no difference between measurement, calculation with the RPAE and the full numerical simulation which demonstrates that the description of the electronic structure by the model potential [83] is accurate. At the photon energy $\hbar\omega_{\text{XUV}} = 106$ eV the beta parameter has the value $\beta_{2p} = 1.5$ meaning that $1/(1 + \beta_{2p} P_2(\cos \vartheta_{\mathbf{k}}))$ has two maxima at $\vartheta_{\mathbf{k}} = \pm 90^\circ$. Therefore, it is explained why the relative time delay τ_{W}^{2p-2s} increases slowly when approaching larger angles. Consequently, the numerator of Eq. (1.27) which is determined by $\sum_{m_i=-1}^1 w_{\ell_i=1, m_i}(\epsilon_k, \vartheta_{\mathbf{k}}) \tau_{\text{W}}^{\ell_i=1, m_i}(\epsilon_k, \vartheta_{\mathbf{k}})$

shows no significant angular dependence which underpins the attenuation of the pronounced angular modulation of $\tau_{\text{W}}^{\ell_i=1, m_i=0}$ due to the averaging with $\tau_{\text{W}}^{\ell_i=1, m_i=\pm 1}$.

In Fig. 1.5 the dependence of the relative time delay τ_{W}^{2p-2s} on the photon energy is depicted for different asymptotic directions $\vartheta_{\mathbf{k}}$ of the photoelectron. Two characteristics can be observed. Generally, the time delay decreases with an increasing photon energy which can be explained by the behavior of the scattering phases. For large energies, the HF phases, as well as the RPAE phases, tend to become very flat (cf. Fig. 1.4(a)) leading to very small time delays. More important is the observation that the angular dependence is very subtle yielding a negative answer regarding the question whether any angular modulation of the time delay could have an impact on the experimental measurement.

In forward direction (i.e. $\vartheta_{\mathbf{k}} = 0^\circ$) we find a relative RPAE time delay $\tau_{\text{W}}^{2p-2s} = 8.19$ as which is in good agreement with the results of Kheifets *et al.* [12, 16]. An averaging of the relative time delay within a large acceptance angle, i.e. over all angles $\vartheta_{\mathbf{k}} \in [-45^\circ, 45^\circ]$ at a photon energy of 106 eV leads to a relative time delay of $\tau_{\text{W}}^{2p-2s} = 8.51$ as while a smaller acceptance angle of $\vartheta_{\text{max}} = 20^\circ$ results in a time delay of $\tau_{\text{W}}^{2p-2s} = 8.24$ as. Thus, in the case of neon effects on the measurements due to the angular dependence of the time delay can be neglected, and it does not serve as an explanation for the discrepancy between the experimental and all theoretical results.

1.6.2 Argon

In the case of argon, the same shape and field amplitude of the electromagnetic perturbation was used. To improve the RPAE approximation we substitute the HF energy eigenvalues with the experimental ionization thresholds [16]. Therefore, the energy difference between the 3s and 3p subshells is 13.48 eV [83]. To avoid some accidental photoionization of both initial subshells (3s and 3p), we have to adjust the spectral width which has to be narrower. Therefore, we use an XUV pulse with a longer duration in comparison to the neon case. The FWHM of 300 as is sufficient.

The partial cross sections corresponding to the photoionization process of the 3s and 3p subshells are depicted in Fig. 1.6(a). Theoretically, they are calculated for a specific subshell with the quantum numbers n_i, ℓ_i according to

$$\sigma_{n_i \ell_i}(\omega) = 2.689 \frac{\omega N_i}{2\ell_i + 1} \sum_{\ell=\ell_i \pm 1} |d_{\ell, n_i \ell_i}(k)|^2, \quad (1.47)$$

where $k = \sqrt{2(\omega + \varepsilon_{n_i \ell_i})}$. Some integral features can be observed. First, the 3p partial cross section reveals a Cooper minimum, i.e. a minimum of the photoionization probability around 50 eV, while it does not exist in the case of the nodeless 2p orbital of neon [89]. Second, the correlation correction due to the RPAE changes the shape of the 3s partial cross section completely and evidencing a deep Cooper minimum around 42 eV which cannot

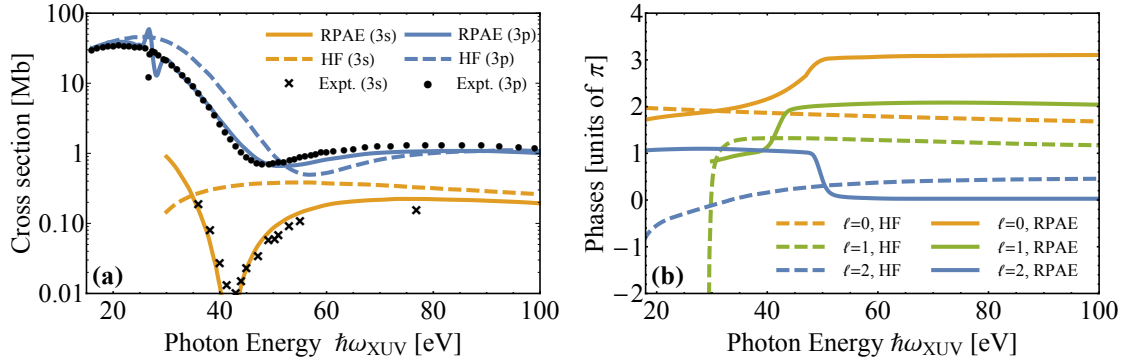


Fig. 1.6 (a) Photoionization cross sections corresponding to the $3s$ and $3p$ subshells in argon. (b) Scattering phases of argon of the different ionization channels within HF approximation and RPAE.

be captured by the HF approximation or other single-active electron approximations. In the case of both partial cross sections, the RPAE calculations reproduce the experimental measurement to a fair agreement. Therefore, we forgo the full numerical simulations for argon.

A look at the scattering phases in Fig. 1.6(b) reveals strong differences in comparison with neon. According to the Levinson theorem in the absence of the Coulomb potential the HF phase corresponding to the transition $3s \rightarrow kp$ would tend to 2π at $k \rightarrow 0$ because two p subshells are occupied. Taking the Coulomb potential into account the quantum defect is characterized by $\delta_{\ell=1}^{\text{HF}}(k \rightarrow 0) - \sigma_{\ell=1}(k \rightarrow 0) = 1.75\pi$, i.e. $\mu_{\ell=1}(\infty) = 1.75$. The RPAE phases are very different in comparison to neon because the phase $\delta_{\ell=1}^{\text{RPAE}}(k)$ makes a jump of π when the cross section goes through the Cooper minimum at 42 eV. The explanation is very simple: Imagine the photoionization amplitude $\mu_i(\varepsilon_k, \Omega_{\mathbf{k}})$ is real and had a node (Cooper minimum). In this case, it would change the sign which is similar to adding a phase factor of π in the complex number representation [46]. A similar situation can be observed in the case of the $3p$ subshell. For the transition $3p \rightarrow kd$ we find the quantum defect $\mu_{\ell=2}(\infty) = 0$ since for argon no d orbital is occupied. The corresponding RPAE phase $\delta_{\ell=2}^{\text{RPAE}}(k)$ as well as $\delta_{\ell=0}^{\text{RPAE}}(k)$ ($3p \rightarrow ks$ transition) also make a substantial jump of $-\pi$ and π , respectively, when the partial cross section passes the Cooper minimum at 50 eV. The prominent features in the RPAE phases have a significant impact on the resulting time delays. In panel Fig. 1.7(a) the time delay corresponding to the photoionization process of the $3s$ subshell is shown. It is not surprising that the τ_{W}^{3s} shows no angular dependence since we have only one photoionization channel ($3s \rightarrow kp$). The comparison between the results in HF approximation and within RPAE show the large impact of the correction due to intershell correlation effects. While the HF result is relatively flat and is comparable to the characteristics of $2s$ time delay of neon, we find a very pronounced peak of the RPAE time delay for photon energies around the Cooper minimum. The explanation is given by $\delta_{\ell=1}^{\text{RPAE}}(k)$ which makes a sudden jump of π at $\hbar\omega_{\text{XUV}} = 42$ eV. Therefore, according to

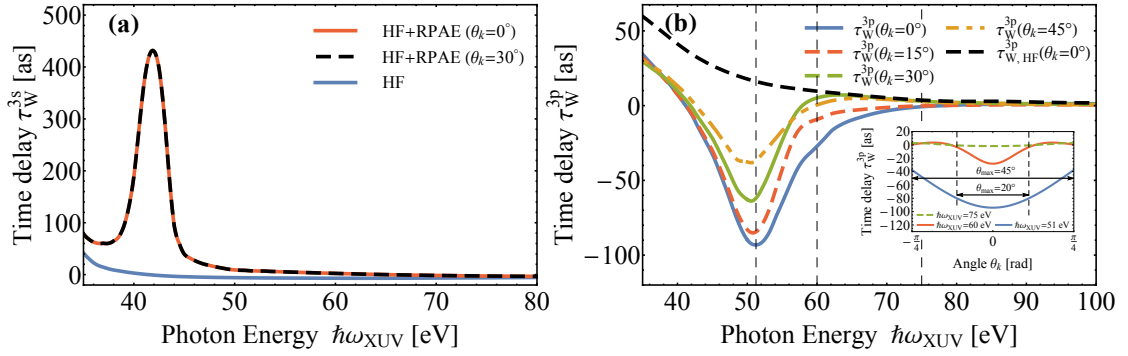


Fig. 1.7 (a) Time delay corresponding to the photoionization process of the $3s$ subshell in argon. (b) Time delay τ_{W}^{3p} for different asymptotic directions $\vartheta_{\mathbf{k}}$ of the liberated photoelectron. The inset shows the angular dependence of the full averaged delays in the case of three different photon energies around the Cooper minimum.

Eq. (1.26) the time delay $\tau_{\text{W}}^{3s} = \frac{\partial}{\partial \varepsilon_k} [\delta_{\ell=1}^{\text{HF}}(k) + \delta_{\ell=1}^{\text{RPAE}}(k)]$ shows a very distinctive positive peak at the π -jump of the RPAE scattering phase.

In Fig. 1.7(b) the whole time delay of the photoionization of the $3p$ subshell is depicted. The contributions of all magnetic substates are included according to Eq. (1.27). Substantial variation with the photon energy $\hbar\omega_{\text{XUV}}$ can be observed. Furthermore, in contrast to the results for neon, we find a pronounced angular modulation around 50 eV which is correlated with the Cooper minimum. The origin is the angular dependence of $\tau_{\text{W}}^{\ell_i=1, m_i=0}$ due to the existence of two ionization channels ($3p \rightarrow ks$ and $3p \rightarrow kd$). The time delays of the other magnetic substates $\tau_{\text{W}}^{\ell_i=1, m_i=\pm 1} \equiv \frac{\partial}{\partial \varepsilon_k} [\delta_{\ell=2}^{\text{HF}}(k) + \delta_{\ell=2}^{\text{RPAE}}(k)]$ do not show any angular modulation since only the transition $3p \rightarrow kd$ is possible.

At an angle of $\vartheta_{\mathbf{k}} = 0^\circ$ the probability of the photoionization processes corresponding to the initial states $\ell_i = 1, m_i = \pm 1$ are zero, i.e. in this case $\tau_{\text{W}}^{3p} = \tau_{\text{W}}^{\ell_i=1, m_i=0}$. The negative sign of τ_{W}^{3p} around the Cooper Minimum despite the positive energy derivative of the HF scattering phase $\delta_{\ell=2}^{\text{HF}}$ corresponding to the dominant transition $3p \rightarrow kd$ can be explained by the RPAE phase $\delta_{\ell=2}^{\text{RPAE}}$, which makes a sudden jump of $-\pi$. However, the peak of the corresponding time delay at the Cooper minimum is not as pronounced and sharp as in the case of the photoionization of the $3s$ subshell. The reason is the interference between both possible photoionization channels which on the other hand, leads to the substantial angular dependence. The usually weak transition $3p \rightarrow ks$ becomes stronger near the Cooper minimum, i.e. it is of the same magnitude as the otherwise dominant transition $3p \rightarrow kd$. As a consequence, the negative delay peak induced by the RPAE phase $\delta_{\ell=2}^{\text{RPAE}}$ is damped by the $3p \rightarrow ks$ transition where the corresponding RPAE phase $\delta_{\ell=0}^{\text{RPAE}}$ makes a positive jump of π (cf. Fig. 1.6(a)). Therefore, the resulting time delay does not fall below -100 as. Nevertheless, we can observe a local and pronounced negative time delay due to the intershell correlation correction.

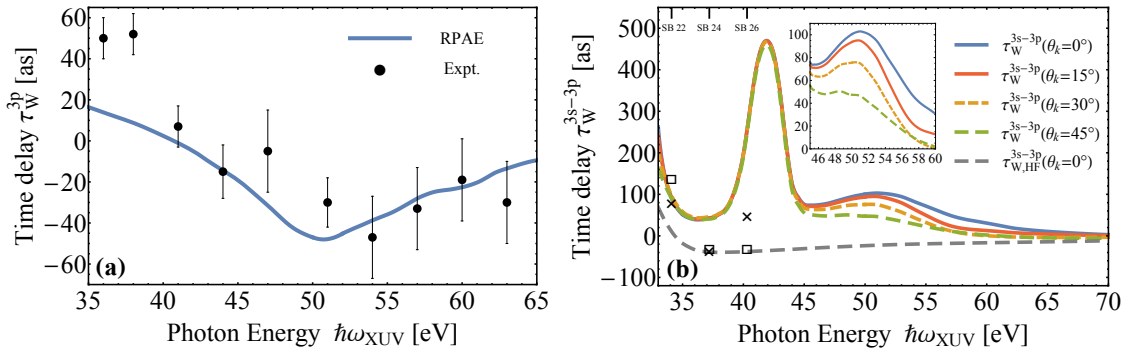


Fig. 1.8 (a) Comparison of the angle-integrated time delay τ_W^{3p} corresponding to the photoionization of the $3p$ subshell calculated within the RPAE with the experimental measurement [66]. (b) Full relative time delay τ_W^{3s-3p} in dependence on the photon energy and different asymptotic directions $\vartheta_{\mathbf{k}}$ of the photoelectron. For comparison, the experimental results by the RABBIT method are included (closed circles, Ref. [5]; open squares, Ref. [4]).

For angles $\vartheta_{\mathbf{k}} > 0^\circ$ and photon energies around the Cooper minimum, the transition $3p \rightarrow ks$ begins to dominate the photoionization process. Now, it marks the primary contribution to $\tau_W^{\ell_i=1, m_i=0}$ with the consequence that the resulting full time delay τ_W^{3p} (with contributions from all possible initial magnetic substates) tending to increase due to the positive π -jump of the RPAE phase $\delta_{\ell=0}^{\text{RPAE}}$. The reason is that the Legendre polynomial $P_2^0(\cos \vartheta_{\mathbf{k}})$ decreases for larger angles $\vartheta_{\mathbf{k}}$ while $P_0^0(\cos \vartheta_{\mathbf{k}})$ is constant (cf. Eq. (1.24)). For photon energies far away from the Cooper minimum, the effect due to angular dependence becomes very subtle. In this regime, the photoionization process is entirely dominated by the transition $3p \rightarrow kd$ [86] and the same characteristics as for neon can be observed. In addition, the RPAE phase $\delta_{\ell=2}^{\text{RPAE}}$ becomes very flat which means the angular dependence of the time delay is of the same magnitude as in the case of neon.

The small inset of Fig. 1.7(b) shows the time delay of the $3p$ photoionization process angle-resolved for three different photon energies. Again large differences between the atomic systems neon and argon can be observed due to the existence of the Cooper minimum in the second case. The time delay corresponding to photoionization of neon shows nearly no angular modulation in the range between -45° and 45° while in the case of argon, we find a substantial variation with the angle for photon energies around the Cooper minimum. Especially for the photon energy $\hbar\omega_{\text{XUV}} = 51$ eV, a strong dependence of τ_W^{3p} up to $\vartheta_{\mathbf{k}} = \pm 45^\circ$ can be observed.

Recently, the angular dependence of the time delay was addressed experimentally [66]. The comparison between the angle-integrated measurement of the $3p$ time delay τ_W^{3p} and the RPAE result in Fig. 1.8(a) reveals a reasonably well agreement. Therefore, the RPAE prediction regarding the angular dependence of the time delay seems to be qualitatively correct. However, a more accurate angle-resolved experimental measurement is needed

to verify the theoretically predicted angular modulation of the time delay for asymptotic directions of the photoelectron far away from the polarization axis.

In Fig. 1.8(b) the full relative time delay τ_{W}^{3s-3p} between the photoionization process of the $3s$ and $3p$ subshells are shown. By varying the photon energy $\hbar\omega_{\text{XUV}}$ the otherwise very flat course of the time delay is interrupted at the Cooper minima of the $3s$ and $3p$ subshells. The first peak at 42 eV originates from the very pronounced peak of the $3s$ time delay τ_{W}^{3s} . Characteristic for this feature is the quasi non-existent angular dependence. At larger photon energies around 50 eV, we find the second peak originating from the $3p$ contribution and a large dependence on the asymptotic direction $\vartheta_{\mathbf{k}}$ of the photoelectron. The results in the forward direction ($\vartheta_{\mathbf{k}} = 0^\circ$) are in good agreement with other RPAE results [16, 56] as well as other theoretical approaches like TDLDA [61] or MCHF [57]. The photon energies corresponding to sideband frequencies (SB) of the titanium:sapphire laser at 800 nm used in two-photon interferometric experiments [4, 5] are marked. The corresponding measurements confirm the trend of our theoretical results. However, the RPAE and the measured time delays agree not very well, except for the lowest experimental energy, i.e. furthest away from the $3s$ Cooper minimum. Since the theoretically calculated $3p$ time delay τ_{W}^{3p} is in good agreement with the experiments [66, 90] the correlation correction for the $3s$ subshell does not seem to be entirely accurate. Furthermore, no significant angular modulation occurs at these photon energies which could influence the experimental results. Consequently, a measurement of the time delay τ_{W}^{3s} corresponding to the photoionization of the $3s$ subshell could give a more detailed insight into this theory-experiment discrepancy.

In contrast to the investigation of neon, the strong angular dependence of the relative time delay around the $3p$ Cooper minimum of argon has a significant impact on the experimental measurement emphasizing the importance of the acceptance angle ϑ_{max} of the used TOF detector. At a photon energy $\hbar\omega_{\text{XUV}} = 51$ eV in the forward direction, τ_{W}^{3s-3p} amounts to 105 as, while an acceptance angle of 20° results in an angle-integrated relative time delay of 92 as. A larger acceptance angle $\vartheta_{\text{max}} = 45^\circ$ leads to a relative time delay, averaged over all possible asymptotic photoemission directions, of 68 as.

1.7 Conclusion

Using several theoretical methods, the angular dependence of the Wigner time delay for the two atomic systems neon and argon was calculated. The preliminary considerations show that the whole time delay measured in an attosecond streaking experiment can be divided into two parts: $\tau_{\text{S}} = \tau_{\text{at}} + \tau_{\text{CLC}}$. Here, the atomic time delay τ_{at} is equivalent to the Wigner time delay τ_{W} . While τ_{W} represents the individual scattering characteristics of the atomic system, the CLC delay is a universal quantity and can be calculated analytically according

to Eq. (1.13). Therefore, information about the angular dependence of the time delay is embedded in the Wigner time delay τ_W .

The study of the time delay endorses its angular dependence as general effect whenever transitions to two photoionization channels are accessible leading to interference, e.g. $\tau_W^{\ell_i=1, m_i=0}$ for neon or argon. That means in principle, the angular dependence of the time delay can be accessed with SAE calculations. In the case that only one photoionization channel exists, we find no angular modulation of the time delay.

Our calculations for neon for the relative time delay τ_W^{2p-2s} confirm this and show a weak angular dependence for high photon energies. Therefore, we obtained a negative answer regarding the question whether the angular modulation of the time delay has a significant impact on the measurement by Schultze *et al.* [3] and helps to resolve the discrepancy between theory and experiment.

In the case of argon, the observation is different. The SAE methods are not capable of describing the electronic structure and the photoionization process accurately since the Cooper minimum can not be reproduced correctly. Within the RPAE, which adds intershell correlation correction, the minima in the photoionization amplitudes for both subshells $3s$ and $3p$ can be evaluated more precisely, and we find a substantial angular modulation of the time delay τ_W^{3p} corresponding to the photoionization of the $3p$ subshell in this regime. The explanation is given by the strengths of the usually weak and dominating photoionization channels, i.e. $3p \rightarrow ks$ and $3p \rightarrow kd$, which are of the same magnitude around the Cooper minimum. Our theoretical results are in accord with other theoretical models and show a reasonable agreement with the experimental measurements, although discrepancies persist. Indirectly, the pronounced angular dependence of the time delay is confirmed by the angle-integrated measurement [66].

The angular dependence in the regime of the $3p$ Cooper minimum would have a significant impact on the measurements and emphasize the importance of the acceptance angle ϑ_{\max} of the TOF detector used in the corresponding experiment.

Chapter 2

Ultrafast processes with light carrying orbital angular momentum

2.1 Introduction

Light carrying orbital angular momentum (OAM) [18–23, 91], also called optical vortex, has found exciting applications in photonics and electronics but also gave new impulses in chemistry, life sciences, quantum information, astronomy or optical telecommunication [24–36]. Other examples involve the trapping, rotating and manipulating of microscopic objects [92–94], atoms and molecules [95–97] as well as Bose-Einstein condensates [98]. As an exciting utilization, an OAM beam may drive currents in quantum rings [99, 100] and semiconductor stripes [101].

The phase front of such an OAM beam has the shape of a helix. In cylindrical coordinates with the z -axis parallel to the propagation direction of the light beam this helical shape as part of the field spatial distribution is characterized by $\exp(i\ell_{\text{OAM}}\varphi)$ where φ is the azimuthal angle in the xy -plane and ℓ_{OAM} is the topological charge of the optical vortex. It was shown by Allen *et al.* [18] that helically shaped beams carry OAM with respect to the z -axis. They are, for instance, mathematically described by Laguerre-Gaussian (LG) modes which are solutions of the paraxial approximation of the Helmholtz equation. Each photon of such an LG beam carries a quantized amount of OAM of $\ell_{\text{OAM}}\hbar$. Here we introduce the topological charge ℓ_{OAM} , also called winding number, as an integer number which characterizes the amount of twists of the phase in one wavelength. The higher ℓ_{OAM} , the faster the light is spinning around the propagation axis. Characteristic for the class of optical vortices is the phase singularity in the center which means that the intensity of the beam vanishes at the optical axis and rises to larger radii. Thus, in case of LG modes the spatial profile has the shape of a donut whose radius is determined by the beam's waist and the topological charge ℓ_{OAM} .

Several methods and techniques exist to produce OAM beams. A big advantage is that they can be created from usual light sources [18, 102, 103]. The different approaches involve computer-generated holograms screened on a spatial light modulator (SLM) [104–106], the generation with the aid of astigmatic mode converters [19] or spiral phase plates [107] as well as the conversion of spin angular momentum to OAM in inhomogeneous anisotropic plates [108]. However, there exists no perfect method since all have several limitations. For instance, the creation of OAM beams with the help of an SLM is not very efficient while the overall quality is limited by the pixel size of the nematic liquid crystal cells. The other methods, although more efficient, are static approaches and cannot be dynamically controlled. Recently, a very new method to generate and manipulate OAM beams rests on a ring resonator based geometry [109]. Fascinating for future research is the possibility to generate optical vortices with radii independent on the topological charge with a method which bases on the width pulse approximation of Bessel functions [110, 111].

A key element of using this type of light beams is the opportunity to transfer effectively orbital angular momentum when interacting with matter [94, 112–116]. Therefore, a torque is exerted on the charge carriers which points to exciting new ways of the optically induced controlling and steering of the orbital motion of charged particles. As a demonstration the numerical simulations in Ref. [101] reveal that an electron wave packet in a semiconductor bar which is irradiated with an OAM light spot attains such a torque. As a consequence, it begins to drift transversely to the propagation direction. Furthermore, the direction and magnitude of this drift can be controlled effectively by the parameters of the optical vortex which emphasizes the enormous flexibility by using this type of light.

Within this thesis, we want to show three fundamentally different applications of the optical vortices and the capability of OAM light to reveal exciting and new effects.

i) OAM beams open the way to initiate unprecedented optical excitations to different magnetic sublevels. To demonstrate this effect, the *atomic time delay* which was already introduced in the first chapter of this thesis will be revisited using optical vortex beams. For a linearly polarized light the photoionization probabilities of the initial states with $m_i = \pm m$ are equal and so are their contributions to the time delay. They also show the same angular dependence (cf. with chapter 1 of this thesis). Let us consider the photoionization process of an argon atom with an XUV, OAM carrying LG beam [117–120] which are experimentally feasible [121, 122]. Note that high-intensity LG beams are also available [123].

We show that employing an optical vortex for photoionization initiates transitions involving the change of the magnetic quantum number by an amount set by the topological charge ℓ_{OAM} . Thus, the symmetry between the magnetic sublevels will be broken. As a consequence, we find certain asymptotic directions of the photoelectron where the photoionization process and the corresponding time delay are totally dominated by a magnetic sublevel. Furthermore, the calculation shows that the time delay also depends strongly on the position of the atom in the beam spot. This is connected to the strong dependence of the

photoionization probabilities on the atomic-scale distance of the atom from the optical axis of the twisted photon beam which is already theoretically predicted [124, 125]. The reason is the characteristic of the phase structure which changes drastically on the atomic scale [126, 127]. Therefore, it is possible to use the time delay measurements as a tool to identify the origin of the photoelectron in energy, magnetic sublevel, and space.

ii) Endohedral molecular magnets are auspicious candidates for molecular electronics and quantum information processing. Possible realizations with interesting applications are fullerenes containing nitrogen [128, 129] or DySc₂N [130]. The reason is that the carbon cage acts as a shield for the magnetic properties of the nanoparticles inside. Thus, they exhibit relatively long spin relaxation times. However, for a proper functionalization, an ultrafast control of the local magnetization is favorable. From fundamental electrodynamics, it is known that a charge current loop generates an equally localized magnetic field which is capable of steering the properties of magnetic nanoparticles.

We will consider irradiating a C₆₀ molecule with a fs OAM beam [131]. The abovementioned capability to transfer of OAM to the particle initiates transitions from the bound degenerative states to the so-called super atomic molecular orbitals (SAMOs) which were revealed experimentally [132] and theoretically [133–140]. They are in principle diffuse, unoccupied but still bound (by the central molecular cage potential) orbitals with well-defined orbital angular momenta. Hence, the SAMOs extend way beyond the occupied π orbitals (second radial band) and an influence due to modification of the geometry or doping is not pronounced. Therefore *ab-initio* calculations show that they also exist in the case of larger or doped fullerenes like N@C₆₀.

We will demonstrate that for the transition from a bound state of the π -band to the SAMO due to the interaction with the optical vortex pulse the magnetic quantum number m also changes. The change Δm is set by the topological charge ℓ_{OAM} . Therefore, a charge current loop on the surface of the carbon cage, as well as a magnetic orbital moment, is generated for moderate intensities. The advantage is that by using an OAM beam one is not restricted to the conventional optical selection rules, and the current can be effectively increased by increasing the topological charge ℓ_{OAM} . We evaluate then the magnetic field inside the fullerene cage which can be tuned in sign and amplitude by varying the parameters of the optical vortex, such as the topological charge, the waist, the intensity or the frequency.

iii) As a third application, we explore the effect of an optical vortex beam which is focused on a GaAs-AlGaAs-based quantum ring. Due to the interaction with the light wave and the corresponding transfer of OAM conduction band transitions are caused which leads to a centrifugal drift of the charge carriers. Thus, a time-dependent imbalance between the inner and outer ring boundaries is shown, i.e. a charge separation can be found. This process leads to a useable voltage and a directed photocurrent whose magnitude can be controlled by the parameters of OAM beam. Most important it can be increased by enlarging the light topological charge ℓ_{OAM} at a fixed frequency and intensity, i.e. without additional heating.

In a further step, a mechanism to generate currents induced by light carrying OAM is demonstrated. A full-fledged numerical simulation emphasizes that this photovoltaic effect, i.e. generation of a charge current from light sources, is systematically controllable and tuneable by changing the properties of light as well as by appropriate nanostructuring of the system. Therefore, the quantum ring acts as a charge reservoir for the generated current [141, 142]. We propose a wiring network of several quantum rings with spiral phase plates on top. The mechanism is clear: a conventional (Gaussian) light beam traversing the phase plates would be transformed in an optical vortex, which transfers OAM to the charge carriers due to subsequent light-matter interaction. With every additional quantum ring in this network of charge wheels, the resulting current in an attached wire will be increased. The theoretical findings gain further importance in the view of recent experiments on an n-doped bulk GaAs, which is irradiated with OAM pulses [143]. It was measured that the semiconductor sample indeed acquires OAM due to the interaction with the optical vortex. Unless otherwise stated, atomic units (a.u.) will be used throughout this chapter.

2.2 Mathematical description of OAM beams

The vector potential of a vortex beam, used in the investigations below, in cylindrical coordinates with the z -axis parallel to the light propagation is given by [18]

$$\mathbf{A}(\mathbf{r}, t) = \hat{\mathbf{e}} A_0 f_{\ell_{\text{OAM}}}^p(\mathbf{r}) e^{i(\ell_{\text{OAM}} \varphi'(\mathbf{r}) - \omega t)} \Omega(t) e^{iq_z z} + \text{c.c.} \quad (2.1)$$

Here $\hat{\mathbf{e}}$ is the polarization vector and $\Omega(t)$ the pulse temporal envelope which can be further characterized while the amplitude of vector potential is given by A_0 . The angle $\varphi'(\mathbf{r})$ is the angle in the xy -plane of the considered object relative to the optical axis of the light beam. In all our studies the dynamics transversal to q_z is of interest. For photon energies $\hbar\omega$ in the (X)UV regime and the size of the considered objects (argon and the C_{60} molecule) we deduce that $q_z z \ll 1$, i.e. the dipole approximation is very acceptable along the z -axis. The radial structure is described by the functions

$$f_{\ell_{\text{OAM}}}^p(\boldsymbol{\rho}'(\mathbf{r})) = C_{\ell_{\text{OAM}}, p} e^{-\frac{\rho'^2(\mathbf{r})}{w_0^2}} \left(\frac{\sqrt{2}\rho'(\mathbf{r})}{w_0} \right)^{|\ell_{\text{OAM}}|} L_p^{|\ell_{\text{OAM}}|} \left(\frac{2\rho'^2(\mathbf{r})}{w_0^2} \right), \quad (2.2)$$

where $\boldsymbol{\rho}'(\mathbf{r})$ describes the vector in the xy -plane and relative to the optical axis of the beam. The parameter p indexes the number of radial nodes of the spatial distribution of the light field. The functions $L_p^{|\ell_{\text{OAM}}|}(x)$ are the associated Laguerre polynomials while $C_{\ell_{\text{OAM}}, p}$ describes the normalization factor. In all investigations we assume $p = 0$, i.e. $L_{p=1}^{|\ell_{\text{OAM}}|} = 1$. The case $p \neq 0$ implicates no further complications but adds no further qualitative information. Highest intensities are reached at $\rho_{\text{max}} = \sqrt{\frac{\ell_{\text{OAM}}}{2}} w_0$ with the maximal amplitude

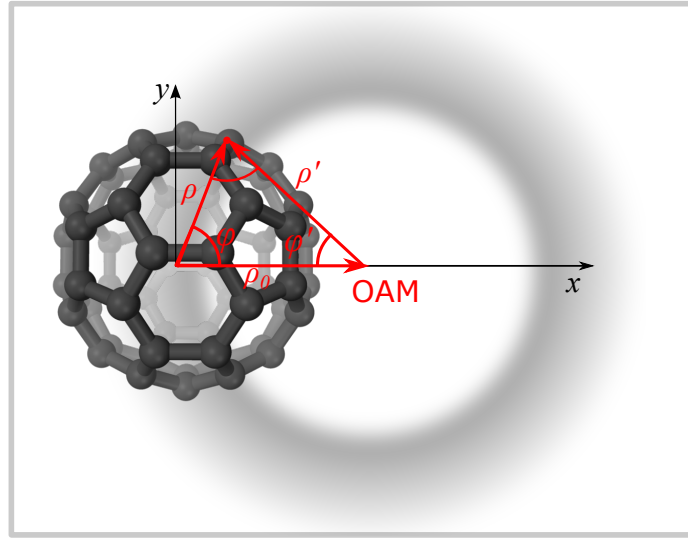


Fig. 2.1 A general schematic representation of the coordinate system corresponding to the investigations below. The considered object (in this particular case the C_{60} molecule) in the xy -plane has the distance ρ_0 to the optical axis of the vortex beam. The vector $\rho = r \sin(\vartheta)$ marks the position of the electron relative to the center of mass of the object, while ρ' is relative to the optical axis. The shaded area indicates the donut-shaped high-intensity regime of the optical vortex.

$A_{\max}^{\ell_{\text{OAM}}} = |\ell_{\text{OAM}}| \frac{|\ell_{\text{OAM}}|}{2} e^{\frac{|\ell_{\text{OAM}}|}{2}}$. Thus, for a reasonable comparison for different values of the topological charge ℓ_{OAM} the normalization factor is given by $C_{\ell_{\text{OAM}},p} = 1/A_{\max}^{\ell_{\text{OAM}}}$.

In Fig. 2.1 a schematic representation of the coordinate system is presented. In the general case the optical axis and the center of mass of the considered object (origin of ordinates) do not coincide and therefore, $\rho'(\mathbf{r})$ or $\varphi'(\mathbf{r})$ (relative to the optical axis) are functions of \mathbf{r} . For a fixed distance ρ_0 between the object and the vortex beam the angle $\varphi'(\mathbf{r})$ is related to φ according to:

$$\frac{\sin(\varphi'(\mathbf{r}))}{\sin(\varphi)} = \frac{\rho}{\rho'(\mathbf{r})} \quad (2.3)$$

while

$$\rho'(\mathbf{r}) = \sqrt{\rho^2 + \rho_0^2 - 2\rho\rho_0 \cos(\varphi)}. \quad (2.4)$$

Note that $\rho = r \sin(\vartheta)$ where the angle ϑ is relative to propagation direction (and optical axis) of the vortex beam. In the special case where the optical axis and the center of mass coincide, i.e. $\rho_0 = 0$, the relation applies that $\rho' \equiv \rho$ and $\varphi' \equiv \varphi$. Otherwise, we have to calculate $\rho'(\mathbf{r})$ or $\varphi'(\mathbf{r})$ (which are relative to the optical axis) according to the Eq. (2.3) and (2.4).

The total amount of transferable angular momentum of the light beam defined in Eq. (2.1) is then given by $(\ell_{\text{OAM}} + \sigma_z)\hbar$ where σ_z is the helicity which is connected to the polarization vector $\hat{\mathbf{e}}$. In the case of linearly polarized light $\sigma_z = 0$ while for circularly polarized light $\sigma_z = \pm 1$.

2.3 Time delay in atomic photoionization with optical vortex beams

2.3.1 Photoionization amplitude

We consider here the photoionization process of the argon atom with a circularly polarized XUV OAM beam. For extracting the information about the angular dependence and the time delay we follow the steps introduced in the first chapter of this thesis. In the gauge where the scalar potential disappears the interaction Hamiltonian with the optical vortex beam is given by

$$\hat{H}_{\text{int}} = -\frac{1}{2} [\hat{\mathbf{p}} \cdot \mathbf{A}(\mathbf{r}, t) + \mathbf{A}(\mathbf{r}, t) \cdot \hat{\mathbf{p}}]. \quad (2.5)$$

The momentum operator is represented by $\hat{\mathbf{p}}$. Since we consider very moderate intensities we neglect the A^2 term of the vector potential $\mathbf{A}(\mathbf{r}, t)$.

The atomic potential of the argon atom is incorporated into the field free Hamiltonian \hat{H}_0 and is given by the single-particle potential from Muller [144]. Originally, it was designed for strong-field physics with low-frequency laser fields. Later, the potential was used for analyzing XUV attosecond pulses within a RABBIT scheme [145]. As a single-particle potential, the weak point is the relatively poor agreement with the experimental data close to the ionization threshold of the one-photon XUV photoionization process which can be explained by the absence of correlation effects [146]. Nevertheless, significant for our investigation is the reasonable sound reproduction of the energetic position of the $3p$ Cooper minimum in comparison to the experimental measurement and the existing RPAE calculations [17].

The temporal envelope of the XUV OAM pulse is characterized by $\Omega(t) = \cos[\pi t/nT]^2$ where $T = 2\pi/\omega$ is the cycle duration, and n characterizes the number of optical cycles. The beam waist in the calculations below is chosen as $w_0 = 100$ nm (940 a.u.) and is much larger than the atomic scale. Obviously, due to the donut-shaped intensity distribution, the object in the middle experiences only a very weak electric field which justifies the perturbative treatment even for high intense fields. In an experimental realization, the atoms would be in a gas phase and therefore distributed over the whole beam profile. However, the photoionization probabilities depend strongly on the position of the atom relative to the optical axis [124, 125]. We demonstrate below that it is sufficient to place the atom 10 a.u. away from the center of the optical vortex with the consequence that the captured time delays (and photoionization amplitudes) already show no dependence of the topological charge. This relation can be explained since the transferable OAM refers to the optical axis and decreases rapidly even on the atomic scale. As a consequence, these two types of atoms (in the center of the beam and far away from the optical axis) are distinguishable by measurements of the time delay or photoelectron momentum distribution. In the calculations

below the considered electric field starts with a zero amplitude at the optical axis of the vortex reaching a peak amplitude of 1 a.u. at a distance of 10 a.u., which amounts to an intensity at ρ_{\max} of 5.6×10^{19} W/cm² in the case of $\ell_{\text{OAM}} = 1$.

In addition to the full numerical treatment with the MIM technique, introduced in the first chapter, an analytical model of the photoionization process with optical vortex beams is favorable to understand the influence of the transferred OAM. Therefore, we consider the special case of circularly polarized light characterized by $\hat{\boldsymbol{\varepsilon}} = (1, i)^T$ and a strict positive topological charge ℓ_{OAM} . The argon atom is positioned at the center of the vortex beam, and consequently, the vector \mathbf{r} refers to the optical axis, i.e. $\rho'(\mathbf{r}) = \rho$ and $\varphi'(\mathbf{r}) = \varphi$. For a short attosecond XUV pulse the captured distance of the photoelectron is much smaller than the waist w_0 of the beam, i.e. $\exp^{-\rho^2/w_0^2} = 1$. Thus, the angular and radial parts in Eq. (2.1) can be decoupled and the whole photoionization can be described analytically. Furthermore, under these assumptions one can show that in this particular case $\nabla \cdot \mathbf{A}(\mathbf{r}, t) = 0$. Therefore, using then the identity $\hat{\mathbf{p}} = [\hat{H}_0, \mathbf{r}]_-$ the transition matrix elements can be computed according to

$$\langle \varphi_{\mathbf{k}}^f | \hat{H}_{\text{int}}(t) | \Psi_i \rangle = i(\varepsilon_i - \varepsilon_k) \langle \varphi_{\mathbf{k}}^f | \mathbf{r} \cdot \mathbf{A}(\mathbf{r}, t) | \Psi_i \rangle. \quad (2.6)$$

They describe the transition from the initial bound electron state $|\Psi_i\rangle$ into the continuum which is represented by $|\langle \varphi_{\mathbf{k}}^f \rangle$ due to the action of the OAM XUV beam. Now by inserting the matrix element into Eq. (1.15) we obtain access to the information about the angular characteristics and the time delay. The calculation of the projection coefficients within the single active electron approximation leads to the following analytic expression:

$$a_i(\mathbf{k}) = (\varepsilon_i - \varepsilon_k) \sum_{\ell=0}^{m=\ell} \sum_{m=-\ell}^{m=\ell} i^{-\ell} e^{i\delta_\ell(k)} d_{\ell, n_i \ell_i}^{\ell_{\text{OAM}}} Y_{\ell m}(\boldsymbol{\Omega}_{\mathbf{k}}) \times \left[\mathcal{E}_-(\varepsilon_k - \varepsilon_i) \begin{pmatrix} \ell & \ell_{\text{OAM}} + 1 & \ell_i \\ -m & \ell_{\text{OAM}} + 1 & m_i \end{pmatrix} + \mathcal{E}_+(\varepsilon_k - \varepsilon_i) \begin{pmatrix} \ell & \ell_{\text{OAM}} + 1 & \ell_i \\ -m & -\ell_{\text{OAM}} - 1 & m_i \end{pmatrix} \right], \quad (2.7)$$

where $\mathcal{E}_{\mp}(\varepsilon) = \mathcal{E}_0 \int_{-\infty}^{\infty} dt \Omega(t) e^{i(\varepsilon \mp \omega)t}$ describe the absorption and emission coefficients. The amplitude is characterized by $\mathcal{E}_0 = A_0 C_{\ell_{\text{OAM}}, p=0}$. The reduced matrix elements are in accordance with Eq. (1.22) and are given by

$$d_{\ell, n_i \ell_i}^{\ell_{\text{OAM}}} = \sqrt{\frac{(2\ell + 1)(2\ell_{\text{OAM}} + 3)(2\ell_i + 1)}{3}} \times \begin{pmatrix} \ell & \ell_{\text{OAM}} + 1 & \ell_i \\ 0 & 0 & 0 \end{pmatrix} \int dr r^{3+\ell_{\text{OAM}}} R_{k\ell}(r) R_i(r). \quad (2.8)$$

The projection coefficients in (2.7) are in general angular dependent while the corresponding photoionization probability $w_i(\varepsilon_k, \boldsymbol{\Omega}_{\mathbf{k}}) = |a_i(\mathbf{k})|^2$ of the photoionization process of the

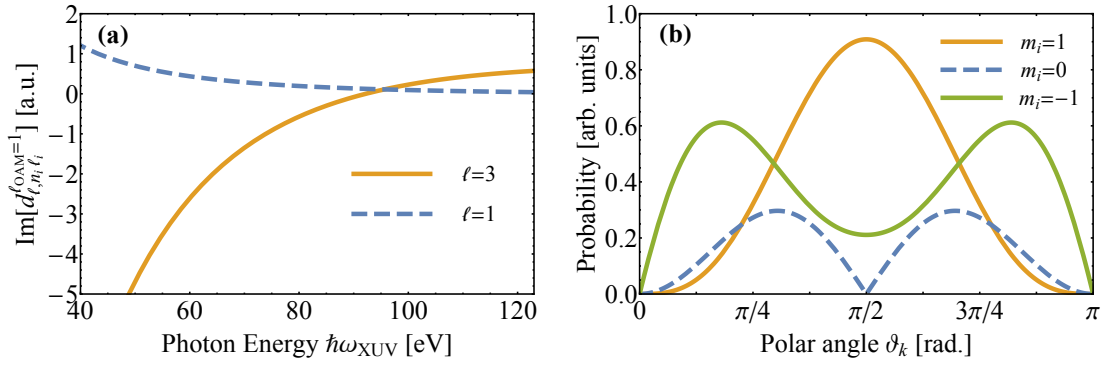


Fig. 2.2 (a) Reduced radial matrix elements for the partial wave functions with the orbital angular momenta $\ell = 1$ and $\ell = 3$. (b) Photoionization probabilities for the three different initial states of the $3p$ subshell in argon.

initial state indexed by i is peaked around the center of energy (COE) $\varepsilon_{\text{COE}} = \omega + \varepsilon_i$ [with $k_{\text{COE}} = \sqrt{2\varepsilon_{\text{COE}}}$]. For adiabatic pulses, we find that the emission coefficient $\mathcal{E}_+(\varepsilon_{\text{COE}}) \equiv 0$. For photoionization from the various possible initial states of the $3p$ subshell, we obtain then the analytical expressions:

$$a(k_{\text{COE}}, \Omega_{\mathbf{k}}) = \begin{cases} S_{\ell_{\text{OAM}}+2, \ell_{\text{OAM}}} Y_{\ell_{\text{OAM}}+2, \ell_{\text{OAM}}}(\Omega_{\mathbf{k}}) & m_i = -1 \\ + S_{\ell_{\text{OAM}}+2, \ell_{\text{OAM}}} Y_{\ell_{\text{OAM}}, \ell_{\text{OAM}}}(\Omega_{\mathbf{k}}) & \\ S_{\ell_{\text{OAM}}+2, \ell_{\text{OAM}}+1} Y_{\ell_{\text{OAM}}+2, \ell_{\text{OAM}}+1}(\Omega_{\mathbf{k}}) & m_i = 0 \\ S_{\ell_{\text{OAM}}+2, \ell_{\text{OAM}}+2} Y_{\ell_{\text{OAM}}+2, \ell_{\text{OAM}}+2}(\Omega_{\mathbf{k}}) & m_i = 1 \end{cases}, \quad (2.9)$$

where

$$S_{\ell, m} = \mathcal{E}_-(\varepsilon_{\text{COE}}) d_{\ell, m; \ell_i}^{\ell_{\text{OAM}}} i^{-\ell} e^{i\delta_\ell(k_{\text{COE}})} \begin{pmatrix} \ell & \ell_{\text{OAM}}+1 & 1 \\ -m & \ell_{\text{OAM}}+1 & m_i \end{pmatrix}. \quad (2.10)$$

The equation applies for a photoelectron originating from a magnetic sublevel with m_i and a considered topological charge ℓ_{OAM} . The information on the dependence on the emission angle $\Omega_{\mathbf{k}} = (\vartheta_{\mathbf{k}}, \varphi_{\mathbf{k}})$ of the photoelectron emission is encapsulated in the spherical harmonics. The OAM light leads to new selection rules which are dependent on the considered topological charge ℓ_{OAM} . We find that $\Delta\ell \leq \ell_{\text{OAM}} + 1$ ($\ell_i + \ell + \ell_{\text{OAM}}$ odd) and $\Delta m = \ell_{\text{OAM}} + 1$. It is immediately obvious that no photoelectrons originating from $m_i = 0$ are emitted in the xy plane (i.e. $\vartheta_{\mathbf{k}} = \pi/2$) since the spherical harmonics $Y_{\lambda, \lambda-1}(\Omega_{\mathbf{k}})$ have a node at $\vartheta_{\mathbf{k}} = \pi/2$. Furthermore, The emission probability $|a_i(\mathbf{k})|^2$ exhibits no dependence on the angle $\varphi_{\mathbf{k}}$ since for a particular m_i the involved spherical harmonics have the same phase $\exp(i(\ell_{\text{OAM}} + 1 + m_i)\varphi_{\mathbf{k}})$ which cancels out by taking the absolute square.

From the considerations in the first chapter of this thesis, we learnt that the usually dominant transition to a higher orbital angular momentum is of the same magnitude as the generally weak transition to a lower orbital momentum around the Cooper minimum. However, the

energetic position of the minimum in the photoionization probability depends strongly on the angular momentum of the perturbative field. Fig. 2.2(a) shows the two relevant radial matrix elements (Eq. (2.8)), which correspond according to the scheme (2.9) to the transitions $\ell_i = 1 \rightarrow \ell = 3$ and $\ell_i = 1 \rightarrow \ell = 1$, in the case of $\ell_{\text{OAM}} = 1$. The figure reveals that around a laser frequency corresponding to $\hbar\omega = 95$ eV we find that $d_{\ell=3, \ell_i=1}^{\ell_{\text{OAM}}} = 1$ is of a comparable magnitude as $d_{\ell=1, \ell_i=1}^{\ell_{\text{OAM}}} = 1$. Thus, the photoionization minimum is shifted in comparison to the case of using an unstructured laser beam where we found the $3p$ Cooper minimum at 51 eV. Consequently, the influence of the topological charge is emphasized. The regime of the photon energies around $\hbar\omega = 95$ eV is the starting point of our investigation because from our insights, gathered in the first chapter of this thesis, we expect there the most pronounced angular dependence of the time delays and photoionization amplitudes. In Fig. 2.2(b) the photoionization probabilities $w(\vartheta_{\mathbf{k}})$ in dependence on the photoelectron emission angle $\vartheta_{\mathbf{k}}$ for the different initial states m_i are shown in the case of $\hbar\omega = 100$ eV. For the considered topological charge $\ell_{\text{OAM}} = 1$ the photoelectron originating the $m_i = 1$ initial state, upon absorbing a photon from the XUV-OAM field, ends up in the f -partial wave channel with $m = 3$. In contrast, the counter-rotating photoelectron is characterized by the superposition state of the p - and f -partial wave channels with a magnetic quantum number $m = 1$. The photoelectron ionized from the initial $3p$ state with $m_i = 0$ is described by the f -partial wave channel with $m = 2$. Consequently, the node of the spherical harmonic $Y_{3,2}(\Omega_{\mathbf{k}})$ at $\vartheta_{\mathbf{k}} = \pi/2$ (xy -plane) leads to the vanishing emission probability in this direction, i.e. the electron with a zero magnetic quantum number does not escape in this direction. Here the co-rotating photoelectron with $m_i = 1$ relative to the circularly polarized OAM-field is dominant over the counter-rotating one with $m_i = -1$. Interestingly, this situation is completely different in other directions. At $\vartheta_{\mathbf{k}} = 150^\circ$ the counter-rotating electrons has the largest photoionization probability. Consequently, the two types of electrons are predominantly emitted in different directions allowing thus a discrimination via angular resolved photoelectron detection. This is a big contrast to the usage of conventional and unstructured linearly polarized light beams where we find a symmetry between the photoelectrons originating from initial states with $m_i = \pm m$ meaning, in that case, they have the same angular dependence and photoionization probability.

In Fig. 2.3 the photoelectron momentum distributions corresponding to the asymptotic directions, where either the co-rotating ($\vartheta_{\mathbf{k}} = 90^\circ$) or the counter-rotating ($\vartheta_{\mathbf{k}} = 150^\circ$) photoelectrons dominates the photoionization process, are shown. They reveal the typical ring structure with the maximum at the radius $k_{\text{COE}} = \sqrt{2\varepsilon_{\text{COE}}}$ in the case of photoionization with circularly polarized light [80]. The width of the ring is influenced by the duration of the pulse, i.e. by the number of optical cycles n . A longer pulse is accompanied by a sharper structure in momentum space and therefore, the ring will become narrower. Furthermore, the structure of the photoelectron momentum distribution demonstrates the independence of the

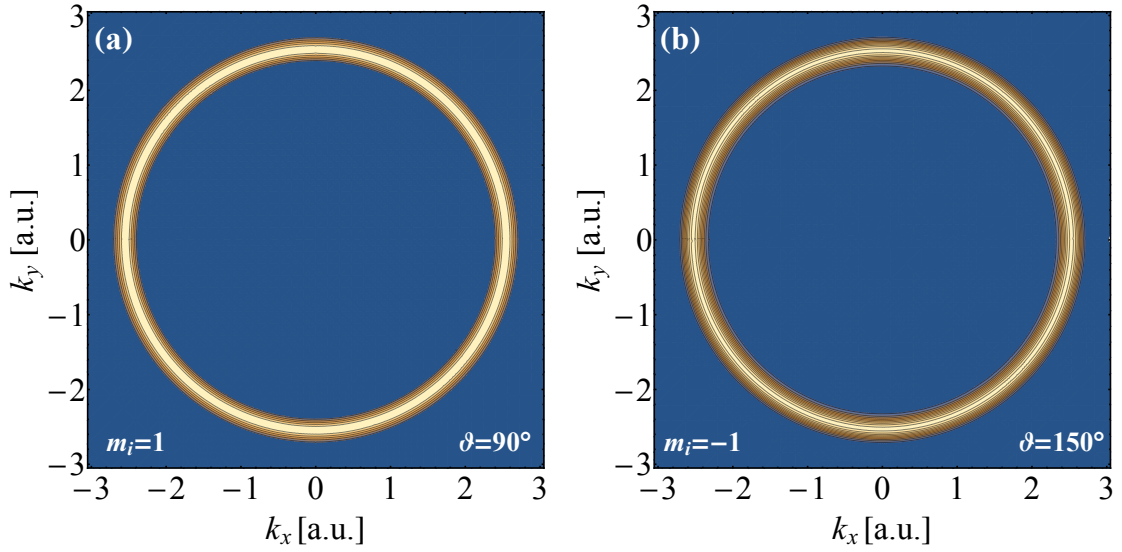


Fig. 2.3 The photoelectron momentum distributions corresponding to (a) $m_i = 1$ at $\vartheta_{\mathbf{k}} = 90^\circ$ and (b) $m_i = -1$ at $\vartheta_{\mathbf{k}} = 150^\circ$. The number of optical cycles $n = 10$. The other pulse parameters are given in the text.

photoionization probabilities of the angle $\varphi_{\mathbf{k}}$ for both photoelectrons. These characteristics are confirmed by the full-numerical simulation which yielded the same results.

2.3.2 Evaluation of the time delay

By following the steps of the first chapter, the Wigner time delay in photoionization is defined as the energy derivative of the spectral phase of the photoionization amplitude, i.e.

$$\tau_{\text{W}}^i(\varepsilon_{\mathbf{k}}, \Omega_{\mathbf{k}}) = \frac{\partial}{\partial \varepsilon_{\mathbf{k}}} \mu_i(\varepsilon_{\mathbf{k}}, \Omega_{\mathbf{k}}), \quad (2.11)$$

where $\mu_i(\varepsilon_{\mathbf{k}}, \Omega_{\mathbf{k}}) = \arg[a_i(\mathbf{k})]$. An alternative and more practical expression for the evaluation of the time delay is provided by [16]:

$$\tau_{\text{W}}^i(\varepsilon_{\mathbf{k}}, \Omega_{\mathbf{k}}) = \Im \left[\frac{1}{a_i(\mathbf{k})} \frac{\partial a_i(\mathbf{k})}{\partial \varepsilon_{\mathbf{k}}} \right]. \quad (2.12)$$

Taking into account that $\partial \mathcal{E}_- / \partial \varepsilon_{\mathbf{k}} = 0$ (absorption coefficient) while $\partial \mathcal{E}_+ / \partial \varepsilon_{\mathbf{k}} \neq 0$ (emission coefficient) at $\varepsilon_{\mathbf{k}} = \varepsilon_{\text{COE}}$, we find the following expression for the energy derivative of the

amplitude in case of $m_i = 1$

$$\begin{aligned} \left. \frac{\partial a(k, \Omega_{\mathbf{k}})}{\partial \varepsilon_k} \right|_{\varepsilon_k = \varepsilon_{\text{COE}}} &= \frac{\partial S_{\ell_{\text{OAM}}+2, \ell_{\text{OAM}}+2}}{\partial \varepsilon_k} Y_{\ell_{\text{OAM}}+2, \ell_{\text{OAM}}+2}(\Omega_{\mathbf{k}}) \\ &+ F_{\ell_{\text{OAM}}, -\ell_{\text{OAM}}} Y_{\ell_{\text{OAM}}, -\ell_{\text{OAM}}}(\Omega_{\mathbf{k}}) \\ &+ F_{\ell_{\text{OAM}}+2, -\ell_{\text{OAM}}} Y_{\ell_{\text{OAM}}+2, -\ell_{\text{OAM}}}(\Omega_{\mathbf{k}}) \end{aligned} \quad (2.13)$$

where the contribution of the absorption process changes the magnetic quantum number by $\Delta m = \ell_{\text{OAM}} + 1$. The part which incorporates the energy derivative of the emission coefficient and changes the magnetic quantum number by $\Delta m = -\ell_{\text{OAM}} - 1$ is described by the functions

$$F_{\ell, m} = \frac{\partial \mathcal{E}_+}{\partial \varepsilon_k} d_{\ell, n_i; \ell_i}^{\ell_{\text{OAM}}} i^{-\ell}(k) e^{i\delta_\ell(k)} \left(\begin{array}{ccc} \ell & \ell_{\text{OAM}} + 1 & 1 \\ -m & -\ell_{\text{OAM}} - 1 & m_i \end{array} \right) \Big|_{\varepsilon_k = \varepsilon_{\text{COE}}}. \quad (2.14)$$

In the same manner we obtain for $m_i = 0$

$$\begin{aligned} \left. \frac{\partial a(k, \Omega_{\mathbf{k}})}{\partial \varepsilon_k} \right|_{\varepsilon_k = \varepsilon_{\text{COE}}} &= \frac{\partial S_{\ell_{\text{OAM}}+2, \ell_{\text{OAM}}+1}}{\partial \varepsilon_k} Y_{\ell_{\text{OAM}}+2, \ell_{\text{OAM}}+1}(\Omega_{\mathbf{k}}) \\ &+ F_{\ell_{\text{OAM}}+2, -\ell_{\text{OAM}}-1} Y_{\ell_{\text{OAM}}+2, -\ell_{\text{OAM}}-1}(\Omega_{\mathbf{k}}) \end{aligned} \quad (2.15)$$

and for $m_i = -1$

$$\begin{aligned} \left. \frac{\partial a(k, \Omega_{\mathbf{k}})}{\partial \varepsilon_k} \right|_{\varepsilon_k = \varepsilon_{\text{COE}}} &= \frac{\partial S_{\ell_{\text{OAM}}+2, \ell_{\text{OAM}}}}{\partial \varepsilon_k} Y_{\ell_{\text{OAM}}+2, \ell_{\text{OAM}}}(\Omega_{\mathbf{k}}) \\ &+ \frac{\partial S_{\ell_{\text{OAM}}, \ell_{\text{OAM}}}}{\partial \varepsilon_k} Y_{\ell_{\text{OAM}}, \ell_{\text{OAM}}}(\Omega_{\mathbf{k}}) \\ &+ F_{\ell_{\text{OAM}}+2, -\ell_{\text{OAM}}-2} Y_{\ell_{\text{OAM}}+2, -\ell_{\text{OAM}}-2}(\Omega_{\mathbf{k}}). \end{aligned} \quad (2.16)$$

Due to the terms which are proportional to $\partial \mathcal{E}_+ / \partial \varepsilon_k|_{\varepsilon_k = \varepsilon_{\text{COE}}}$ a dependence on the azimuthal angle $\varphi_{\mathbf{k}}$ to the time delay is induced. Evaluating (2.12) on the energy shell $\varepsilon_k = \varepsilon_{\text{COE}}$ reveals that this angular modulation depends on $\exp[i(2\ell_{\text{OAM}} + 2)\varphi]$ and reflects the influence of the topological charge. The energy derivative $\partial \mathcal{E}_+ / \partial \varepsilon_k|_{\varepsilon_k = \varepsilon_{\text{COE}}}$ is very sensitive to the pulse length and decreases very fast with an increasing number n of optical cycles. Therefore, we expect that the variation on $\varphi_{\mathbf{k}}$ also declines rapidly with a longer pulse duration.

The time delay associated with the photoionization of the complete subshell is a superposition of all contributions from photoelectrons originating from different magnetic subshells with the quantum numbers m_i :

$$\tau_{\text{W}}^{n_i \ell_i}(\Omega_{\mathbf{k}}) = \frac{\sum_{m_i = -\ell_i}^{\ell_i} w_{\ell_i m_i}(\varepsilon_{\text{COE}}, \Omega_{\mathbf{k}}) \tau_{\text{W}}^{\ell_i m_i}(\varepsilon_{\text{COE}}, \Omega_{\mathbf{k}})}{\sum_{m_i = -\ell_i}^{\ell_i} w_{\ell_i m_i}(\varepsilon_{\text{COE}}, \Omega_{\mathbf{k}})}. \quad (2.17)$$

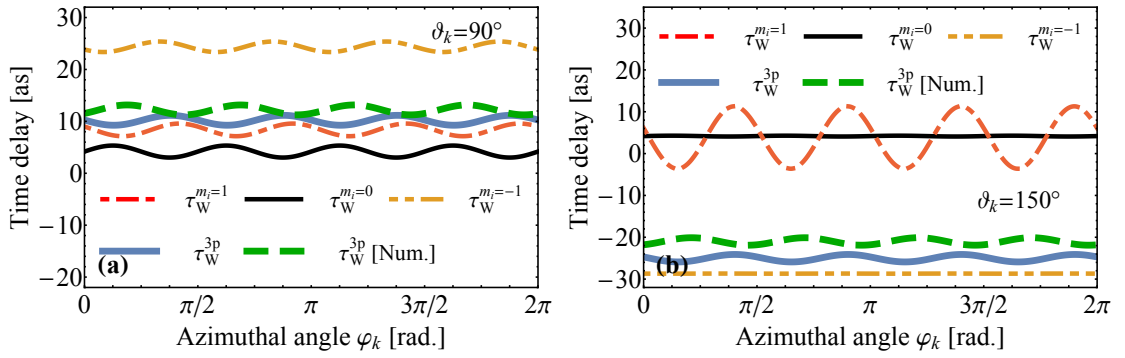


Fig. 2.4 Wigner Time delays as a function of the azimuthal angle $\varphi_{\mathbf{k}}$ for different directions $\vartheta_{\mathbf{k}}$ with respect of to optical axis of the optical vortex. The left column belongs to the photoionization process for $\vartheta_{\mathbf{k}} = 90^\circ$ where the photoelectron with $m_i = +1$ is dominant, while the right column is associated with $\vartheta_{\mathbf{k}} = 150^\circ$ (photoelectron with $m_i = -1$ dominates). Here a short pulse is considered, i.e. $n = 3$.

In addition to this quasi-analytical model, the 3DSE was solved numerically with the MIM technique and the time delays were extracted from the numerically obtained projection coefficients $a_i(\mathbf{k})$ at a propagation time after the vortex pulse is off.

In Fig. 2.4 the time delays in dependence on the emission angle are shown. They reveal a large difference between the photoionization processes from the initial magnetic substates with $m_i = 1$ or $m_i = -1$. The photon energy $\hbar\omega = 100$ eV and the considered topological charge $\ell_{\text{OAM}} = 1$. The photoionization probabilities in Fig. 2.2(b) evidence that for the angle $\vartheta_{\mathbf{k}} = 90^\circ$ the photoelectron originating from the magnetic subshell with $m_i = 1$ dominates while at $\vartheta_{\mathbf{k}} = 150^\circ$ the counter-rotating electron ($m_i = -1$) delivers the strongest contribution.

By investigating the corresponding time delays, the gathered trend is confirmed. In the case of photoionization in the xy -plane, i.e. $\vartheta_{\mathbf{k}} = 90^\circ$, we find that the full $3p$ time delay (includes the contributions from all magnetic substates) is nearly identical to the individual time delay $\tau_{\text{W}}^{\ell_i=1, m_i=1}$ of the initial magnetic sublevel with $m_i = 1$. On the contrary, the time delay $\tau_{\text{W}}^{\ell_i=1, m_i=-1}$ related to the counter-rotating electron has a different number and provides only a minor contribution to the full subshell delay due to the lower photoionization probability. The electron ionized from the initial state with $m_i = 0$ has no influence on the resulting time delay since there is no observable photoionization probability in the equatorial plane. Summarizing, the measured full time delay τ_{W}^{3p} is dominated by one photoelectron in this particular direction. The vanishingly small differences between the analytical model and the numerical propagation method give further credibility to the analytical explanations.

At the asymptotic direction $\vartheta_{\mathbf{k}} = 150^\circ$ the situation changes. The negative full time delay of the $3p$ subshell is nearly completely characterized by the individual time delay $\tau_{\text{W}}^{\ell_i=1, m_i=-1}$ corresponding to the counter-rotating electron which is also reflected by the photoionization

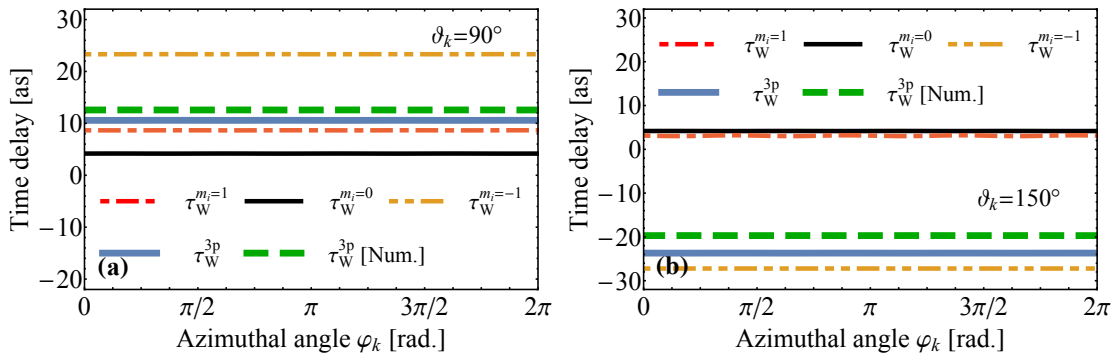


Fig. 2.5 Wigner Time delays as a function of the azimuthal angle φ_k for different directions ϑ_k with respect to the optical axis of the optical vortex. The situations where either (a) the co-rotating photoelectron or (b) the counter-rotating photoelectron dominates the photoionization process are shown. The long pulse duration is characterized by $n = 10$.

probability (cf. Fig. 2.2(b)). The other contributions from the initial sublevels with the magnetic quantum numbers $m_i = 0$ and $m_i = 1$ play a minor role.

In the Wigner time delay also the influence of the pulse duration is encapsulated. The results in Fig. 2.4 based on a short pulse characterized by the number of optical cycles $n = 3$ showed a pronounced variation on the azimuthal angle φ_k . The number of oscillations within 2π depends according to Eq. (2.13) and (2.12) on $\exp[i(2\ell_{\text{OAM}} + 2)\varphi_k]$ and is therefore four for $\ell_{\text{OAM}} = 1$. The results in Fig. 2.5 represent the same situations as illustrated in Fig. 2.4 for a longer pulse, i.e. the number of optical cycles is $n = 10$. It is immediately obvious that the angular modulation regarding the angle φ_k disappeared and now the time delays follow a straight line. This can be explained because the derivative of the emission coefficient $\partial \mathcal{E}_+ / \partial \varepsilon_k |_{\varepsilon_k = \varepsilon_{\text{COE}}}$ rapidly decreases with an increasing number of optical cycles n . In the equatorial plane [Fig. 2.5(a)] we find the full $3p$ time delay $\tau_W^{3p} = 10.7$ as which coincides almost with the value of the, in that case, dominating photoelectron contribution $\tau_W^{m_i=1} = 8.7$ as. In contrast at the asymptotic direction $\vartheta_k = 150^\circ$ [Fig. 2.5(b)] the subshell time delay τ_W^{3p} amounts to -23.5 as is therefore mainly characterized by $\tau_W^{m_i=-1} = -27$ as while the contributions of the co-rotating electron ($\tau_W^{m_i=+1} = 3.0$ as) and the photoelectron ionized from the initial magnetic substate with $m_i = 0$ ($\tau_W^{m_i=0} = 4.0$ as) have a minor role. Experimentally advantageous is the significant difference between both cases where either the co-rotating or the counter-rotating electrons dominate the photoionization process. We find a large difference $\Delta \tau_W^{3p}$ of 34.2 as which gives the opportunity to track back the origin of the photoelectrons via time delay measurements. More precisely, it is useful to identify the initial magnetic sublevel photoionized by the optical vortex beam. Furthermore, from the analytical considerations which are supported by the numerical results, it is foreseeable that these OAM light-induced effects are of a general nature and are not restricted to a particular system as long as spherical symmetry exists.

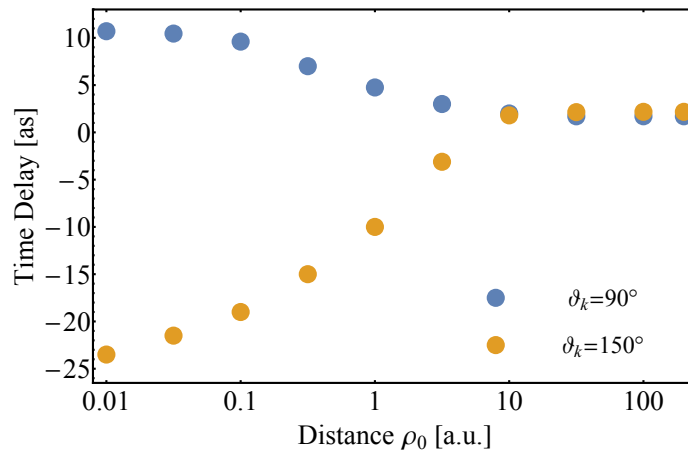


Fig. 2.6 The $3p$ time delays τ_W^{3p} corresponding to the situations where either the co-rotating or the counter-rotating electron dominates the photoionization process in dependence on the distance ρ_0 between the optical axis and the center of the argon atom. A long optical vortex laser pulse is considered, i.e. $n = 10$.

2.3.3 Dependence on the distance to the optical axis

Crucial for an experimental realization is the dependence of the resulting time delay on the distance ρ_0 (in the xy -plane) between the atom and the optical axis of the XUV optical vortex beam. It was already shown theoretically that the photoionization amplitude shows a substantial variation when the atom will be positioned away from the center of the light beam [124, 125]. The explanation is given by the transfer of the OAM which is maximal when the atom is inside the donut-shaped intensity distribution ($\rho_0 = 0$), i.e. the angle with respect to optical axis $\varphi'(\mathbf{r}) \equiv \varphi_k$ [126] [cf. Eq. 2.3 and 2.4]. Once the atom is positioned away from the center, $\varphi'(\mathbf{r}) \neq \varphi_k$ and only a fraction of the full 2π -interval is captured with the consequence that the transfer of OAM is limited. At the maximum of the intensity, i.e. at $\rho_{\max} = w_0/\sqrt{2}$, only the local spatial structure of the light beam is relevant. Here a Gaussian beam is resembled, and a further analyse reveals the well-known dipole selection rules $\ell_i \rightarrow \ell_i \pm 1$ and $m_i = m_i + 1$ as in the case of the linearly polarized light. The transfer of angular momentum is then only associated with the photon spin which depends on the polarization vector and not on the spatial structure. Therefore, far away from the optical axis, the whole process resembles the photoionization of the subshell with conventional circularly polarized light.

For the case the atom is not positioned at the optical axis of the vortex beam, the time delay can not be captured analytically. Therefore, a full numerical solution will be presented. In Fig. 2.6 we present the Wigner time in dependence on the distance ρ_0 between the atom and the optical axis of the OAM beam. The two situation where either the co-rotating ($\vartheta_k = 90^\circ$) or the counter-rotating photoelectron ($\vartheta_k = 150^\circ$) dominates the photoionization process are reflected by the numbers for $\rho_0 = 0$ which are in good agreement with the analytical results

depicted in Fig. 2.5. Surprisingly, even at small distances $\rho_0 \approx 1$ a.u., i.e. on the atomic scale, the difference between both time delays rapidly decreases which can be explained by the diminishing transfer of OAM. At a distance $\rho_0 = 10$ a.u., the time delays are nearly indistinguishable and therefore, the identification of the origin of the photoelectron via time delay measurements is not possible anymore. Here, the photoionization process can be described by using conventional circularly polarized light [80]. As another consequence, one could argue that measurements of the time delay using optical vortex beams allow the access to the magnetic information with an atomic-size resolution which does not violate the diffraction limit because all the information are delivered by the photoelectron and not obtained by optical microscopy methods.

2.3.4 Conclusion

The time delay in photoionization induced by light carrying orbital angular momentum was analyzed analytically and numerically. As a typical example, we considered Argon. The analytical results reveal that the effect due to the transfer of OAM is of a general nature and not restricted to a particular system as long as spherical symmetry exists. In contrast to using conventional laser beams, the angular distribution of the photoionization probability shows a substantial dependence on the magnetic quantum number m_i , i.e. the initial magnetic substate of the photoelectron has a decisive role. Asymptotic directions can be identified where the photoionization process, including all contribution of the possible initial states, is totally dominated by one magnetic sublevel. Thus, for the time delay a substantial difference between the situations where either the co-rotating or the counter-rotating electron (relative to the optical vortex) dominates can be found. As a consequence, time delay measurements are an interesting tool to identify the origin of the photoelectron. Furthermore, a strong dependence of the time delay on the position of the atom relative to beam spot can be found which allows measurements with an atomic-scale resolution.

2.4 Driving current loops in C₆₀ by optical vortex beams

2.4.1 Theoretical model

We consider here a linearly polarized, monochromatic Laguerre-Gaussian OAM pulse with a topological charge ℓ_{OAM} and a frequency ω which irradiates a C₆₀ molecule. The distance ρ_0 between the fullerene and the optical axis is variable. The whole initial situation is resembled in Fig. 2.1. The vector potential in cylindrical coordinates is given by Eq. (2.1) where all used approximations are described in section 2.2 of this chapter. We employ a diffraction limited beam implying $2w_0 \approx \lambda$ where w_0 is the waist of the beam which determines the radial extent of the optical vortex. The frequency is in the UV regime and

photon energies $\hbar\omega$ between 8 eV and 20 eV are considered, i.e. we need a waist size $w_0 = 50$ nm. The pulse length used in the calculations below is 10 fs while the intensity is moderate and amounts to $I = 3 \times 10^{13}$ W/cm².

The correct choice of the pulse parameters was decisive for our considerations. The intensity has to be low to legitimize a perturbative description of the whole process. Therefore, I/ω is small, so that we avoid strong field or tunneling effects and expect only single-photon transitions. Furthermore, as we are interested in the photo-induced magnetic field, the pulse duration should be shorter than the relaxation time of the associated current loop but has to allow for a few optical cycles. The special electronic structure of the C₆₀ molecule is the key element of the observed effects. Fullerenes are characterized by the quasi-spherical I_h point symmetry, and the coordinates of the inequivalent carbon atoms are well-known [133, 134, 136]. The single-particle states of the molecule are characterized by the principal quantum number n and have a well-defined angular quantum number ℓ . In addition to the quantum numbers, they are further specified by p_ℓ which discriminates between the different representations of the I_h symmetry group with the same orbital angular quantum number ℓ . The λ marks the element of the multi-dimensional representation p_ℓ . The bound state i with the quantum numbers n_i and ℓ_i is represented by the real wave function

$$\Psi_i(\mathbf{r}) = R_{n_i, \ell_i}(r) \sum_{m=-\ell_i}^{\ell_i} C_{\ell_i, m}^{p_{\ell_i}, \lambda} Y_{\ell_i, m}(\Omega_{\mathbf{r}}). \quad (2.18)$$

The coefficients $C_{\ell_i, m}^{p_{\ell_i}, \lambda}$ corresponding to the p_{ℓ_i} representation within the I_h -symmetry point group are tabulated in Ref. [147]. The radial wave functions $R_{n_i, \ell_i}(r)$ and the corresponding energy eigenvalues $\varepsilon_i \equiv \varepsilon_{n_i, \ell_i, p_{\ell_i}}$ were calculated with the aid of the HF method implemented in GAUSSIAN 03 quantum chemistry package [148].

The electron states occupy two radial bands (σ and π band) which are characterized by the principal quantum number n . Taking the electron spin into account, the σ band ($n = 1$) is occupied by 180 electronic states whereas the maximal angular quantum number is given by $\ell_{\max} = 9$. The corresponding orbital for $\ell = 9$ is only filled with 9 electrons. Thus, only the g_u and h_u representation groups are occupied [134]. The second radial band (π -band) is filled with 60 electronic states (including the spin degeneracy) leading to a maximal orbital quantum number $\ell_{\max} = 5$. Again, the HOMO orbital with $\ell = 5$ is only partly occupied, i.e. only the h_u representation group is filled [149]. Astonishingly, we find a nearly perfectly parabolic dispersion curve $\varepsilon_i = \varepsilon_{n_i=2, \ell=0} + \ell_i(\ell_i + 1)/2R^2$ for $\ell < 3$ where $R = 6.745$ a.u. is the averaged radius of the C₆₀ molecule. The reason is that the S,P,D orbitals transform as a_g , t_{1u} and h_g , respectively, in the I_h point symmetry. A small splitting can be found for larger ℓ because of the $SO(3) \rightarrow I_h$ symmetry-break. However, in the case of the π band, this splitting is smaller than 0.5 eV [133].

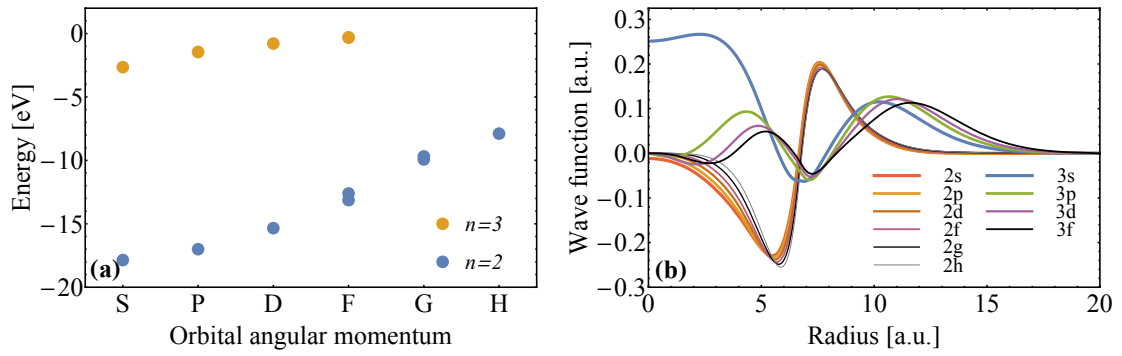


Fig. 2.7 (a) The energy spectrum and (b) the corresponding normalized wave functions of the second and third radial band of the C₆₀ molecule.

In addition to the two occupied radial bands, we find a group of virtual but still bound (by the central molecular potential) states with a well-defined angular character which are called super atomic molecular orbitals (SAMOs). This special group of virtual states occupy a third radial band and are characterized by the principal quantum number $n = 3$. A very important feature is the well-defined angular character of the SAMOs. Thus, the corresponding wave functions can also be represented by Eq. (2.18) with the energy eigenvalues $\epsilon_{n=3,\ell,p_\ell}$. However, due to the correlation effects, it is very difficult to capture their exact energetic position theoretically [133, 134, 136, 138–140]. The calculation of the corresponding wave functions and corresponding energy eigenvalues were again performed with the aid of the GAUSSIAN 03 quantum chemistry package [126]. We sought for 248 excited states of C₆₀ in the active window of (121, 366) molecular orbitals while using the experimental geometry with the bond lengths $d_{C=C} = 1.402 \text{ \AA}$ between two hexagons and $d_{C-C} = 1.462 \text{ \AA}$ between a hexagon and a pentagon. The abovementioned well-defined angular character applies only for low angular quantum numbers ℓ . Therefore, the maximal angular momentum is restricted to $\ell_{\max} = 3$. Consequently, we expect a small split of the energy levels due to $\text{SO}(3) \rightarrow I_h$ symmetry-break because the F-orbital transforms into the t_{2u} and g_u representation classes. Indeed, this separation is smaller than 0.05 eV [133].

In the investigation below, we consider only transitions between the π band and the SAMOs. The corresponding energy scheme and the involved radial wave functions are shown in Fig. 2.7. Therefore, the frequency regime is restricted to photon energies $\hbar\omega$ between 8 eV and 20 eV. The temporal envelope of the optical vortex pulse is modeled as $\Omega(t) = e^{-\delta t^2}$ where $\delta = 2.5 \times 10^{-5} \text{ a.u.}$ for the considered duration of 10 fs.

For the considered low intensities of the vortex beam, single-photon processes dominate the light-matter interaction. Therefore, we can describe the time-dependent wave function $\Psi_i(\mathbf{r}, t)$ which evolves from the initial state i (characterized by the eigenvalue ϵ_i , the quantum numbers n_i and ℓ_i as well as the parameters p_{ℓ_i} and λ) in the framework of the perturbation theory. The deviation $\delta\Psi_i(\mathbf{r}, t)$ from the ground state i due to the action of $\hat{H}_{\text{int}}(t)$, described

by Eq. (2.5), can be treated, to the first order in $|A(\mathbf{r}, t)|$, as an expansion over the unperturbed and unoccupied eigenstates of the system:

$$\delta\Psi_i(\mathbf{r}, t) = \sum_j C_j(t) e^{-i\varepsilon_j t} \Psi_j(\mathbf{r}). \quad (2.19)$$

The time-dependent interaction Hamiltonian can further be divided into two parts: $\hat{H}_{\text{int}}(t) = H_{\text{Int}}(\mathbf{r})\Omega(t)e^{-i\omega t} + H_{\text{Int}}^*(\mathbf{r})\Omega(t)e^{i\omega t}$. Using the standard techniques of the perturbation theory, the projection coefficients are evaluated as

$$C_j(t) = i \left[G_{\varepsilon_j, \varepsilon_i}^-(t) \langle \Psi_j | H_{\text{Int}} | \Psi_i \rangle + G_{\varepsilon_j, \varepsilon_i}^+(t) \langle \Psi_j | H_{\text{Int}}^* | \Psi_i \rangle \right]. \quad (2.20)$$

Here the absorption and emission coefficients are defined as the Fourier transforms of the temporal envelope of the OAM beam:

$$G_{\varepsilon_j, \varepsilon_i}^\mp(t) = \int_{-\infty}^t d\tau \Omega(\tau) e^{i(\varepsilon_j - \varepsilon_i \mp \omega)\tau}. \quad (2.21)$$

The matrix element $M_{ji} = \langle \Psi_j | H_{\text{Int}} | \Psi_i \rangle$ describes the transition from the occupied state i to the unoccupied state j due to the interaction with the optical vortex pulse. It can only be derived analytically for the special case when the distance ρ_0 between the center of the molecule and the optical axis of the vortex beam is zero. Otherwise, a full numerical calculation is needed because φ' and ρ' (relative to the OAM pulse) become functions of \mathbf{r} (relative to the molecule) and has to be translated according to Eq. (2.3) and (2.4). In principle, the case of $\rho_0 = 0$ is already demonstrated in section 2.3 of this thesis where we derived the optical selection rule $\Delta L \leq \ell_{\text{OAM}} + 1$ analytically.

Now we introduce the time T_{off} where the laser pulse is truly off. For final times $t_f > T_{\text{off}}$ we find that $G_{\varepsilon_j, \varepsilon_i}^\mp(t_f) = G_{\varepsilon_j, \varepsilon_i}^\mp(T_{\text{off}})$ which means that the time-dependence of the coefficients C_j disappears. Furthermore, one can show that $G_{\varepsilon_j, \varepsilon_i}^-(t_f) \gg G_{\varepsilon_j, \varepsilon_i}^+(t_f)$. Therefore, we are able to neglect the part of C_j which describes the emission process and find that

$$C_j(t_f) = i G_{\varepsilon_j, \varepsilon_i}^-(T_{\text{off}}) M_{ji}. \quad (2.22)$$

Henceforth, $G_{\varepsilon_j, \varepsilon_i}^- \equiv G_{\varepsilon_j, \varepsilon_i}$.

For our purpose, the photo-induced current density after the interaction with the pulse, i.e. for $t_f > T_{\text{off}}$, has to be evaluated according to $\mathbf{j}(\mathbf{r}) = \sum_i^{\text{occ.}} \Im \{ \Psi_i^*(\mathbf{r}, t_f) \nabla \Psi_i(\mathbf{r}, t_f) \}$. The current density has fast oscillating and slowly decaying (DC) elements. We introduce now the time scale T_{obs} where the current can be observed, i.e. T_{obs} is comparable to the typical lifetime of the excited SAMO states. Therefore, $T_{\text{obs}}\eta \simeq 1$ where η is the effective decay constant of excited states. Consequently, the DC component of the current density can be extracted by time-averaging over the fast oscillating contribution. The evaluation yields to

the following analytical result:

$$\mathbf{j}(\mathbf{r}) = \sum_i^{\text{occ.}} \Im \left\{ \frac{1}{T_{\text{obs}}} \int_{T_{\text{off}}}^{T_{\text{off}}+T_{\text{obs}}} \sum_{j,k}^{\text{unocc.}} \langle \psi_i | H_{\text{int}} | \psi_j \rangle \langle \psi_k | H_{\text{int}} | \psi_i \rangle \right. \\ \left. \times G_{\varepsilon_j, \varepsilon_i}^* G_{\varepsilon_k, \varepsilon_i} e^{i(\varepsilon_j - \varepsilon_k)t} \psi_j^*(\mathbf{r}) \nabla \cdot \psi_k(\mathbf{r}) dt \right\}. \quad (2.23)$$

Introducing the decay by the exponential factor $e^{-\eta t}$ we obtain immediately that the time integral $\frac{1}{T_{\text{obs}}} \int_{T_{\text{off}}}^{T_{\text{off}}+T_{\text{obs}}} e^{i(\varepsilon_j - \varepsilon_k)t} e^{-\eta(t-T_{\text{off}})}$ preferentially picks up the contributions of the states which fulfill $|\varepsilon_j - \varepsilon_k| < \eta$. In other words, the cases where $\varepsilon_j = \varepsilon_k$ yield the largest contributions to the current density. Therefore, the obtained current density can be further simplified to

$$\mathbf{j}(\mathbf{r}) = \sum_i^{\text{occ.}} \Im \left\{ \sum_{\ell, p_\ell}^{\text{unocc.}} \sum_{\lambda, \lambda'} M_{n\ell p_\ell \lambda, n_u \ell_i p_\ell, \lambda_i}^* M_{n\ell p_\ell \lambda', n_i \ell_i p_\ell, \lambda_i} \right. \\ \left. \times \left| G_{\varepsilon_{n\ell p_\ell}, \varepsilon_i} \right|^2 \psi_{n\ell p_\ell \lambda}^*(\mathbf{r}) \nabla \cdot \psi_{n\ell p_\ell \lambda'}(\mathbf{r}) \right\}. \quad (2.24)$$

The sums of the elements λ, λ' within the representation group p_ℓ are present because the energy eigenvalues are degenerated with respect to λ .

The current density can be expressed as $\mathbf{j}(\mathbf{r}) = j_r(\mathbf{r})\hat{e}_r + j_\vartheta(\mathbf{r})\hat{e}_\vartheta + j_\varphi(\mathbf{r})\hat{e}_\varphi$, where $j_r(\mathbf{r})$, $j_\vartheta(\mathbf{r})$ and $j_\varphi(\mathbf{r})$ describe the densities in radial, orbital and azimuthal directions. Extensive numerical calculations reveal that for single photon processes the radial and orbital contributions current density disappear, i.e. $j_r(\mathbf{r}) = j_\vartheta(\mathbf{r}) = 0$ since the ionization channel is closed.

2.4.2 Photo-induced magnetic moment

The magnetic moment induced by a ring current can be evaluated by [150]

$$\mathbf{m} = \frac{1}{2} \int d\mathbf{r} [\mathbf{r} \times \mathbf{j}(\mathbf{r})]. \quad (2.25)$$

In our case the magnetic moment points in the z direction because only the angular component j_φ contributes to the total current density.

In Fig. 2.8 the photo-induced magnetic moment in the z -direction in dependence on the photon energy $\hbar\omega$ and the molecule's position relative to the optical axis of the vortex beam is presented where the cases with topological charges $\ell_{\text{OAM}} = 1$ and $\ell_{\text{OAM}} = 2$ are shown. A linearly polarized Gaussian pulse, which is resembled for $\ell_{\text{OAM}} = 0$, would not generate any DC current because the degeneracy of the magnetic substates can not be rescinded. Therefore, the visible magnetic moments are solely the result of the transfer of OAM due to the interaction of the molecule with the optical vortex.

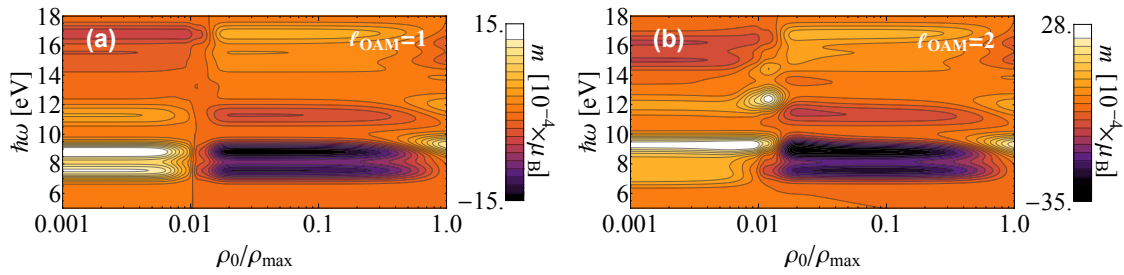


Fig. 2.8 The magnetic moment in dependence on the distance between the optical axis and the center of the molecule (characterized by the ratio ρ_0/ρ_{\max}) and the photon energy $\hbar\omega$ for (a) $\ell_{\text{OAM}} = 1$ and (b) $\ell_{\text{OAM}} = 2$.

The multiple peaks of the magnetic moment in dependence on the photon energies can be explained by the variety of possible resonant transitions between electronic states within the π band and the SAMOs [cf. the energy scheme Fig. 2.7(a)]. More surprising and probably unexpected is the smooth dependence of the magnetic moment on the position of the molecule relative to the optical axis which is given by the ratio ρ_0/ρ_{\max} . It shows the same order of magnitude for the fullerene at different positions in the laser beam.

This behavior is not generic but due to the mechanism of the OAM transfer. The topological charge ℓ_{OAM} , which characterizes the amount of transferable OAM, is defined relative to the optical axis of the vortex beam. The optimal setting is reached when the symmetry axis of the fullerene coincides with the center of the optical vortex, i.e. $\rho_0/\rho_{\max} = 0$. In that case φ' (which enters the vector potential according to Eq. (2.1)) is equivalent to φ which is relative to the center of the molecule. This is also emphasized by the optical selection rules for different topological charges ℓ_{OAM} . For the ratio $\rho_0/\rho_{\max} = 0$, the photo-induced transitions are governed by the selection rule $\Delta\ell \leq \ell_{\text{OAM}} + 1$ ($\Delta\ell + \ell_{\text{OAM}}$ odd) which is similar to our investigation in section 2.2, as well as to the results given in Ref. [127, 151]. Since the magnetic quantum number m is no adequate quantum number for describing the electronic structure of the C_{60} molecule the selection rule is restricted to the orbital angular quantum number ℓ .

However, since the average radius R of the system is small in comparison to the waist w_0 of the beam, i.e. $R \ll w_0$, the electronic states are only weakly excited due to the low intensity in the center of the optical vortex. The situation is totally different for $\rho_0 = \rho_{\max}$, i.e. for positioning the molecule at the maximum of intensity of the OAM beam. Here the angle φ' is a function of the vector \mathbf{r} and only a tiny fraction of the whole 2π -interval is covered, and therefore, the transfer of OAM with respect to the fullerene cage center is limited. However, the intensity is very high which leads to photo-induced transitions between the π band and the third radial band. The transitions are governed by the dipole selection rule $\Delta\ell = 1$ since the whole process resembles now the interaction of the molecule with a conventional Gaussian beam. The interplay between both extreme situations, i.e. low intensity/maximal

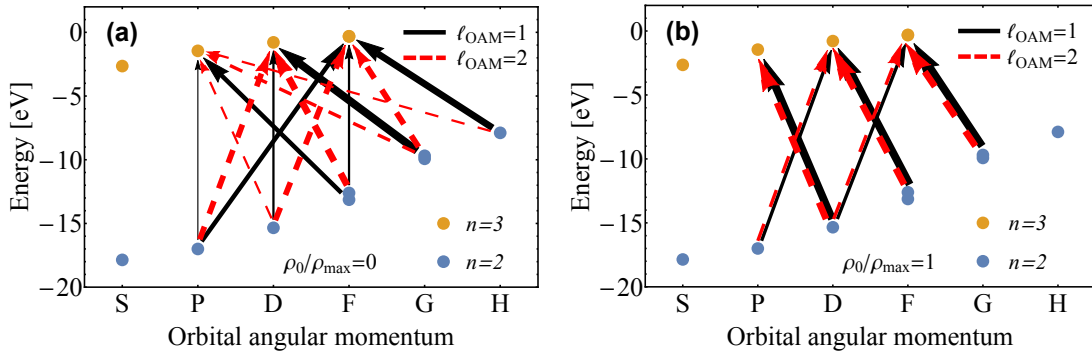


Fig. 2.9 The various possible transitions in dependence on the topological charge ℓ_{OAM} for (a) $\rho_0/\rho_{\text{max}} = 0$ and (b) $\rho_0 = \rho_{\text{max}}$.

transfer of OAM at $\rho_0/\rho_{\text{max}} = 0$ and maximal intensity/weak transfer of OAM at $\rho_0 = \rho_{\text{max}}$, leads to the relatively smooth dependence of the magnetic moment on the position of the molecule relative to the optical axis.

The selection rules, which can be revealed by contrasting with the energy scheme, are emphasized in the transition schemes in Fig. 2.9. The both extreme situations $\rho_0 = 0$ and $\rho_0 = \rho_{\text{max}}$ are presented. Thick arrows mark here the dominant transitions, which are directly visible in the spectra of the magnetic moments in Fig. 2.8.

In the case of $\ell_{\text{OAM}} = 1$ for $\rho_0/\rho_{\text{max}} = 0$ (molecule is in the center of the beam), we find two pronounced positive peaks at 7.6 eV and 8.8 eV which belong to the interband transitions $(n_i = 2, \ell_i = 5) \rightarrow (n_f = 3, \ell_f = 3)$ and $(n_i = 2, \ell_i = 4) \rightarrow (n_f = 3, \ell_f = 2)$. The final states belong here to the third radial band with the orbital angular momenta $\ell_f = \ell_i + \Delta\ell$. Another prominent peak is at 11.3 eV which marks the $(n_i = 2, \ell_i = 3) \rightarrow (n_f = 3, \ell_f = 1)$ transition, while a negative magnetic moment can be found at 16.7 eV which is characterized by $(n_i = 2, \ell_i = 1) \rightarrow (n_f = 3, \ell_f = 3)$. The condensed selection rules are reflected in the transition scheme shown in Fig. 2.9(a) by comparing with the thick arrows. In general transitions from larger orbital angular momenta ℓ_i to smaller momenta ℓ_f yield to a positive magnetic moment while we observe a negative quantity for the opposite.

In the case of $\ell_{\text{OAM}} = 2$ (Fig. 2.8(b)) for $\rho_0/\rho_{\text{max}} = 0$, the spectrum reveals nearly the same positions of pronounced magnetic momentum peaks although a detailed look at the prominent positive peak leads to a spot at 9.3 eV. This maximum is characterized by the transition $(n_i = 2, \ell_i = 4) \rightarrow (n_f = 3, \ell_f = 3)$ which confirms the selection rule $\Delta\ell \leq 3$ ($\Delta\ell + 2$ odd). Another pronounced dominant peaks can be found at 12 eV corresponding to the transition $(n_i = 2, \ell_i = 3) \rightarrow (n_f = 3, \ell_f = 2)$, while the negative magnetic moments at 15 eV and 16.3 eV are characterized by $(n_i = 2, \ell_i = 1) \rightarrow (n_f = 3, \ell_f = 2)$ and $(n_i = 2, \ell_i = 2) \rightarrow (n_f = 3, \ell_f = 3)$. Again, these transitions are represented nicely in the form of the thick arrows in the corresponding scheme which is shown in Fig. 2.9(a).

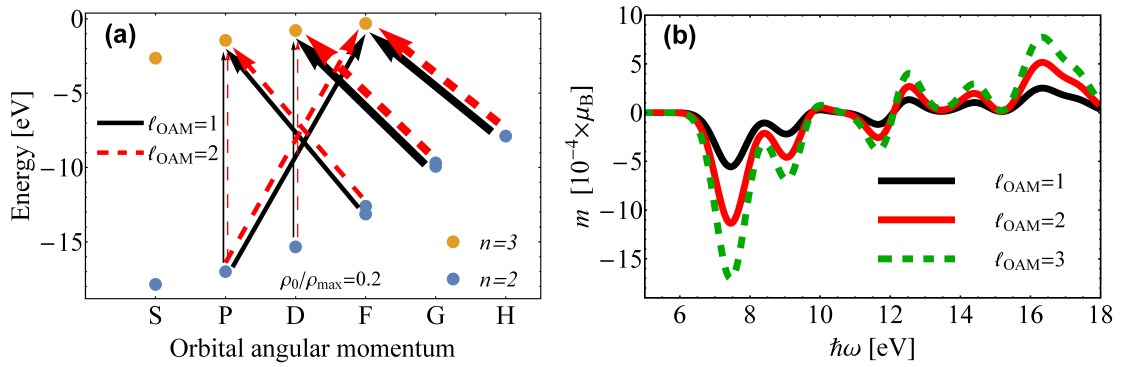


Fig. 2.10 (a) Transition scheme for $\rho_0/\rho_{\max} = 0.2$. (b) The over a homogeneous gas-phase averaged photo-induced magnetic moment in dependence on the photon energy $\hbar\omega$ for different topological charges ℓ_{OAM} .

Despite the different optical selection rules in dependence on the topological charge ℓ_{OAM} , we find only small discrepancies between the corresponding spectra of the magnetic moments. The explanation is given by the small energy differences between the various SAMOs states. Taking into account that the transitions to virtual states with $\ell_f = 0$ deliver no current, we find an energy difference lesser than 1.2 eV between the SAMO states with $l_f = \text{P, D, F}$. The energy level splitting of 0.08 eV for $l_f = 3$ due to the $\text{SO}(3) \rightarrow I_h$ symmetry breaking is already included. For a better resolution of the corresponding spectra and to emphasize the different optical selection rules stronger, the duration of the pulse has to be much longer which comes along with much sharper magnetic moment peaks.

At larger distances between the optical axis of the vortex beam and the center of the fullerene, up to $\rho_0/\rho_{\max} > 0.01$, the discrepancies between the different transitions for varying values of the topological charge ℓ_{OAM} vanish completely. Henceforth, all optical transitions initiated by the interaction with the OAM beam are fully characterized by the same selection rules. As a consequence, all magnetic moment peaks can be found at the same photon energies which can be explained by the reduced transferred OAM when translated to the fullerene cage. The reason is the phase structure of the optical vortex which changes drastically even on the atomic scale [127].

The dipole selection rule $\Delta L = 1$, which characterizes the transitions when the molecule is placed at the maximum of intensity, i.e. $\rho_0/\rho_{\max} = 1$, can be identified in the spectra in Fig. 2.8 and the corresponding transition schema in Fig. 2.9(b). The prominent positive peaks at the photon energies 9.3 eV and 12.1 eV correspond to the transitions $(n_i = 2, \ell_i = 4) \rightarrow (n_f = 3, \ell_f = 3)$ and $(n_i = 2, \ell_i = 3) \rightarrow (n_f = 3, \ell_f = 2)$ for all ℓ_{OAM} which are also emphasized by the thick arrows in the transition scheme.

In Fig. 2.10(a) we show the intermediate transition scheme for $\rho_0/\rho_{\max} = 0.2$ which lies between both extreme situations mentioned above. It reveals that the transitions are determined by non-dipolar contributions, i.e. $\Delta L = 0$ and $\Delta L = 2$, but independent of the

considered topological charge. Therefore, also in this case, the vanishing transfer of OAM for large distances between the molecule and the optical axis is underlined. By contrasting with the magnetic moment spectra in Fig. 2.8 we can explain the peak at 7.6 eV by the transition $(n_i = 2, \ell_i = 5) \rightarrow (n_f = 3, \ell_f = 3)$, while the pronounced magnetic moment at 8.9 eV belongs to $(n_i = 2, \ell_i = 4) \rightarrow (n_f = 3, \ell_f = 2)$. The prominent positive peak is characterized at 16.7 eV is characterized by $(n_i = 2, \ell_i = 1) \rightarrow (n_f = 3, \ell_f = 3)$ transition. Nevertheless, the resulting magnetic moments are not completely independent of the topological charge ℓ_{OAM} although they reveal the same photo-induced transitions for $\rho_0/\rho_{\text{max}} > 0.01$. This circumstance is emphasized by the averaging the magnetic moment in the range from $\rho_0 = 0$ to $\rho_0 = \rho_{\text{max}}$ which is presented in Fig. 2.10(b). Here, also the case of the topological $\ell_{\text{OAM}} = 3$ is shown. In an experimental realization, the fullerenes are in a dilute gas phase which is irradiated by the optical vortex pulse. Therefore, the C₆₀ molecules are distributed over the whole beam spot and the corresponding individual photo-induced magnetic moments vary in sign as well as in magnitude. Nevertheless, the averaging demonstrates that the individual signals do not cancel each other and a substantial total magnetic moment can be observed.

Furthermore, two characteristics are noticeable: First, the dependence of the averaged magnetic moment on the photon energy $\hbar\omega$ exploits the electronic structure of the fullerenes because several transitions between π -band and the SAMOs are involved and visible. Second, it is revealed that the magnitude of comprehensive magnetic moment depends on the topological charge ℓ_{OAM} . A higher winding number delivers a higher current and a more distinct magnetic moment. The condition is that appropriate highly degenerate states for the photo-induced transitions are available. This effect can be explained by the factor $e^{i\ell_{\text{OAM}}\varphi'(\mathbf{r})}$ in Eq. (2.1). Although the covered $\varphi'(\mathbf{r})$, when translated to the system, is small for large distances ρ_0 of the molecule to the optical axis, it produces additional non-dipolar transitions to states within the representation p_{ℓ_f} with the same energy $\varepsilon_{n_f \ell_f p_{\ell_f}}$. A larger ℓ_{OAM} delivers contributions $C_{\ell_f, m}^{p_{\ell_f}, \lambda} Y_{\ell_f, m}$ with larger m (cf. Eq. (2.18)), which are encapsulated in the matrix elements $\langle \Psi_f | H_{\text{Int}} | \Psi_i \rangle$, to the current density and therefore, higher magnetic moments can be achieved.

2.4.3 Magnetic field

In Fig. 2.10 we show explicitly the current densities corresponding to the positive peak of the magnetic moment at 8.8 eV when the molecule is positioned at the intensity maximum of the vortex beam, i.e. $\rho_0 = \rho_{\text{max}}$. The choice of the topological charge is subsidiary because the position of the peak is independent on ℓ_{OAM} . Therefore, we show the current density in the case of $\ell_{\text{OAM}} = 1$.

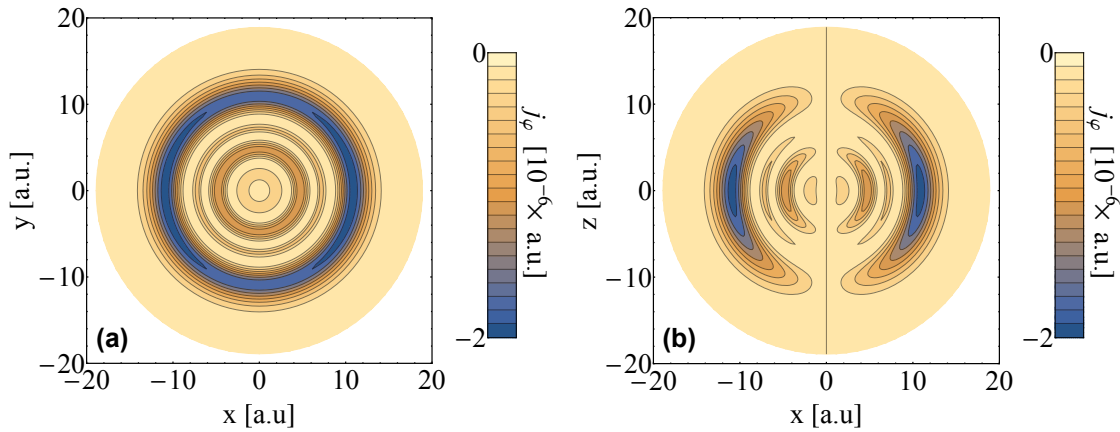


Fig. 2.11 The current density $j_\varphi(\mathbf{r})$ for a photon energy $\hbar\omega = 8.8$ eV and a topological charge $\ell_{\text{OAM}} = 1$ in (a) the xy -plane and (b) the xz -plane.

The presentation in the xy -plane reflects the structure of SAMOs nicely since the current density forms three intensive intercalated ring structures. They can be explained by the radial wave functions of the SAMOs [cf. Fig. 2.2(a)] which have two nodes and therefore three extrema. Furthermore, $j_\varphi(\mathbf{r})$ is nearly independent of the angle φ which is characteristic for spherical objects [151]. The presentation in the xz -plane reveals that the current density forms an onion-like structure with the maximal values in the equatorial plane.

The photo-induced circulating current is located around the shell of the C₆₀ molecule and induces a similarly localized magnetic field which can be calculated with the aid of the Biot-Savart law [150]:

$$\mathbf{B}(\mathbf{r}) = \frac{\mu}{4\pi} \int d\mathbf{r}' \mathbf{j}(\mathbf{r}') \times \frac{\mathbf{r} - \mathbf{r}'}{|\mathbf{r} - \mathbf{r}'|^3}. \quad (2.26)$$

In contrast to the current density, the high influence of the topological charge ℓ_{OAM} is revealed by inspecting the generated magnetic field inside the center, i.e. for $r = 0$. In Fig. 2.12 we show the two extreme situations $\rho_0 = 0$ and $\rho_0 = \rho_{\text{max}}$ which unveil partly different characteristics.

The case of $\rho_0 = 0$ in Fig. 2.12(a) belongs to the photon energy $\hbar\omega = 8.8$ eV and the corresponding magnetic field shows a substantial dependence on the topological charge. At $\ell_{\text{OAM}} = 0$ we find no generated magnetic field which can be explained because in that case a conventional linearly polarized Gaussian beam is resembled. Therefore, no OAM is transferred, and the degeneracy of the states can not be lifted. The maximal transferable OAM is restricted by $\ell_{\text{OAM}} = 7$ which is a consequence of the selection rule $\Delta\ell \leq \ell_{\text{OAM}} + 1$ and the underlying electronic structure of C₆₀. The maximal orbital angular quantum number of the third radial band is $\ell_{\text{max}} = 3$. Therefore, i.e. the highest possible transition is given by $\varepsilon_{n_i=2, \ell_i=5} \rightarrow \varepsilon_{n_f=3, \ell_f=3}$. The magnitude of the generated magnetic field is in the regime of μT .

The situation changes in the case of $\rho_0 = \rho_{\text{max}}$ shown in Fig. 2.12(b). The used photon

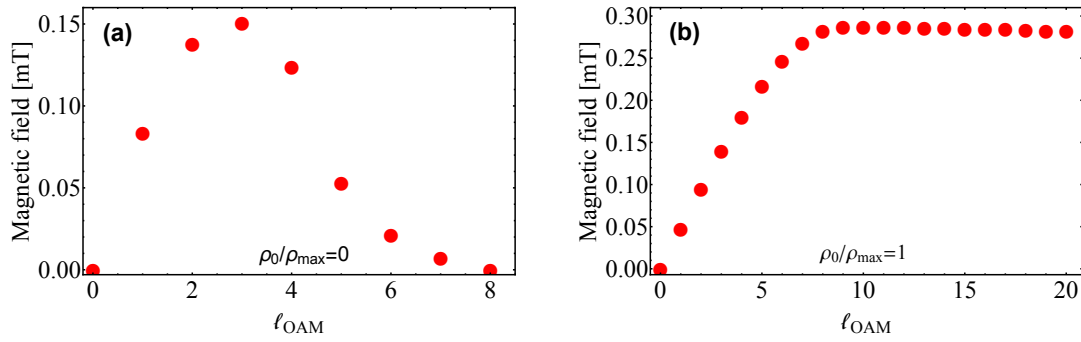


Fig. 2.12 The photo-induced magnetic fields in the center of the C₆₀ molecule in dependence on the topological charge m_{OAM} for (a) $\rho_0 = 0$ and (b) $\rho_0 = \rho_{\max}$.

energy $\hbar\omega = 9.3$ eV which corresponds to the positive peak of the magnetic moment in the spectra showed in Fig. 2.8. It is immediately obvious that we observe no restriction on the topological charge. Consequently, higher topological charges can be used for a more pronounced current generation as long as $l_{\text{OAM}} < 10$. For small winding numbers, the photo-induced magnetic field shows a strong dependence, e.g., by changing the l_{OAM} from 1 to 2 the amplitude is doubled. In the case of $l_{\text{OAM}} = 0$, no magnetic field can be found which can be explained with the same arguments as for $\rho_0 = 0$. Nevertheless, the underlying electronic structure has a substantial effect since for $l_{\text{OAM}} > 10$ the magnetic field does not increase further. Therefore, we find a saturation effect which can be explained by the limited number of degenerate unoccupied states in the third radial band of the fullerene. Consequently, the amount of maximal transferrable OAM is determined by the band structure.

In Fig. 2.13 an illustration of the field lines corresponding to the photo-induced magnetic field is shown. In that case, the C₆₀ molecule is positioned at the maximum of intensity of the vortex beam. The strongest field can be observed in the center of the fullerene while it decreases very fast outside the fullerene. As expected, inside the carbon cage, the field lines point in the z -direction which is explained due to the circulating current on the sphere which has its maximum in the equatorial plane. Outside the molecule, the photo-induced magnetic field decreases rapidly which means that the effect is very localized.

2.4.4 Conclusion

The possibility of generating circulating charge currents on the sphere of a C₆₀ molecule was demonstrated theoretically by using light carrying orbital angular momentum. The capability of transferring OAM to the irradiated the molecule enables resonant non-dipolar transitions from the occupied states to the recently discovered super atomic molecular virtual orbitals. We calculated a photo-induced current loop which generates a magnetic pulse inside the carbon cage in the range of μT . Furthermore, we demonstrated that the current

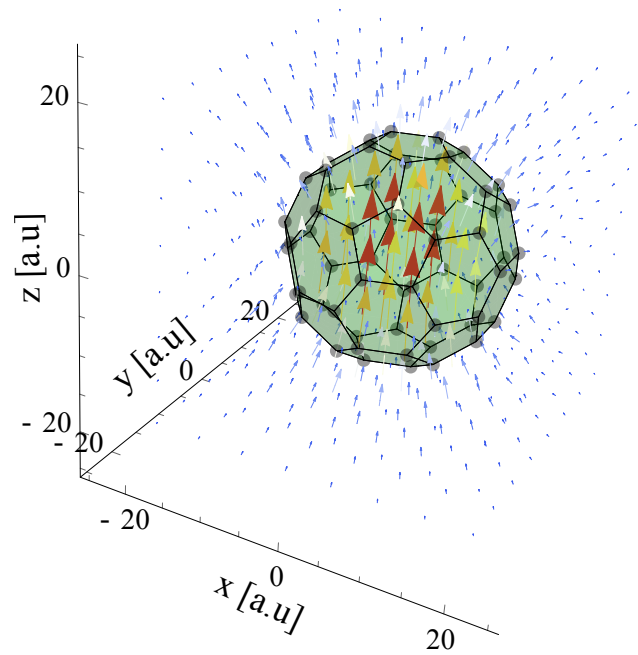


Fig. 2.13 Photo-induced magnetic field for a C_{60} molecule positioned at the maximum of intensity and a optical vortex beam with a photon energy $\hbar\omega = 9.3$ eV. The color scale characterizes the amplitude: red arrows mark the strongest contribution while the blue color reveals a weak field.

could be controlled in sign and magnitude by changing the topological charge ℓ_{OAM} of the optical vortex while the pulse duration and intensity are fixed.

A very smooth dependence of the photo-induced magnetic moment on the distance between the center of the molecule and the optical axis of the OAM beam is found. The characteristics of the photo-induced magnetic field inside the fullerene demonstrate that the electronic band structure sets the maximal amount of transferrable OAM. As a consequence, much larger photo-induced current loops should be generated by considering larger objects which possess highly degenerate SAMOs. Hence, the usage of OAM beams for generating magnetic pulses gives the full potential when on the one hand the topological charge ℓ_{OAM} is very high, and on the other hand a large number of virtual states exist.

2.5 Centrifugal photovoltaic effect induced by optical vortex beams

2.5.1 Details of the investigation

In the following investigation, we consider an experimentally feasible circularly OAM laser with a moderate intensity driving intraband dynamics of the conduction band carriers in a ballistic GaAs-AlGaAs-based nano-size ring. Such quantum ring structures are experimen-

tally reported in Refs. [141, 142]. The time evolution of the charge carriers under the action of the optical vortex beam is computed and reveals strong effects due to the ongoing transfer of OAM. Furthermore, we will also calculate the OAM-laser driven charge current in wires which are attached to the ring structure. We restrict our consideration to the xy -plane by choosing a very small thickness of the ring and the wires. Therefore, no dynamics occur along the propagation direction of the laser beam due to quantum confinement.

As a radial confinement potential we employ the confinement potential of Ref. [152], i.e. $V(r) = \frac{a_1}{r^2} + a_2 r^2 - V_0$, where $r = \sqrt{x^2 + y^2}$ and $V_0 = 2\sqrt{a_1 a_2}$. The key parameters a_1 and a_2 can be determined by choosing the average radius of the ring $r_0 = (a_1/a_2)^{1/4}$ and the width of the ring $\Delta r \approx \sqrt{8\varepsilon_F/m^* \omega_0^2}$ at the Fermi energy ε_F while $\omega_0 = \sqrt{8a_2/m^*}$ and m^* is the electron effective mass. The potential of the ring becomes parabolic when r is approaching r_0 . In that case $V(r) \approx \frac{1}{2}m^* \omega_0^2 (r - r_0)^2$. Taking $a_1 \approx 0$ then $V(r)$ describes a quantum dot.

In our case of the considered GaAs-AlGaAs-based ballistic ring, we assume a uniform effective mass $m^* = 0.067m_e$. For the average radius we choose as $r_0 = 150$ nm with a width $\Delta r = 50$ nm and the Fermi energy $\varepsilon_F = 8$ meV. The numerical solution of the stationary two-dimensional Schrödinger equation $\hat{H}_0 \Psi_{l_0, m_0}(x, y) = E_{l_0, m_0} \Psi_{l_0, m_0}(x, y)$, where the field-free hamiltonian \hat{H}_0 incorporates the above-described confinement potential, reveals the stationary, unperturbed energy eigenvalues E_{l_0, m_0} and wave functions $\Psi_{l_0, m_0}(x, y)$ of the electron states. The corresponding local density of states (LDOS) can be calculated according to

$$D(x, y) = \sum_{l_0, m_0} f^0(l_0, m_0) |\Psi_{l_0, m_0}(x, y)|^2, \quad (2.27)$$

where $f^0(l_0, m_0) = 1/[1 + \exp((E_{l_0, m_0} - \varepsilon_F)/k_B T)]$ is the equilibrium Fermi-Dirac distribution for a given temperature T and Fermi energy ε_F .

The initial energy levels E_{l_0, m_0} , shown in Fig. 2.14(a), form subbands and are classified by the two quantum numbers l_0 and m_0 , where $l_0 = 1, 2, 3, \dots$ characterizes the radial motion in the ring while angular motion is described by the angular momentum m_0 . The energy spectrum reveals the expected degeneration of the initial states with respect to the clock-wise and anti-clock-wise angular motion, i.e. $E_{l_0, m_0} = E_{l_0, -m_0}$. The consequence of that symmetric behavior is that the whole ring system carries no current. The LDOS in Fig. 2.14(b) reveals an independence of the angle φ in the xy -plane and a radial symmetry with respect to the average radius r_0 . Important for the validity of our consideration is that we will be interested in non-invasive excitations in the near the Fermi energy due to the moderate intensity of the laser pulse. Therefore, the independent effective single particle picture is still feasible [152–156].

In the following, the weak monochromatic circularly polarized laser pulse carrying OAM irradiates the quantum ring and initiates the dynamics of the corresponding charge carriers.

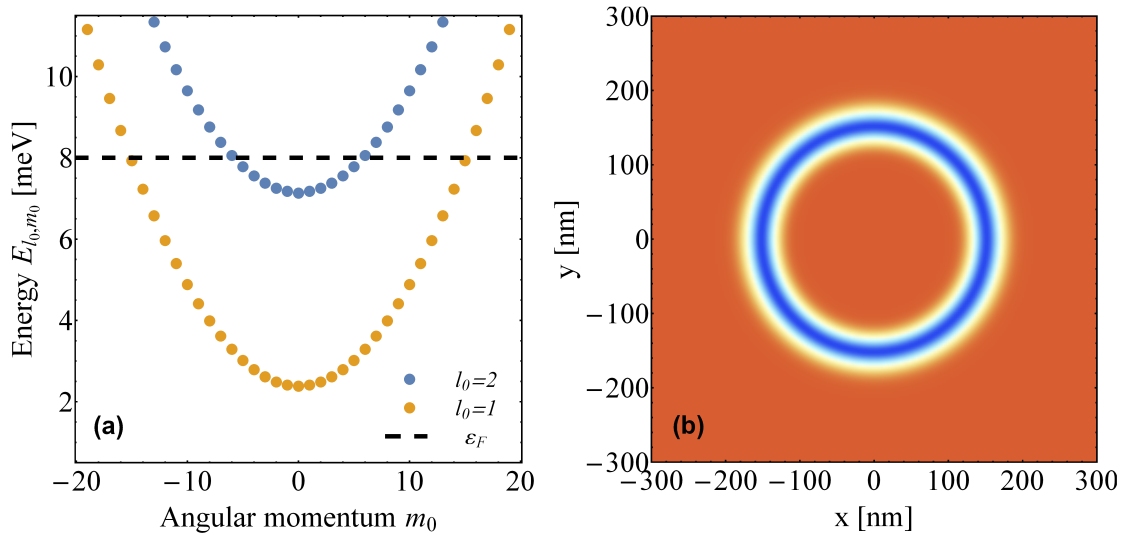


Fig. 2.14 (a) The energy levels E_{l_0, m_0} of the ring structure where the corresponding Fermi energy ϵ_F is marked by the horizontal dashed line. (b) Initial LDOS of the considered 2D-system.

We consider the plane $z = 0$ because no dynamics occur along the propagation direction of vortex beam which is focused vertically on the ring structure. The dynamics is described by the time propagation of the single-particle wave functions $\Psi_{l_0, m_0}(x, y, t)$ corresponding to the individual electron states with the quantum numbers l_0 and m_0 . They can be obtained by solving the time-dependent two-dimensional Schrödinger equation in the presence of the confinement potential $V(x, y)$ and the vector potential $\vec{A}(x, y, t)$ of the optical vortex:

$$i\hbar\partial_t\Psi_{l_0, m_0}(x, y, t) = \left\{ -\frac{\hbar^2}{2m^*}\nabla^2 + \frac{ie\hbar}{2m^*} \left(2\vec{A}(x, y, t) \cdot \vec{\nabla} + \vec{\nabla} \cdot \vec{A}(x, y, t) \right) + \frac{e^2}{2m^*}A^2(x, y, t) + V(x, y) \right\} \Psi_{l_0, m_0}(x, y, t). \quad (2.28)$$

The full numerical solution was performed with the aid of a Runge-Kutta propagation scheme. The considered electron state evolves than from the stationary state at the time $t = 0$ characterized by the quantum numbers l_0 and m_0 . The vector potential of the OAM beam in cylindrical coordinates is further described by Eq. (2.1). Note that because we investigate a 2D system $\rho \equiv r$. We use the simplest form of the LG modes with the radial index $p = 0$ in which case the intensity profile is donut-shaped around $z = 0$. Since the optical axis and the center of the ring coincide, we consider the special case where $r = r'$ and $\varphi' = \varphi = \arctan(x/y)$. The polarization vector of the laser beam is given by $\hat{\epsilon} = \sqrt{1/2}(\vec{e}_x - i\vec{e}_y)$. The moderate peak intensity I_{OAM} is 10^{10} W/cm² while we use a photon energy of $\hbar\omega = 5$ meV. The corresponding wave length is ($\lambda = 247$ μm). The pulse

duration is exactly two optical cycles, i.e. $\tau = 1.65$ ps. For an effective numerical simulation, the total radial intensity profile should not be larger than 200 nm, i.e. we choose a beam waist $w_0 = 55$ nm.

The most important feature is the capability of transferring the orbital angular momentum carried by the optical vortex when interacting with a dielectric particle, i.e. it delivers a torque to charge carriers when absorbing photons [94, 112–116]. Within the paraxial approximation, this total torque can be found by the photon flux multiplied by the total angular momentum of the beam. In our case of LG modes, $(\ell_{\text{OAM}} + \sigma_z)\hbar$ characterizes the total amount of angular momentum where σ_z is the handedness of the circularly polarized OAM light.

2.5.2 Photo-induced charge drift

We consider in the following a topological charge $\ell_{\text{OAM}} = -10$. Together with the helicity $\sigma_z = -1$ due to the polarization state, the total amount of transferrable OAM to the ring is $-11\hbar$. The torque associated with the accompanied change of the OAM of the charge carriers has its origin not only in the vector potential of the optical vortex beam but equally important is the confinement potential $V(x, y)$ that hinders the charge density to escape and must not be overcome. Therefore, we have a system-dependent limitation factor for the used intensity and topological charge ℓ_{OAM} .

In Fig. 2.15(a) we demonstrate the dynamical LDOS at a time $t = 2$ ps, i.e. after the two cycle pulse is off. It can be calculated in the same vein as in Eq. (2.27), i.e. by $\sum_{l_0, m_0} f(l_0, m_0, t) |\Psi_{l_0, m_0}(x, y)|^2$. Here, we introduce the non-equilibrium distribution function $f(l_0, m_0, t)$ which can be evaluated by solving the Boltzmann equation. We used here the relaxation time approximation [157] where the whole class of relaxation processes like electron-phonon scattering, simultaneous scattering by impurities and phonons or electron-electron scattering is condensed phenomenologically in the relaxation time τ_{rel} as single (averaged) quantity. Within this approximation we have to solve the following equation:

$$\frac{\partial f(l_0, m_0, t)}{\partial t} = -\frac{f(l_0, m_0, t) - f^0(l_0, m_0, \varepsilon_F)}{\tau_{\text{rel}}}. \quad (2.29)$$

We emphasize again that we are considering relatively weak, low-energy excitations around the Fermi energy ε_F which legitimizes the approximation. An averaged relaxation time of 25 ps is assumed [156] at a constant Fermi energy. The evolution of the energy of the particle that develops from the initial stationary state l_0, m_0 due to the action of the optical vortex can be obtained by evaluating the time-dependent matrix elements $E_{l_0, m_0}(t) = i\hbar \langle \Psi_{l_0, m_0}(t) | \frac{\partial}{\partial t} | \Psi_{l_0, m_0}(t) \rangle$. On the one hand, these time-dependent energies enter Eq. (2.29) and on the other hand, they reveal the involved electron states.

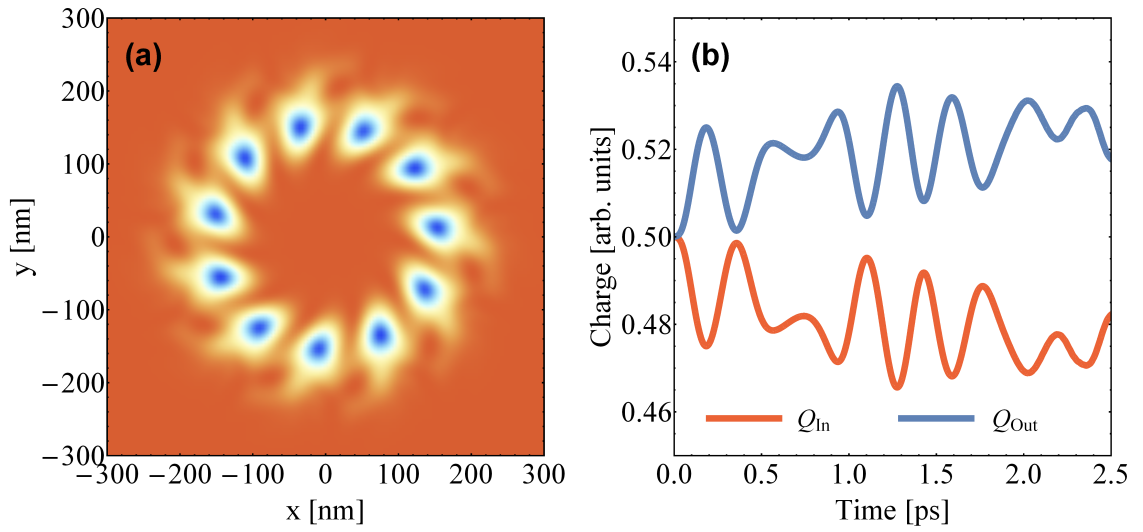


Fig. 2.15 (a) LDOS of the system after a propagation time of $t = 2$ ps. (b) Inner and outer density $Q^{\text{In/Out}}$ of the ring structure in dependence of the propagation time.

From the inspection of the dynamical LDOS after the optical vortex pulse one can conclude that the initial angular symmetry between the states with $m_0 = \pm m$, as well as the radial symmetry with respect to the radius r_0 of the ring are totally broken. This is evidenced by the 11 nodal angular structures which are explainable by the optical selection rules since the total amount of OAM transferred to the charge carriers is $-11\hbar$. As a consequence, the orbital angular momentum is conserved. Furthermore, the shape and the direction of the whirls corresponding to the nodal structures hint the radial accumulation of the charge at the outer ring boundaries and therefore the generation of a charge current loop. This can be easily understood by the enhancement of the effective centrifugal potential due to the abovementioned transfer of OAM. The direction of the whirls can be inverted by changing the sign of the topological charge, as well as, the polarization direction. We checked this relation carefully with a second propagation which is not shown for brevity.

This hinted radial drift of the charge density from the initial equilibrium state to outer radii while the ring structure is irradiated by the OAM beam is evidenced by the time-dependent charge densities in the inner and outer area shown in Fig. 2.15(b). For an individual initial state with the quantum numbers l_0 and m_0 they are given by $Q_{l_0, m_0}^{\text{In}}(t) = \int_0^{2\pi} d\varphi \int_0^{r_0} dr r |\Psi_{l_0, m_0}(r, \varphi)|^2$ for the inner area, and $Q_{l_0, m_0}^{\text{Out}}(t) = \int_0^{2\pi} d\varphi \int_{r_0}^{\infty} dr r |\Psi_{l_0, m_0}(r, \varphi)|^2$ for the outer ring area. In the case of the whole conduction subbands, these quantities are again defined as a weighted sum over all time-dependent contributions from the individual single-particle states. Therefore, they are found as

$$Q^{\text{In/Out}}(t) = \sum_{l_0, m_0} f(l_0, m_0, t) Q_{l_0, m_0}^{\text{In/Out}}(t). \quad (2.30)$$

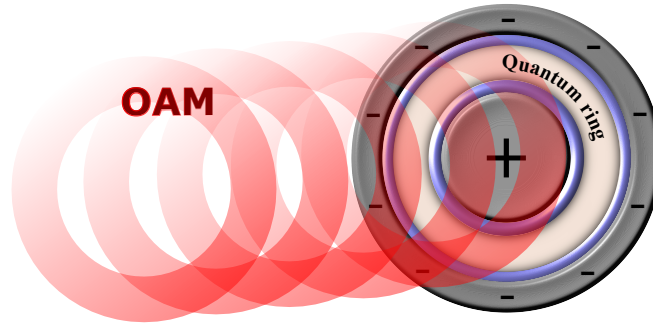


Fig. 2.16 A proposed scheme for an open circuit voltage generation driven by an optical vortex beam. The irradiated ring structure (with a spiral phase plate on the top) is separated by two thin tunneling barriers (blue) from two electrodes which gather the charge carriers.

At a time $t = 0$ when the propagation starts, the initial radial symmetry with respect to r_0 is nicely reflected by both quantities because $Q^{\text{In}}(t = 0) = Q^{\text{Out}}(t = 0)$. This situation changes completely for times when the ring structure is irradiated by the focused optical vortex beam. The light-matter interaction initiates a redistribution of the charge over the course of time (cf. Fig. 2(a)) in a way that the density flows to the outer ring boundary. The explanation is the repulsive centrifugal force which is effectively increased by the accompanied transfer of OAM. Therefore, we have a direct influence on this photovoltaic effect by tuning the topological charge ℓ_{OAM} . As we mentioned above, the only restriction is that the centrifugal potential must not overcome the confinement which would immediately lead to electron emission. Since we are looking at times t well below the relaxation time, the evolution is unitary. Therefore, the frequencies of the oscillations of the time-dependent charge densities $Q^{\text{In/Out}}(t)$ are explained by the frequencies of the photo-induced transitions between levels near the Fermi level ε_F which are governed by the selection rules.

A possible experimental realization of the whole scenario is depicted in Fig. 2.16. An appropriate spiral phase plate is deposited on the quantum ring, and a conventional Gaussian beam irradiates the entire construction. The light wave transverses the plate and is converted into an optical vortex carrying OAM, which is transferred to the charge carriers of the quantum ring. For this purpose, a strong focusing of the light beam on the ring structure is necessary. Indeed, through recent achievements in the development of metamaterial-based lenses [158, 159] such a focusing is realizable and does not prohibit the described photovoltaic effects. The reason is that the topological charge is conserved while such a lens arrangement may modify the spatial profile of the electric field. Therefore, the transfer of the OAM is still possible after the focusing. In the proposed scheme the photo-induced charge imbalance with respect to the ring boundaries which produces a voltage drop is accumulated at the electrodes.

2.5.3 Photovoltaic current generation

In a next step, we want to utilize the observed charge accumulation at the outer boundary of the ring to generate a directed current. Therefore, we wire the ring to a conductive straight channel at one of the sides (cf. Fig.2.17(a)). The system is arranged in a way that the optical vortex does not irradiate the conducting bar, i.e. the light is focused solely on the ring structure. The whole initial situation is shown in Fig.2.17(b). Therefore, the wire is unaffected by the action of the vortex beam. As a consequence, the initial radially symmetric confinement potential $V(x,y)$ has to be modified drastically. From an experimental point of view, such a specific potential landscape has already been fabricated and could be modified as required by appropriate gating [160, 161]. The ring structure and the wire are constructed of the same material and have the same chemical potential. The confinement potential $V(x,y)$ which enters the Schrödinger equation in Eq.(2.28) has to be changed in a way that the charge carriers populate the ring and the conducting bar equally.

The technical modifications of the potential are described in the following: The average ring radius r_0 is still 150 nm, i.e. $V(x,y)$ is characterized for $x \leq 200$ nm by [152]. At $x = 200$ nm we attach a 100 nm wide conducting wire, i.e. $V(x > 200 \text{ nm}, y) = 0$. The effective tunneling barrier region between the quantum ring and the conduction bar is around 25 nm wide since we consider an effective width of the ring $\Delta r = 50$ nm. As a consequence of the modification, the potential $V(x,y)$ has no radial symmetry anymore. Therefore, we have to change the characterization of the single particle states and will describe them henceforth by the quantum numbers n with the energy E_n . The calculation of these state in the equilibrium shows that the shape of the LDOS in the ring region, i.e. $\sum_n f^0(n) |\Psi_n(x < 200 \text{ nm}, y, t = 0)|^2$, is not significantly different in comparison to the case without the wire (cf. Fig. 2.17(b)).

In Fig. 2.17(a) the effect of the new potential landscape is demonstrated nicely. We show here the LDOS at a propagation time of 2.4 ps, i.e. the OAM pulse is off. The action of the optical vortex, which interacts solely with the quantum ring, affects the corresponding charge density in a way that a charge imbalance with respect to the ring boundaries is produced. Furthermore, it acquires a twisted which can be identified by the direction of the whirls of the nodal structures. Due to the small thickness, the charge carriers tunnel through the barrier region to the conducting bar where they crash on the outer boundary at $x = 300$ nm. The subtle interference pattern which is formed by the reflected and the incoming waves emphasizes this process. The whole density distribution is now completely asymmetric with respect to the center of the ring and therefore current carrying. The direction of the flux reflects the direction of the whirls of the nodal structures. In our case, the incoming charge density flows mainly in the negative y -direction which can be tuned by the sign of the topological charge ℓ_{OAM} . We carefully checked this symmetric behavior by

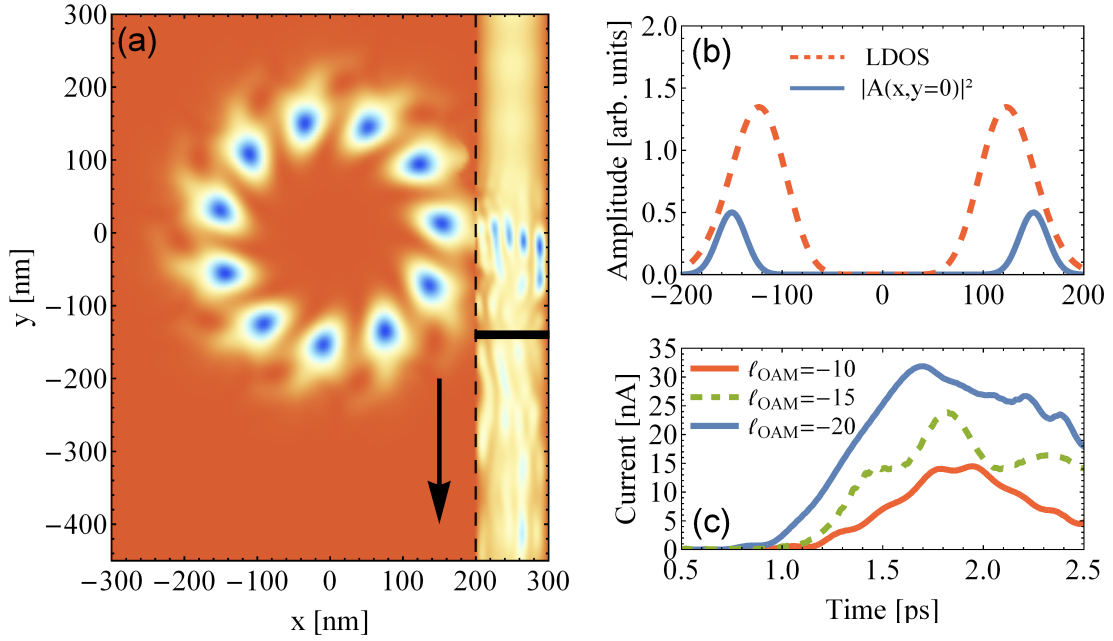


Fig. 2.17 (a) The LDOS of the ring structure which is connected with a conducting bar after a propagation time of $t = 2.4$ ps, i.e. after the optical vortex pulse is off. The thick horizontal line at $y_d = -140$ nm marks a detector to record the photo-induced current whose direction is shown by the arrow. The vertical dashed lines indicate the wire potential boundaries. (b) The initial ring LDOS together with the OAM beam intensity profile. The wire is not affected by the optical vortex beam. (c) Time-dependent total currents (cf. (2.33)) through the detector for different topological charges ℓ_{OAM} .

adjusting the parameters, i.e. that a change of the polarization direction and the sign of the topological charge leads to a positively directed flow of density of the same magnitude.

In addition to the dynamical change of LDOS, one should record the current flow within the wire to quantify this photovoltaic effect. Therefore, a detector is positioned in the conducting bar far enough from the irradiated ring structure at $y_d = -140$ nm. The time-dependent flux of the charge carrier density associated with the photo-induced dynamics of a single particle state characterized by quantum number n can be obtained by calculating the corresponding time-dependent probability current density in the y -direction as

$$j_n^y(x, y, t) = -\frac{1}{m^*} \text{Re} \left\{ \Psi_n^*(x, y, t) [i\hbar \partial_y + eA_y(x, y, t)] \Psi_n(x, y, t) \right\}. \quad (2.31)$$

The time-dependent current of the specified single-particle state which flows through the detector is then evaluated by

$$I_n(t) = \int_{x_1}^{x_2} dx j_n^y(x, y_d, t), \quad (2.32)$$

where the bounds of the integration are the borders of the wire at $x_1 = 200$ nm and $x_2 = 300$ nm. The detector is marked by the black horizontal line in Fig. 2.17(a). The total photovoltaic current is the weighted sum over all partial current contributions $I_n(t)$ generated by the individual particles which are classified by the quantum numbers n . It can be calculated by

$$I(t) = \sum_n f(n,t)I_n(t), \quad (2.33)$$

where $f(n,t)$ is the abovementioned non-equilibrium distribution function which can be evaluated according to Eq. (2.29).

In Fig. 2.17(c) we show the time dependence of the total current for different topological charges explicitly. The several curves reveal the general trend that a higher topological charge $|\ell_{\text{OAM}}|$ leads to a higher current. Therefore, the photovoltaic effect which is accompanied by the enlarged centrifugal force can be increased by considering a larger winding number of the vortex beam. By comparing the results depicted in Fig. 2.17(c) with the charge densities $Q^{\text{In/Out}}(t)$ in Fig. 2.15(b) it becomes evident that the voltage drop due to the charge accumulation at the ring boundaries does not build up immediately as the optical vortex starts to interact with the ring structure. This inertia is related to the finite effective mass of the carriers. Therefore, the current in the wire is generated later in a "transport" time which is characterized by the effective velocities of the various current carrying states which are heavily influenced by the permanent tunneling, rescattering and interfering processes. The "transport" time can be tuned by increasing the frequency ω or using a higher topological charge. This behaviour is emphasized by the time-dependent total currents for $\ell_{\text{OAM}} = -15$ and $\ell_{\text{OAM}} = -20$. It is clearly evident that the currents merge faster in the attached wire for larger $|\ell_{\text{OAM}}|$. The small oscillations of the time-dependent currents in the wire can be easily explained by the related oscillations of the charge densities $Q^{\text{In/Out}}(t)$ in Fig. 2.15(a). A maximum of the currents can be found for times around $t = 1.7$ ps which is the moment where the laser pulse is turned off. Henceforth, the recorded currents decrease rapidly in time due to the weakening flux of the charge density out of the ring.

The underlying effect can be extended to a waterwheel-like mechanism by attaching a second wire on the other side of the ring structure which optimizes the photo-induced current generation. Such a scenario is depicted in Fig. 2.18(a) where we used the same pulse parameters as mentioned above and a topological charge $\ell_{\text{OAM}} = -10$. The LDOS reveals two currents of the same magnitude flowing in opposite directions which can be controlled by the considered topological charge ℓ_{OAM} . The wires can now be connected to produce a larger useable total current generated by the ring structure. Another possibility to enhance the photo-induced current effectively is the fabrication of several and well-defined ring structures which will be attached in series to a conducting bar. On each of the rings, an appropriate spiral phase plate is deposited which generates locally an optical vortex from an

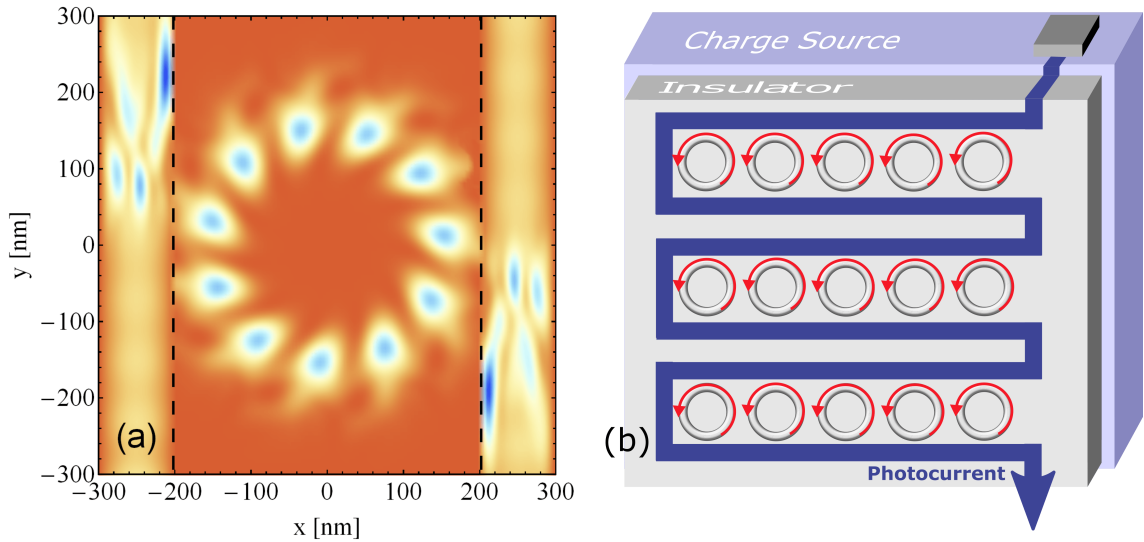


Fig. 2.18 (a) LDOS of the ring structure which is attached to two conducting bars. The considered topological charge $\ell_{\text{OAM}} = -10$ and the propagation time is $t = 1.3$ ps, i.e. the applied OAM pulse is still on. The used parameters are the same as in the simulation shown in Fig.(2.17). (b) A schematic device for generating a photo-induced current based on the mechanism described in the text. On each of the quantum ring structures, a spiral phase plate is placed that produces an optical vortex (indicated by the red arrows) from an incoming unstructured light wave. The subsequent interaction with the charge carriers leads to a directed current in the wires which is enhanced with every additional ring in the device.

conventional Gaussian beam. Therefore, each ring will be irradiated by an individual OAM pulse and delivers a contribution to the total current.

Both possibilities to enhance the photo-induced current, i.e. on the one hand by clamping the rings between two wires and on the other hand by attaching them in series to the conducting bar, can be condensed to an effective scheme for the current generation which is shown in Fig. 2.18(b). From the considerations above, it is clear that we can steer and enhance this photo-induced current at will both in direction and magnitude by tuning the topological charge ℓ_{OAM} and placing or removing quantum rings from the device.

2.5.4 Conclusion

We demonstrated a photovoltaic effect by irradiating a quantum ring structure with a focused laser pulse carrying orbital angular momentum. With the aid of a full-fledged quantum dynamical simulation on the basis of the single-particle picture, we showed that the light-matter interaction caused a radial drift of the charge carriers which is accompanied by a charge accumulation at the outer ring boundary. The explanation is the effective enhancement of the effective repulsive centrifugal potential due to the transfer of orbital angular momentum to the ring. The corresponding photo-induced voltage drop between the inner and outer boundaries can be utilized to generate a directed photocurrent by attaching

a conductive bar to the structure. Therefore, the accumulated charge density at the outer ring boundary tunnels through a thin barrier region into the wire. The directed flow of the OAM-driven photocurrent, as well as, the magnitude could be tuned by changing the topological charge at a fixed intensity and frequency. A possible experimental realization was proposed and demonstrated where this photovoltaic effect can be steered and controlled effectively.

Summary

The major goal of this thesis was the demonstration of fascinating effects brought about by the optical vortex light.

The first chapter of this thesis dealt with the angular dependence of the time delay and revealed the large impact of the description of the electronic structure on the accuracy of the calculations. While the investigation based on the usage of a conventional laser beam, one aspect of the second chapter were the new features in the time delay in photoionization which are introduced by applying an optical vortex pulse. Our results showed that a new class of photo-induced non-dipolar transitions has a significant impact on the time delay which reveals a strong dependence on the initial magnetic substate within the considered subshell even from spherically symmetric targets. Furthermore, it depends very strongly on the position of the target within the vortex beam. Thus, time delay measurements allow the accessing of magnetic information with an atomic size spatial resolution.

In another part of this thesis, we showed how a useable magnetic pulse could be generated by irradiating a C_{60} with an optical vortex pulse. The effective transfer of orbital angular momentum to the molecule initiated non-dipolar transitions from the occupied π -band to the super atomic molecular orbitals which generate a current loop on the sphere. The optical selection rules could be extracted by contrasting with the corresponding frequency-dependent photo-induced magnetic moment spectra. We found a smooth dependence of the molecule's position relative to optical vortex beam, i.e. even for a dilute gas phase of randomly distributed fullerenes a distinctive magnetic field could be generated which is effectively tuneable by the parameters of the used optical vortex beam. The strong dependence on the underlying electronic structure and the considered topological charge endorses that the observable effect could be enlarged by considering larger objects with highly degenerate SAMOs. The vast potential for this proposed photo-induced magnetic pulse generation in matter is underlined by the fact that SAMOs seem to exist [133–140, 162] for large molecular structures, as well as, very high topological charges up to 300 are realizable [18–24, 91]. These results point to an innovative way of ultrafast optical manipulation and steering of magnetically active endohedrals because the generated magnetic pulse Zeeman-couples to the well-isolated spin active states associated with the carbon cage structure.

As the last example, we investigated the capability of an optical vortex laser pulse to generate a directed and useable current. Indeed, we demonstrated on the basis of a full numerical simulation that a directed flux of charge density could be produced in a conductive straight channel while an attached irradiated quantum ring acts as a charge reservoir. This effect can be explained intuitively by the effective enhancement of the repulsive centrifugal force due to the transfer of the orbital momentum to the ring. Subsequently, the charge will be pressed to the outer ring boundary and splashes into the attached wire generating so a directed flux. This photovoltaic mechanism could be optimized by clamping the ring structure between two conducting bars which produced two photocurrents in opposite directions. We proposed schematically a device where several ring structures produce a highly controllable photo-induced current. Groundbreaking is the observation that the photovoltaic effect could be enhanced by solely increasing the topological charge of the optical vortex beam while the frequency and the moderate intensity remain fixed. The promising potential of this proposed photovoltaic effect is emphasized by the possibility to generate optical vortex pulses with a topological charge up to 300. The limitation factor of a strong confinement potential of the quantum ring is achievable by appropriate nanostructuring.

References

- [1] E. P. Wigner, “Lower limit for the energy derivative of the scattering phase shift,” *Physical Review*, vol. 98, no. 1, p. 145, 1955.
- [2] F. T. Smith, “Lifetime matrix in collision theory,” *Physical Review*, vol. 118, no. 1, p. 349, 1960.
- [3] M. Schultze, M. Fieß, N. Karpowicz, J. Gagnon, M. Korbman, M. Hofstetter, S. Neppl, A. L. Cavalieri, Y. Komninos, T. Mercouris, *et al.*, “Delay in photoemission,” *Science*, vol. 328, no. 5986, pp. 1658–1662, 2010.
- [4] K. Klünder, J. Dahlström, M. Gisselbrecht, T. Fordell, M. Swoboda, D. Guénot, P. Johnsson, J. Caillat, J. Mauritsson, A. Maquet, *et al.*, “Probing single-photon ionization on the attosecond time scale,” *Physical Review Letters*, vol. 106, no. 14, p. 143002, 2011.
- [5] D. Guénot, K. Klünder, C. Arnold, D. Kroon, J. Dahlström, M. Miranda, T. Fordell, M. Gisselbrecht, P. Johnsson, J. Mauritsson, *et al.*, “Photoemission-time-delay measurements and calculations close to the 3 s-ionization-cross-section minimum in ar,” *Physical Review A*, vol. 85, no. 5, p. 053424, 2012.
- [6] A. L. Cavalieri, N. Müller, T. Uphues, V. S. Yakovlev, A. Baltuška, B. Horvath, B. Schmidt, L. Blümel, R. Holzwarth, S. Hendel, *et al.*, “Attosecond spectroscopy in condensed matter,” *Nature*, vol. 449, no. 7165, pp. 1029–1032, 2007.
- [7] S. Nagele, R. Pazourek, J. Feist, K. Doblhoff-Dier, C. Lemell, K. Tókési, and J. Burgdörfer, “Time-resolved photoemission by attosecond streaking: extraction of time information,” *Journal of Physics B: Atomic, Molecular and Optical Physics*, vol. 44, no. 8, p. 081001, 2011.
- [8] S. Nagele, R. Pazourek, J. Feist, and J. Burgdörfer, “Time shifts in photoemission from a fully correlated two-electron model system,” *Physical Review A*, vol. 85, no. 3, p. 033401, 2012.
- [9] R. Pazourek, S. Nagele, and J. Burgdörfer, “Time-resolved photoemission on the attosecond scale: opportunities and challenges,” *Faraday Discussions*, vol. 163, pp. 353–376, 2013.
- [10] S. Nagele, R. Pazourek, M. Wais, G. Wachter, and J. Burgdörfer, “Time-resolved photoemission using attosecond streaking,” in *Journal of Physics: Conference Series*, vol. 488, p. 012004, 2014.
- [11] J. Feist, O. Zatsarinny, S. Nagele, R. Pazourek, J. Burgdörfer, X. Guan, K. Bartschat, and B. I. Schneider, “Time delays for attosecond streaking in photoionization of neon,” *Physical Review A*, vol. 89, no. 3, p. 033417, 2014.

- [12] A. Kheifets and I. Ivanov, “Delay in atomic photoionization,” *Physical Review Letters*, vol. 105, no. 23, p. 233002, 2010.
- [13] L. Moore, M. Lysaght, J. Parker, H. Van Der Hart, and K. Taylor, “Time delay between photoemission from the 2 p and 2 s subshells of neon,” *Physical Review A*, vol. 84, no. 6, p. 061404, 2011.
- [14] J. Dahlström, A. L’Huillier, and A. Maquet, “Introduction to attosecond delays in photoionization,” *Journal of Physics B: Atomic, Molecular and Optical Physics*, vol. 45, no. 18, p. 183001, 2012.
- [15] J. M. Dahlström, D. Guénot, K. Klünder, M. Gisselbrecht, J. Mauritsson, A. L’Huillier, A. Maquet, and R. Taïeb, “Theory of attosecond delays in laser-assisted photoionization,” *Chemical Physics*, vol. 414, pp. 53–64, 2013.
- [16] A. Kheifets, “Time delay in valence-shell photoionization of noble-gas atoms,” *Physical Review A*, vol. 87, no. 6, p. 063404, 2013.
- [17] J. M. Dahlström and E. Lindroth, “Study of attosecond delays using perturbation diagrams and exterior complex scaling,” *Journal of Physics B: Atomic, Molecular and Optical Physics*, vol. 47, no. 12, p. 124012, 2014.
- [18] L. Allen, M. W. Beijersbergen, R. J. C. Spreeuw, and J. P. Woerdman, “Orbital angular momentum of light and the transformation of laguerre-gaussian laser modes,” *Physical Review A*, vol. 45, pp. 8185–8189, 1992.
- [19] M. Beijersbergen, L. Allen, H. van der Veen, and J. Woerdman, “Astigmatic laser mode converters and transfer of orbital angular momentum,” *Optics Communications*, vol. 96, no. 1–3, pp. 123 – 132, 1993.
- [20] M. Beijersbergen, R. Coerwinkel, M. Kristensen, and J. Woerdman, “Helical-wavefront laser beams produced with a spiral phaseplate,” *Optics Communications*, vol. 112, no. 5, pp. 321–327, 1994.
- [21] H. He, M. Friese, N. Heckenberg, and H. Rubinsztein-Dunlop, “Direct observation of transfer of angular momentum to absorptive particles from a laser beam with a phase singularity,” *Physical Review Letters*, vol. 75, no. 5, p. 826, 1995.
- [22] N. Simpson, K. Dholakia, L. Allen, and M. Padgett, “Mechanical equivalence of spin and orbital angular momentum of light: an optical spanner,” *Optics Letters*, vol. 22, no. 1, pp. 52–54, 1997.
- [23] M. Soskin, V. Gorshkov, M. Vasnetsov, J. Malos, and N. Heckenberg, “Topological charge and angular momentum of light beams carrying optical vortices,” *Physical Review A*, vol. 56, no. 5, p. 4064, 1997.
- [24] G. Molina-Terriza, J. P. Torres, and L. Torner, “Twisted photons,” *Nature Physics*, vol. 3, pp. 305–310, 2007.
- [25] A. Mair, A. Vaziri, G. Weihs, and A. Zeilinger, “Entanglement of the orbital angular momentum states of photons,” *Nature*, vol. 412, no. 6844, pp. 313–316, 2001.
- [26] J. T. Barreiro, T.-C. Wei, and P. G. Kwiat, “Beating the channel capacity limit for linear photonic superdense coding,” *Nature Physics*, vol. 4, no. 4, pp. 282–286, 2008.

- [27] R. W. Boyd, A. Jha, M. Malik, C. O'Sullivan, B. Rodenburg, and D. J. Gauthier, "Quantum key distribution in a high-dimensional state space: exploiting the transverse degree of freedom of the photon," in *SPIE OPTO*, pp. 79480L–79480L, International Society for Optics and Photonics, 2011.
- [28] M. Padgett and R. Bowman, "Tweezers with a twist," *Nature Photonics*, vol. 5, no. 6, pp. 343–348, 2011.
- [29] S. Fürhapter, A. Jesacher, S. Bernet, and M. Ritsch-Marte, "Spiral interferometry," *Optics Letters*, vol. 30, no. 15, pp. 1953–1955, 2005.
- [30] M. Woerdemann, C. Alpmann, and C. Denz, "Self-pumped phase conjugation of light beams carrying orbital angular momentum," *Optics Express*, vol. 17, no. 25, pp. 22791–22799, 2009.
- [31] J. P. Torres and L. Torner, *Twisted Photons: Applications of Light with Orbital Angular Momentum*. Wiley-VCH, Weinheim, 2011.
- [32] D. L. Andrews, *Structured light and its applications: An introduction to phase-structured beams and nanoscale optical forces*. Academic Press, 2011.
- [33] G. Foo, D. M. Palacios, G. A. Swartzlander Jr, *et al.*, "Optical vortex coronagraph," *Optics Letters*, vol. 30, no. 24, pp. 3308–3310, 2005.
- [34] H. He, N. Heckenberg, and H. Rubinsztein-Dunlop, "Optical particle trapping with higher-order doughnut beams produced using high efficiency computer generated holograms," *Journal of Modern Optics*, vol. 42, no. 1, pp. 217–223, 1995.
- [35] H. Wang, L. Shi, B. Lukyanchuk, C. Sheppard, and C. T. Chong, "Creation of a needle of longitudinally polarized light in vacuum using binary optics," *Nature Photonics*, vol. 2, no. 8, pp. 501–505, 2008.
- [36] S. W. Hell, "Far-field optical nanoscopy," *Science*, vol. 316, no. 5828, pp. 1153–1158, 2007.
- [37] P. Agostini and L. F. DiMauro, "The physics of attosecond light pulses," *Reports on Progress in Physics*, vol. 67, no. 6, p. 813, 2004.
- [38] M. F. Kling and M. J. Vrakking, "Attosecond electron dynamics," *Annual Review of Physical Chemistry*, vol. 59, pp. 463–492, 2008.
- [39] F. Krausz and M. Ivanov, "Attosecond physics," *Reviews of Modern Physics*, vol. 81, no. 1, p. 163, 2009.
- [40] M. Y. Amusia, *Atomic Photoeffect*. New York: Plenum, 1990.
- [41] M. Drescher, M. Hentschel, R. Kienberger, G. Tempea, C. Spielmann, G. A. Reider, P. B. Corkum, and F. Krausz, "X-ray pulses approaching the attosecond frontier," *Science*, vol. 291, no. 5510, pp. 1923–1927, 2001.
- [42] J. Itatani, F. Quéré, G. L. Yudin, M. Y. Ivanov, F. Krausz, and P. B. Corkum, "Attosecond streak camera," *Physical Review Letters*, vol. 88, no. 17, p. 173903, 2002.
- [43] F. Quéré, Y. Mairesse, and J. Itatani, "Temporal characterization of attosecond xuv fields," *Journal of Modern Optics*, vol. 52, no. 2-3, pp. 339–360, 2005.

- [44] G. Sansone, E. Benedetti, F. Calegari, C. Vozzi, L. Avaldi, R. Flammini, L. Poletto, P. Villoresi, C. Altucci, R. Velotta, *et al.*, “Isolated single-cycle attosecond pulses,” *Science*, vol. 314, no. 5798, pp. 443–446, 2006.
- [45] V. S. Yakovlev, F. Bammer, and A. Scrinzi, “Attosecond streaking measurements,” *Journal of Modern Optics*, vol. 52, no. 2-3, pp. 395–410, 2005.
- [46] V. S. Yakovlev, J. Gagnon, N. Karpowicz, and F. Krausz, “Attosecond streaking enables the measurement of quantum phase,” *Physical Review Letters*, vol. 105, no. 7, p. 073001, 2010.
- [47] M. Drescher, M. Hentschel, R. Kienberger, M. Uiberacker, V. Yakovlev, A. Scrinzi, T. Westerwalbesloh, U. Kleineberg, U. Heinzmann, and F. Krausz, “Time-resolved atomic inner-shell spectroscopy,” *Nature*, vol. 419, no. 6909, pp. 803–807, 2002.
- [48] E. Goulielmakis, M. Uiberacker, R. Kienberger, A. Baltuska, V. Yakovlev, A. Scrinzi, T. Westerwalbesloh, U. Kleineberg, U. Heinzmann, M. Drescher, *et al.*, “Direct measurement of light waves,” *Science*, vol. 305, no. 5688, pp. 1267–1269, 2004.
- [49] N. M. Kroll and K. M. Watson, “Charged-particle scattering in the presence of a strong electromagnetic wave,” *Physical Review A*, vol. 8, no. 2, p. 804, 1973.
- [50] A. Maquet and R. Taïeb, “Two-colour ir+ xuv spectroscopies: the “soft-photon approximation”,” *Journal of Modern Optics*, vol. 54, no. 13-15, pp. 1847–1857, 2007.
- [51] Á. J. Galán, L. Argenti, and F. Martín, “The soft-photon approximation in infrared-laser-assisted atomic ionization by extreme-ultraviolet attosecond-pulse trains,” *New Journal of Physics*, vol. 15, no. 11, p. 113009, 2013.
- [52] I. Ivanov and A. Kheifets, “Extraction of the attosecond time delay in atomic photoionization using the soft-photon approximation,” *Physical Review A*, vol. 87, no. 6, p. 063419, 2013.
- [53] G. Duchateau, E. Cormier, and R. Gayet, “Coulomb-volkov approach of ionization by extreme-ultraviolet laser pulses in the subfemtosecond regime,” *Physical Review A*, vol. 66, no. 2, p. 023412, 2002.
- [54] A. Kornev and B. Zon, “Testing of coulomb-volkov functions,” *Journal of Physics B: Atomic, Molecular and Optical Physics*, vol. 35, no. 11, p. 2451, 2002.
- [55] C. A. de Carvalho and H. M. Nussenzveig, “Time delay,” *Physics Reports*, vol. 364, no. 2, pp. 83–174, 2002.
- [56] J. M. Dahlström, T. Carette, and E. Lindroth, “Diagrammatic approach to attosecond delays in photoionization,” *Physical Review A*, vol. 86, no. 6, p. 061402, 2012.
- [57] T. Carette, J. Dahlström, L. Argenti, and E. Lindroth, “Multiconfigurational hartree-fock close-coupling ansatz: Application to the argon photoionization cross section and delays,” *Physical Review A*, vol. 87, no. 2, p. 023420, 2013.
- [58] L. Eisenbud, *Formal properties of nuclear collisions*. dissertation, Princeton University, 1948.
- [59] J. W. Cooper, “Photoionization from outer atomic subshells. a model study,” *Physical Review*, vol. 128, no. 2, p. 681, 1962.

- [60] G. Dixit, H. S. Chakraborty, and M. E.-A. Madjet, “Time delay in the recoiling valence photoemission of an endohedrally confined in C_{60} ,” *Physical Review Letters*, vol. 111, no. 20, p. 203003, 2013.
- [61] M. Magrakvelidze, M. E.-A. Madjet, G. Dixit, M. Ivanov, and H. S. Chakraborty, “Attosecond time delay in valence photoionization and photorecombination of argon: A time-dependent local-density-approximation study,” *Physical Review A*, vol. 91, no. 6, p. 063415, 2015.
- [62] I. Ivanov, “Time delay in strong-field photoionization of a hydrogen atom,” *Physical Review A*, vol. 83, no. 2, p. 023421, 2011.
- [63] I. Ivanov, A. Kheifets, and V. V. Serov, “Attosecond time-delay spectroscopy of the hydrogen molecule,” *Physical Review A*, vol. 86, no. 6, p. 063422, 2012.
- [64] V. V. Serov, V. L. Derbov, and T. A. Sergeeva, “Interpretation of time delay in the ionization of two-center systems,” *Physical Review A*, vol. 87, no. 6, p. 063414, 2013.
- [65] S. Heuser, Á. Jiménez-Gálán, C. Cirelli, M. Sabbar, R. Boge, M. Lucchini, L. Gallmann, I. Ivanov, A. Kheifets, J. Dahlström, *et al.*, “Time delay anisotropy in photoelectron emission from isotropic helium,” *Journal of Physics: Conference Series*, vol. 635, no. 9, p. 092089, 2015.
- [66] C. Palatchi, J. M. Dahlström, A. Kheifets, I. Ivanov, D. Canaday, P. Agostini, and L. DiMauro, “Atomic delay in helium, neon, argon and krypton,” *Journal of Physics B: Atomic, Molecular and Optical Physics*, vol. 47, no. 24, p. 245003, 2014.
- [67] W. Pauli, “Die allgemeinen Prinzipien der Wellenmechanik,” *Handbuch der Physik*, vol. 24, p. 83–272, 1933.
- [68] C. J. Joachain, *Quantum collision theory*. New York: North Holland, 1975.
- [69] F. Gesztesy, “On the structure of coulomb-type scattering amplitudes,” *Journal of Mathematical Physics*, vol. 23, no. 1, pp. 74–82, 1982.
- [70] D. Bollé, F. Gesztesy, and H. Grosse, “Time delay for long-range interactions,” *Journal of Mathematical Physics*, vol. 24, no. 6, pp. 1529–1541, 1983.
- [71] M. V. Fedorov, *Atomic and free electrons in a strong light field*, vol. 452. World Scientific, 1997.
- [72] M. Seaton, “Quantum defect theory,” *Reports on Progress in Physics*, vol. 46, no. 2, p. 167, 1983.
- [73] L. Rosenberg, “Levinson-seaton theorem for potentials with an attractive coulomb tail,” *Physical Review A*, vol. 52, no. 5, p. 3824, 1995.
- [74] R. G. Newton, *Scattering theory of waves and particles*. Springer Science & Business Media, 2013.
- [75] M. Y. Amusia and L. V. Chernysheva, *Computation of atomic processes: a handbook for the ATOM programs*. Institute of physics, 1997.
- [76] D. A. Varshalovich, A. Moskalev, and V. Khersonskii, *Quantum theory of angular momentum*. World Scientific, 1988.

- [77] E. Cormier and P. Lambropoulos, “Optimal gauge and gauge invariance in non-perturbative time-dependent calculation of above-threshold ionization,” *Journal of Physics B: Atomic, Molecular and Optical Physics*, vol. 29, no. 9, p. 1667, 1996.
- [78] M. Nurhuda and F. H. Faisal, “Numerical solution of time-dependent schrödinger equation for multiphoton processes: A matrix iterative method,” *Physical Review A*, vol. 60, no. 4, p. 3125, 1999.
- [79] A. N. Grum-Grzhimailo, B. Abeln, K. Bartschat, D. Weflen, and T. Urness, “Ionization of atomic hydrogen in strong infrared laser fields,” *Physical Review A*, vol. 81, no. 4, p. 043408, 2010.
- [80] I. Ivanov and A. Kheifets, “Time delay in atomic photoionization with circularly polarized light,” *Physical Review A*, vol. 87, no. 3, p. 033407, 2013.
- [81] A. Goldberg, H. M. Schey, and J. L. Schwartz, “Computer-generated motion pictures of one-dimensional quantum-mechanical transmission and reflection phenomena,” *American Journal of Physics*, vol. 35, no. 3, 1967.
- [82] W. H. Press, *Numerical recipes 3rd edition: The art of scientific computing*. Cambridge university press, 2007.
- [83] A. Kramida, Y. Ralchenko, and J. Reader, “Nist atomic spectra database (ver. 5.1). national institute of standards and technology, gaithersburg, md,” URL: <http://physics.nist.gov/asd>, 2013.
- [84] L. Chernysheva, N. Cherepkov, and V. Radojević, “Self-consistent field hartree-fock program for atoms,” *Computer Physics Communications*, vol. 11, no. 1, pp. 57–73, 1976.
- [85] L. Chernysheva, N. Cherepkov, and V. Radojević, “Frozen core hartree-fock program for atomic discrete and continuous states,” *Computer Physics Communications*, vol. 18, no. 1, pp. 87–100, 1979.
- [86] U. Fano, “Propensity rules: An analytical approach,” *Physical Review A*, vol. 32, no. 1, p. 617, 1985.
- [87] K. Codling, R. Houlgate, J. West, and P. Woodruff, “Angular distribution and photoionization measurements on the 2p and 2s electrons in neon,” *Journal of Physics B: Atomic and Molecular Physics*, vol. 9, no. 5, p. L83, 1976.
- [88] S. T. Manson and A. F. Starace, “Photoelectron angular distributions: energy dependence for s subshells,” *Reviews of Modern Physics*, vol. 54, no. 2, p. 389, 1982.
- [89] U. Fano and J. Cooper, “Spectral distribution of atomic oscillator strengths,” *Reviews of Modern Physics*, vol. 40, no. 3, p. 441, 1968.
- [90] S. Schoun, R. Chirla, J. Wheeler, C. Roedig, P. Agostini, L. DiMauro, K. Schafer, and M. Gaarde, “Attosecond pulse shaping around a cooper minimum,” *Physical Review Letters*, vol. 112, no. 15, p. 153001, 2014.
- [91] L. Allen, S. M. Barnett, and M. Padgett, *Optical Angular Momentum*. Institute of Physics Publishing, Bristol, 2003.
- [92] L. Allen, “Introduction to the atoms and angular momentum of light special issue,” *Journal of Optics B: Quantum and Semiclassical Optics*, vol. 4, no. 2, p. S1, 2002.

- [93] S. Barreiro and J. Tabosa, "Generation of light carrying orbital angular momentum via induced coherence grating in cold atoms," *Physical Review Letters*, vol. 90, p. 133001, Mar 2003.
- [94] M. E. J. Friese, T. A. Nieminen, N. R. Heckenberg, and H. Rubinsztein-Dunlop, "Optical alignment and spinning of laser-trapped microscopic particles," *Nature*, vol. 394, p. 348, 1998.
- [95] L. C. D. Romero, D. L. Andrews, and M. Babiker, "A quantum electrodynamics framework for the nonlinear optics of twisted beams," *Journal of Optics B: Quantum and Semiclassical Optics*, vol. 4, no. 2, p. S66, 2002.
- [96] S. Al-Awfi and M. Babiker, "Atomic motion in hollow submicron circular cylinders," *Physical Review A*, vol. 61, p. 033401, Feb 2000.
- [97] F. Araoka, T. Verbiest, K. Clays, and A. Persoons, "Interactions of twisted light with chiral molecules: An experimental investigation," *Physical Review A*, vol. 71, p. 055401, May 2005.
- [98] K. Helmerson and W. D. Phillips, "Rotating atoms with light," in *Twisted Photons: Applications of Light with Orbital Angular Momentum* (J. JTorres and L. Torner, eds.), pp. 215–220, WILEY-VCH, Weinheim, 2011.
- [99] G. F. Quinteiro and J. Berakdar, "Electric currents induced by twisted light in quantum rings," *Optics Express*, vol. 17, pp. 20465–20475, Oct 2009.
- [100] G. Quinteiro, P. Tamborenea, and J. Berakdar, "Orbital and spin dynamics of intra-band electrons in quantum rings driven by twisted light," *Optics Express*, vol. 19, no. 27, pp. 26733–26741, 2011.
- [101] J. Wätzel, A. S. Moskalenko, and J. Berakdar, "Photovoltaic effect of light carrying orbital angular momentum on a semiconducting stripe," *Optics Express*, vol. 20, pp. 27792–27799, 2012.
- [102] N. R. Heckenberg, R. McDuff, C. P. Smith, H. Rubinsztein-Dunlop, and M. J. Wegener, "Laser beams with phase singularities," *Optical and Quantum Electronics*, vol. 24, pp. 951–962, 1992.
- [103] S. A. Kennedy, M. J. Szabo, H. Teslow, J. Z. Porterfield, and E. R. I. Abraham, "Creation of laguerre-gaussian laser modes using diffractive optics," *Physical Review A*, vol. 66, p. 043801, 2002.
- [104] A. V. Carpentier, H. Michinel, J. R. Salgueiro, and D. Olivieri, "Making optical vortices with computer-generated holograms," *American Journal of Physics*, vol. 76, no. 10, pp. 916–921, 2008.
- [105] J. Curtis and D. Grier, "Structure of optical vortices," *Physical Review Letters*, vol. 90, p. 133901, Apr 2003.
- [106] A. S. Ostrovsky, C. Rickenstorff-Parrao, and V. Arrizón, "Generation of the 'perfect' optical vortex using a liquid-crystal spatial light modulator," *Optics Letters*, vol. 38, pp. 534–536, Feb 2013.
- [107] M. W. Beijersbergen, R. P. C. Coerwinkel, M. Kristensen, and J. P. Woerdman, "Helical-wavefront laser beams produced with a spiral phaseplate," *Optics Communications*, vol. 112, pp. 321–327, 1994.

- [108] L. Marrucci, C. Manzo, and D. Paparo, “Optical spin-to-orbital angular momentum conversion in inhomogeneous anisotropic media,” *Physical Review Letters*, vol. 96, no. 16, p. 163905, 2006.
- [109] S. A. Schulz, T. Machula, E. Karimi, and R. W. Boyd, “Integrated multi vector vortex beam generator,” *Optics Express*, vol. 21, no. 13, pp. 16130–16141, 2013.
- [110] A. S. Ostrovsky, C. Rickenstorff-Parrao, and V. Arrizón, “Generation of the “perfect” optical vortex using a liquid-crystal spatial light modulator,” *Optics Letters*, vol. 38, no. 4, pp. 534–536, 2013.
- [111] J. García-García, C. Rickenstorff-Parrao, R. Ramos-García, V. Arrizón, and A. S. Ostrovsky, “Simple technique for generating the perfect optical vortex,” *Optics Letters*, vol. 39, no. 18, pp. 5305–5308, 2014.
- [112] A. T. O’Neil, I. MacVicar, L. Allen, and M. J. Padgett, “Intrinsic and extrinsic nature of the orbital angular momentum of a light beam,” *Physical Review Letters*, vol. 88, p. 053601, Jan 2002.
- [113] N. B. Simpson, K. Dholakia, L. Allen, and M. J. Padgett, “Mechanical equivalence of spin and orbital angular momentum of light: an optical spanner,” *Optics Letters*, vol. 22, pp. 52–54, Jan 1997.
- [114] K. T. Gahagan and G. A. Swartzlander, “Optical vortex trapping of particles,” *Optics Letters*, vol. 21, pp. 827–829, Jun 1996.
- [115] M. Babiker, W. Power, and L. Allen, “Light-induced torque on moving atoms,” *Physical Review Letters*, vol. 73, no. 9, p. 1239, 1994.
- [116] D. L. Andrews and M. Babiker, *The angular momentum of light*. Cambridge University Press, 2012.
- [117] R. Généaux, A. Camper, T. Auguste, O. Gobert, J. Caillat, R. Taeïb, and T. Ruchon, “Attosecond light and electronic vortices,” *arXiv preprint arXiv:1509.07396*, 2015.
- [118] G. Gariépy, J. Leach, K. T. Kim, T. J. Hammond, E. Frumker, R. W. Boyd, and P. B. Corkum, “Creating high-harmonic beams with controlled orbital angular momentum,” *Physical Review Letters*, vol. 113, p. 153901, 2014.
- [119] M. Zürch, C. Kern, P. Hansinger, A. Dreischuh, and C. Spielmann, “Strong-field physics with singular light beams,” *Nature Physics*, vol. 8, no. 10, pp. 743–746, 2012.
- [120] J. Vieira, R. Trines, E. Alves, R. Fonseca, J. Mendonça, R. Bingham, P. Norreys, and L. Silva, “Amplification and generation of ultra-intense twisted laser pulses via stimulated raman scattering,” *Nature Communications*, vol. 7, 2016.
- [121] C. Hernández-García, A. Picón, J. San Román, and L. Plaja, “Attosecond extreme ultraviolet vortices from high-order harmonic generation,” *Physical Review Letters*, vol. 111, no. 8, p. 083602, 2013.
- [122] C. Hernandez-Garcia, A. Picon, J. San Roman, and L. Plaja, “Coherent attosecond extreme ultraviolet vortices from high-order harmonic generation,” in *Laser Science*, pp. LW5H–6, Optical Society of America, 2014.

- [123] X. Zhang, B. Shen, Y. Shi, X. Wang, L. Zhang, W. Wang, J. Xu, L. Yi, and Z. Xu, "Generation of intense high-order vortex harmonics," *Physical Review Letters*, vol. 114, no. 17, p. 173901, 2015.
- [124] O. Matula, A. G. Hayrapetyan, V. G. Serbo, A. Surzhykov, and S. Fritzsche, "Atomic ionization of hydrogen-like ions by twisted photons: angular distribution of emitted electrons," *Journal of Physics B: Atomic, Molecular and Optical Physics*, vol. 46, no. 20, p. 205002, 2013.
- [125] A. Afanasev, C. E. Carlson, and A. Mukherjee, "Off-axis excitation of hydrogenlike atoms by twisted photons," *Physical Review A*, vol. 88, no. 3, p. 033841, 2013.
- [126] J. Wätzel, Y. Pavlyukh, A. Schäffer, and J. Berakdar, "Optical vortex driven charge current loop and optomagnetism in fullerenes," *Carbon*, vol. 99, pp. 439 – 443, 2016.
- [127] A. Picón, A. Benseny, J. Mompart, J. V. de Aldana, L. Plaja, G. F. Calvo, and L. Roso, "Transferring orbital and spin angular momenta of light to atoms," *New Journal of Physics*, vol. 12, no. 8, p. 083053, 2010.
- [128] C. F. Hermanns, M. Bernien, A. Krüger, C. Schmidt, S. T. Waßerroth, G. Ahmadi, B. W. Heinrich, M. Schneider, P. W. Brouwer, K. J. Franke, *et al.*, "Magnetic coupling of Gd₃N@C₈₀ endohedral fullerenes to a substrate," *Physical Review Letters*, vol. 111, no. 16, p. 167203, 2013.
- [129] J. E. Grose, E. S. Tam, C. Timm, M. Scheloske, B. Ulgut, J. J. Parks, H. D. Abruna, W. Harneit, and D. C. Ralph, "Tunnelling spectra of individual magnetic endofullerene molecules," *Nature Materials*, vol. 7, no. 11, pp. 884–889, 2008.
- [130] R. Westerström, J. Dreiser, C. Piamonteze, M. Muntwiler, S. Weyeneth, H. Brune, S. Rusponi, F. Nolting, A. Popov, S. Yang, *et al.*, "An endohedral single-molecule magnet with long relaxation times: DySc₂N@C₈₀," *Journal of the American Chemical Society*, vol. 134, no. 24, pp. 9840–9843, 2012.
- [131] K. Yamane, Y. Toda, and R. Morita, "Ultrashort optical-vortex pulse generation in few-cycle regime," *Optics express*, vol. 20, no. 17, pp. 18986–18993, 2012.
- [132] M. Feng, J. Zhao, and H. Petek, "Atomlike, hollow-core-bound molecular orbitals of C₆₀," *Science*, vol. 320, no. 5874, pp. 359–362, 2008.
- [133] Y. Pavlyukh and J. Berakdar, "Angular electronic 'band structure' of molecules," *Chemical Physics Letters*, vol. 468, no. 4, pp. 313–318, 2009.
- [134] Y. Pavlyukh and J. Berakdar, "Kohn-sham potentials for fullerenes and spherical molecules," *Physical Review A*, vol. 81, no. 4, p. 042515, 2010.
- [135] T. Huang, J. Zhao, M. Feng, H. Petek, S. Yang, and L. Dunsch, "Superatom orbitals of Sc₃N@C₈₀ and their intermolecular hybridization on Cu(110) – (2 × 1) – O surface," *Physical Review B*, vol. 81, no. 8, p. 085434, 2010.
- [136] Y. Pavlyukh and J. Berakdar, "Communication: Superatom molecular orbitals: New types of long-lived electronic states," *The Journal of Chemical Physics*, vol. 135, no. 20, p. 201103, 2011.
- [137] M. Feng, Y. Shi, C. Lin, J. Zhao, F. Liu, S. Yang, and H. Petek, "Energy stabilization of the s-symmetry superatom molecular orbital by endohedral doping of c 82 fullerene with a lanthanum atom," *Physical Review B*, vol. 88, no. 7, p. 075417, 2013.

- [138] V. K. Voora, L. S. Cederbaum, and K. D. Jordan, "Existence of a correlation bound s-type anion state of C_{60} ," *The Journal of Physical Chemistry Letters*, vol. 4, no. 6, pp. 849–853, 2013.
- [139] S. Klaiman and L. S. Cederbaum, "The best orbital and pair function for describing ionic and excited states on top of the exact ground state," *The Journal of Chemical Physics*, vol. 141, no. 19, p. 194102, 2014.
- [140] V. Zakrzewski, O. Dolgounitcheva, and J. Ortiz, "Electron propagator calculations on the ground and excited states of C_{60} ," *The Journal of Physical Chemistry A*, vol. 118, no. 35, pp. 7424–7429, 2014.
- [141] L. Levy, G. Dolan, J. Dunsmuir, and H. Bouchiat, "Magnetization of mesoscopic copper rings: Evidence for persistent currents," *Physical Review Letters*, vol. 64, no. 17, p. 2074, 1990.
- [142] D. Mailly, C. Chapelier, and A. Benoit, "Experimental observation of persistent currents in gaas-algaas single loop," *Physical Review Letters*, vol. 70, no. 13, p. 2020, 1993.
- [143] M. A. Noyan and J. M. Kikkawa, "Time-resolved orbital angular momentum spectroscopy," *Applied Physics Letters*, vol. 107, no. 3, p. 032406, 2015.
- [144] H. Muller, "Numerical simulation of high-order above-threshold-ionization enhancement in argon," *Physical Review A*, vol. 60, no. 2, p. 1341, 1999.
- [145] E. Toma and H. Muller, "Calculation of matrix elements for mixed extreme-ultraviolet–infrared two-photon above-threshold ionization of argon," *Journal of Physics B: Atomic, Molecular and Optical Physics*, vol. 35, no. 16, p. 3435, 2002.
- [146] J. Higuete, H. Ruf, N. Thiré, R. Cireasa, E. Constant, E. Cormier, D. Descamps, E. Mével, S. Petit, B. Pons, *et al.*, "High-order harmonic spectroscopy of the cooper minimum in argon: Experimental and theoretical study," *Physical Review A*, vol. 83, no. 5, p. 053401, 2011.
- [147] K. Shirai, "The basis functions and the matrix representations of the single and double icosahedral point group," *Journal of the Physical Society of Japan*, vol. 61, no. 8, pp. 2735–2747, 1992.
- [148] M. Frisch, G. Trucks, H. Schlegel, G. Scuseria, M. Robb, J. Cheeseman, J. Montgomery Jr, T. Vreven, K. Kudin, J. Burant, *et al.*, "Gaussian 03, revision d. 01," *Gaussian Inc., Wallingford, CT*, vol. 26, 2004.
- [149] R. Haddon, L. E. Brus, and K. Raghavachari, "Electronic structure and bonding in icosahedral C_{60} ," *Chemical Physics Letters*, vol. 125, no. 5-6, pp. 459–464, 1986.
- [150] J. D. Jackson, *Classical electrodynamics*. Wiley, 1999.
- [151] K. Köksal and J. Berakdar, "Charge-current generation in atomic systems induced by optical vortices," *Physical Review A*, vol. 86, no. 6, p. 063812, 2012.
- [152] W. Tan and J. Inkson, "Electron states in a two-dimensional ring-an exactly soluble model," *Semiconductor Science and Technology*, vol. 11, no. 11, p. 1635, 1996.
- [153] Y. Imry, *Introduction to mesoscopic physics*. Oxford University Press on Demand, 2002.

- [154] T. Chakraborty and P. Pietiläinen, “Electron-electron interaction and the persistent current in a quantum ring,” *Physical Review B*, vol. 50, no. 12, p. 8460, 1994.
- [155] C. Presilla and J. Sjöstrand, “Nonlinear resonant tunneling in systems coupled to quantum reservoirs,” *Physical Review B*, vol. 55, no. 15, p. 9310, 1997.
- [156] A. Matos-Abiague and J. Berakdar, “Photoinduced charge currents in mesoscopic rings,” *Physical Review Letters*, vol. 94, no. 16, p. 166801, 2005.
- [157] J. M. Ziman, *Principles of the Theory of Solids*. Cambridge university press, 1972.
- [158] X. Zhang and Z. Liu, “Superlenses to overcome the diffraction limit,” *Nature Materials*, vol. 7, no. 6, pp. 435–441, 2008.
- [159] J. Zhao, G. Zheng, S. Li, H. Zhou, Y. Ma, R. Zhang, Y. Shi, and P. He, “A hyperlens-based device for nanoscale focusing of light,” *Chinese Optics Letters*, vol. 10, no. 4, p. 042302, 2012.
- [160] A. Fuhrer, S. Lüscher, T. Ihn, T. Heinzl, K. Ensslin, W. Wegscheider, and M. Bichler, “Energy spectra of quantum rings,” *Nature*, vol. 413, no. 6858, pp. 822–825, 2001.
- [161] A. Lorke, R. J. Luyken, A. O. Govorov, J. P. Kotthaus, J. Garcia, and P. M. Petroff, “Spectroscopy of nanoscopic semiconductor rings,” *Physical Review Letters*, vol. 84, no. 10, p. 2223, 2000.
- [162] L. Zoppi, L. Martin-Samos, and K. Baldrige, “Buckybowl superatom states: a unique route for electron transport?,” *Physical Chemistry Chemical Physics*, vol. 17, no. 8, pp. 6114–6121, 2015.

List of figures

- 1.1 Streaking spectrogram corresponding to the photoionization of the hydrogen 1s ground state by an XUV pulse with a photon energy $\hbar\omega_{\text{XUV}} = 27.211$ eV. The photoelectron is probed by an 800 nm IR laser field with a duration of 6 fs and an intensity of 10^{12} W/cm². The red color means here the largest ionization probability while violet corresponds to no photoionization. The electron momentum distribution is depicted for various values of the delay time $\Delta_{\text{XUV-IR}}$ between the maxima of the XUV and IR field. The solid white line shows the center of energy (COE) and therefore the peak position of the final electron momentum distribution. The small inset reveals the streaking delay τ_{S} 9
- 1.2 Illustration of RPAE equations. The straight lines with an arrow to the right represent a continuum state, while an arrow to the left stands for a bound (hole) state. The curly line displays the Coulomb interaction while a dashed line exhibits a photon with the energy $\hbar\omega$. The filled circle represents the correlated matrix element while the bare reduced matrix element is displayed by the bifurcation. The time axis goes from left to right. 20
- 1.3 Angular dependence of the time delays corresponding to photoelectrons liberated from the different initial states of the 2s and 2p subshells in neon. The photon energy $\hbar\omega_{\text{XUV}} = 106$ eV. Results within the RPAE and numerical calculations are shown. 22
- 1.4 (a) Scattering phases of the different ionization channels within HF approximation and RPAE. Both enter the evaluation of the time delay according to Eq. (1.45). (b) Angular dependence of the relative delay τ_{W}^{2p-2s} at a photon energy $\hbar\omega_{\text{XUV}} = 106$ eV as an average of the contributions of all possible initial states. The inset shows the β -parameter β_{2p} of the 2p subshell calculated on the basis of the pseudopotential and the RPAE model. The crosses represent the experimental data given in Ref. [87]. 23
- 1.5 The relative time delay τ_{W}^{2p-2s} within the RPAE in dependence on the photon energy $\hbar\omega_{\text{XUV}}$ for different angles $\vartheta_{\mathbf{k}}$ 24

1.6	(a) Photoionization cross sections corresponding to the $3s$ and $3p$ subshells in argon. (b) Scattering phases of argon of the different ionization channels within HF approximation and RPAE.	26
1.7	(a) Time delay corresponding to the photoionization process of the $3s$ subshell in argon. (b) Time delay τ_{W}^{3p} for different asymptotic directions $\vartheta_{\mathbf{k}}$ of the liberated photoelectron. The inset shows the angular dependence of the full averaged delays in the case of three different photon energies around the Cooper minimum.	27
1.8	(a) Comparison of the angle-integrated time delay τ_{W}^{3p} corresponding to the photoionization of the $3p$ subshell calculated within the RPAE with the experimental measurement [66]. (b) Full relative time delay τ_{W}^{3s-3p} in dependence on the photon energy and different asymptotic directions $\vartheta_{\mathbf{k}}$ of the photoelectron. For comparison, the experimental results by the RABBIT method are included (closed circles, Ref. [5]; open squares, Ref. [4]). . .	28
2.1	A general schematic representation of the coordinate system corresponding to the investigations below. The considered object (in this particular case the C_{60} molecule) in the xy -plane has the distance ρ_0 to the optical axis of the vortex beam. The vector $\rho = r \sin(\vartheta)$ marks the position of the electron relative to the center of mass of the object, while ρ' is relative to the optical axis. The shaded area indicates the donut-shaped high-intensity regime of the optical vortex.	35
2.2	(a) Reduced radial matrix elements for the partial wave functions with the orbital angular momenta $\ell = 1$ and $\ell = 3$. (b) Photoionization probabilities for the three different initial states of the $3p$ subshell in argon.	38
2.3	The photoelectron momentum distributions corresponding to (a) $m_i = 1$ at $\vartheta_{\mathbf{k}} = 90^\circ$ and (b) $m_i = -1$ at $\vartheta_{\mathbf{k}} = 150^\circ$. The number of optical cycles $n = 10$. The other pulse parameters are given in the text.	40
2.4	Wigner Time delays as a function of the azimuthal angle $\varphi_{\mathbf{k}}$ for different directions $\vartheta_{\mathbf{k}}$ with respect of to optical axis of the optical vortex. The left column belongs to the photoionization process for $\vartheta_{\mathbf{k}} = 90^\circ$ where the photoelectron with $m_i = +1$ is dominant, while the right column is associated with $\vartheta_{\mathbf{k}} = 150^\circ$ (photoelectron with $m_i = -1$ dominates). Here a short pulse is considered, i.e. $n = 3$	42
2.5	Wigner Time delays as a function of the azimuthal angle $\varphi_{\mathbf{k}}$ for different directions $\vartheta_{\mathbf{k}}$ with respect to the optical axis of the optical vortex. The situations where either (a) the co-rotating photoelectron or (b) the counter-rotating photoelectron dominates the photoionization process are shown. The long pulse duration is characterized by $n = 10$	43

2.6	The $3p$ time delays τ_W^{3p} corresponding to the situations where either the co-rotating or the counter-rotating electron dominates the photoionization process in dependence on the distance ρ_0 between the optical axis and the center of the argon atom. A long optical vortex laser pulse is considered, i.e. $n = 10$	44
2.7	(a) The energy spectrum and (b) the corresponding normalized wave functions of the second and third radial band of the C_{60} molecule.	47
2.8	The magnetic moment in dependence on the distance between the optical axis and the center of the molecule (characterized by the ratio ρ_0/ρ_{\max}) and the photon energy $\hbar\omega$ for (a) $\ell_{\text{OAM}} = 1$ and (b) $\ell_{\text{OAM}} = 2$	50
2.9	The various possible transitions in dependence on the topological charge ℓ_{OAM} for (a) $\rho_0/\rho_{\max} = 0$ and (b) $\rho_0 = \rho_{\max}$	51
2.10	(a) Transition scheme for $\rho_0/\rho_{\max} = 0.2$. (b) The over a homogeneous gas-phase averaged photo-induced magnetic moment in dependence on the photon energy $\hbar\omega$ for different topological charges ℓ_{OAM}	52
2.11	The current density $j_\phi(\mathbf{r})$ for a photon energy $\hbar\omega = 8.8$ eV and a topological charge $\ell_{\text{OAM}} = 1$ in (a) the xy -plane and (b) the xz -plane.	54
2.12	The photo-induced magnetic fields in the center of the C_{60} molecule in dependence on the topological charge m_{OAM} for (a) $\rho_0 = 0$ and (b) $\rho_0 = \rho_{\max}$	55
2.13	Photo-induced magnetic field for a C_{60} molecule positioned at the maximum of intensity and a optical vortex beam with a photon energy $\hbar\omega = 9.3$ eV. The color scale characterizes the amplitude: red arrows mark the strongest contribution while the blue color reveals a weak field.	56
2.14	(a) The energy levels E_{l_0, m_0} of the ring structure where the corresponding Fermi energy ε_F is marked by the horizontal dashed line. (b) Initial LDOS of the considered 2D-system.	58
2.15	(a) LDOS of the system after a propagation time of $t = 2$ ps. (b) Inner and outer density $Q^{\text{In/Out}}$ of the ring structure in dependence of the propagation time.	60
2.16	A proposed scheme for an open circuit voltage generation driven by an optical vortex beam. The irradiated ring structure (with a spiral phase plate on the top) is separated by two thin tunneling barriers (blue) from two electrodes which gather the charge carriers.	61

- 2.17 (a) The LDOS of the ring structure which is connected with a conducting bar after a propagation time of $t = 2.4$ ps, i.e. after the optical vortex pulse is off. The thick horizontal line at $y_d = -140$ nm marks a detector to record the photo-induced current whose direction is shown by the arrow. The vertical dashed lines indicate the wire potential boundaries. (b) The initial ring LDOS together with the OAM beam intensity profile. The wire is not affected by the optical vortex beam. (c) Time-dependent total currents (cf. (2.33)) through the detector for different topological charges ℓ_{OAM} . . . 63
- 2.18 (a) LDOS of the ring structure which is attached to two conducting bars. The considered topological charge $\ell_{\text{OAM}} = -10$ and the propagation time is $t = 1.3$ ps, i.e. the applied OAM pulse is still on. The used parameters are the same as in the simulation shown in Fig.(2.17). (b) A schematic device for generating a photo-induced current based on the mechanism described in the text. On each of the quantum ring structures, a spiral phase plate is placed that produces an optical vortex (indicated by the red arrows) from an incoming unstructured light wave. The subsequent interaction with the charge carriers leads to a directed current in the wires which is enhanced with every additional ring in the device. 65

List of Publications

Parts of this thesis are published as:

1. J. Wätzel, A. Moskalenko, Y. Pavlyukh, and J. Berakdar, "Angular resolved time delay in photoemission," *Journal of Physics B: Atomic Molecular and Optical Physics*, vol. 48, no. 2, p. 025602, 2014.
2. J. Wätzel, Y. Pavlyukh, A. Schäffer, and J. Berakdar, "Optical vortex driven charge current loop and optomagnetism in fullerenes," *Carbon*, vol. 99, pp. 439–443, 2016.
3. J. Wätzel and J. Berakdar, "Centrifugal photovoltaic and photogalvanic effects driven by structured light," *Scientific Reports*, vol. 6, no. 21475, 2016.
4. J. Wätzel and J. Berakdar, "Discerning on a sub-optical-wavelength the attosecond time delays in electron emission from magnetic sublevels by optical vortices," *Physical Review A*, vol. 94, no. 033414, 2016.

Acknowledgements

The work presented in this thesis would not have been performed without the help of many colleagues, co-workers, and friends.

First of all, I want to thank my supervisor Prof. Jamal Berakdar for giving me the opportunity to do a doctorate in fascinating and diverse fields of physics. He always encouraged me to improve my scientific work and shared a lot of his physical insights with me. It is admirable that he was never really upset when some of his ideas did not come to fruition and his commitment to form good scientists was perceptible all the time. The many opportunities to attend a lot of conferences, to give talks and presenting my work enriched my scientific understanding immensely.

I am furthermore really thankful for sharing some time with Dr. Yaroslav Pavlyukh and Dr. Andrey Moskalenko, who guided me through some integral parts of this thesis. Without their patience in many discussions and their rich expertise, this thesis would not be existent in this form.

A big thank you is dedicated to all my office neighbors who enriched my scientific and private life with interesting discussions: My direct office neighbor Michael Schüler, Stefan Stagraczyński, Seyyed Ruhollah Etesami, Maryam Azimi, Alexander Sukhov, Levan Chotorlishvili with his wise words, Conrad Schuster, my fitness apprentice Mário Rui Gonçalves Marques, Carlos Benavides Riveros, Dominik "Kinimod" Schulze and the wonderful Alexander Schäffer.

Last but not least, this thesis would not have been existing without the endless support of my family and friends. I am grateful to my parents, who enabled me a strong education which led eventually to the study of physics. Furthermore, I am very proud to have such a group of wonderful and warm friends around me. At the top stands Julia Katharina Müller, who always took care of me as well as encouraged and supported me in all my decisions.

Curriculum vitae

Personal information

Name	Jonas Wätzel
Date of birth	27.09.1988
Place of birth	Halle (Saale)
Address	Mozartstraße 1, 06114 Halle (Saale)

Education

since 01/2013	PhD studies at the "Martin-Luther University Halle-Wittenberg" Institute for Physics, 06120 Halle (Saale)
11/2010–09/2012	Study of Physics at the "Martin-Luther-University Halle-Wittenberg" Institute for Physics, 06120 Halle (Saale) Master Degree Thesis: "Attosecond dynamics in nanostructures" Supervisor: Prof. Jamal Berakdar
10/2007–10/2010	Study of Physics at the "Martin-Luther-University Halle-Wittenberg" Institute for Physics, 06112 Halle (Saale) Bachelor Degree Thesis: "Lichtinduzierte Dynamik von Ladung und Spin in Nanostrukturen" Supervisor: Prof. Jamal Berakdar
08/2001-07/2007	High School, "Gymnasium Landsberg", 06188 Landsberg
08/1999-07/2001	Secondary School, "Dr. Theodor-Neubauer Sekundarschule", 06188 Landsberg OT Hohenthurm
08/1999-07/1999	Elementary school, "Albrecht-Dürer-Schule", 06114 Halle (Saale)

Scientific career

- 11/2009-9/2012 Student Assistant at the “Martin-Luther University Halle-Wittenberg”
in the group of Prof. Dr. Jamal Berakdar
- 11/2011-6/2016 Student Assistant at the “Martin-Luther University Halle-Wittenberg”
on behalf of the institute

Jonas Wätzel

Eidesstattliche Erklärung

Hiermit erkläre ich, gemäß §5 der Promotionsordnung der Naturwissenschaftlichen Fakultät II - Chemie, Physik und Mathematik der Martin-Luther-Universität Halle-Wittenberg vom 13.06.2012, dass die vorliegende Arbeit

"Ultrafast dynamics driven by attosecond and structured photons"

selbständig und ohne fremde Hilfe verfasst, andere als die von mir angegebenen Quellen und Hilfsmittel nicht benutzt und die den benutzten Werken wörtlich oder inhaltlich entnommenen Stellen als solche kenntlich gemacht habe. Ich erkläre, die Angaben wahrheitsgemäß gemacht und keine Dissertation an einer anderen wissenschaftlichen Einrichtung zur Erlangung eines akademischen Grades eingereicht zu haben

Jonas Wätzel

August 2016